OPTICAL AND THERMAL PROPERTIES OF SAMARIUM-DOPED FLUOROPHOSPHATE AND FLUOROALUMINATE GLASSES FOR HIGH-DOSE, HIGH-RESOLUTION DOSIMETRY APPLICATIONS

A Thesis Submitted to the College of

Graduate Studies and Research

In Partial Fulfillment of the Requirements

For the Degree of Doctor of Philosophy

In the Division of Biomedical Engineering

University of Saskatchewan

Saskatoon

By

SHAHRZAD VAHEDI

Permission to Use

In presenting this thesis in partial fulfilment of the requirements for a Postgraduate degree from the University of Saskatchewan, I agree that the Libraries of this University may make it freely available for inspection. I further agree that permission for copying of this thesis in any manner, in whole or in part, for scholarly purposes may be granted by the professor or professors who supervised my thesis work or, in their absence, by the Head of the Department or the Dean of the College in which my thesis work was done. It is understood that any copying or publication or use of this thesis or parts thereof for financial gain shall not be allowed without my written permission. It is also understood that due recognition shall be given to me and to the University of Saskatchewan in any scholarly use which may be made of any material in my thesis.

Requests for permission to copy or to make other use of material in this thesis in whole or part should be addressed to:

Head of the Division of Biomedical Engineering

57 Campus Drive

University of Saskatchewan

Saskatoon, Saskatchewan, Canada

S7N 5A9

Abstract

Microbeam radiation therapy (MRT) is an experimental form of radiation treatment which causes less damage to normal tissue in comparison with customary broad-beam radiation treatment. In this method the synchrotron generated X-ray beam is passed through a multislit collimator and applied to the tumor in the form of an array of planar microbeams. MRT dosimetry is an extremely challenging task and no current detector can provide the required wide dynamic rang and high spatial resolution. In this thesis, fluorophosphate (FP) and fluoroaluminate (FA) glass plates doped with trivalent samarium (Sm^{3+}) are characterized towards developing a potential X-ray detector suitable for MRT dosimetry. The detection is based on the difference in the photoluminescence signatures of Sm^{3+} ions and Sm^{2+} ions; the latter are formed under X-ray irradiation. This valency conversion is accompanied by the formation of defects including hole centers (HCs) and electron centers (ECs) in the glass structure which absorb light in the UV and visible regions (induced absorbance). Both FP and FA glasses show promising dynamic range for MRT and may be used as a linear sensor up to ~150 Gy and as a nonlinear sensor up to ~2400 Gy, where saturation is reached. X-ray induced defects saturate at the same dose. The optimum doping concentration is in the 0.001- 0.2 at.% range. Doping with higher concentrations will decrease the conversion efficiency. The glass plates also show a very promising spatial resolution (as high as a few microns) for recording the dose profile of microbeams which is readout using a confocal fluorescence microscopy technique. These plates are restorable as well and the response is reproducible. The effects of previous X-ray exposure including samarium valency conversion as well as induced absorbance may be erased by annealing at temperatures exceeding the glass transition temperature T_g while annealing at $T_A < T_g$ enhances the response. This enhancement is explained by a thermally

stimulated relaxation of host glass ionic matrix surrounding X-ray induced Sm^{2+} ions. Optical erasure is another practical means to erase the recorded data. Nearly complete Sm^{2+} to Sm^{3+} reconversion (erasure) is achieved by intense optical illumination at 405 nm. While, existing X-ray induced bands would be only partially erased. Electron spin resonance (ESR) and optical absorbance spectroscopy are used to investigate the nature of X-ray induced defects and their correlation with Sm valency conversion. A model based on competition between defect center formation and the $Sm^{3+} \leftrightarrows Sm^{2+}$ conversion successfully explains the different processes occurring in the glass matrix under X-ray irradiation.

Acknowledgments

I would like to express my sincerest gratitude to my supervisor, Dr. Safa Kasap who has been a steady source of wise encouragement, invaluable advices, guidance and support throughout my doctoral studies. His knowledge and passion for science have made laboratory work so much more motivating and exciting. I specifically thank him for being patient, understanding and supportive through tough times in both my professional and personal lives. I am also indebted to my co-supervisor, Dr. Dean Chapman and the members of my committee, who provided essential advice, comments and kind encouragement during the course of this research. I am especially grateful to my mentor, Dr. Cyril Koughia for his priceless advices, fruitful discussions and assistance throughout the experimental works. He has been a great teacher who taught me how to work as an independent researcher.

Special thanks to Dr. Andy Edgar and Mr. Chris Varoy for preparing the samples. I appreciate the suggestions, advices and critiques of Dr. Edgar throughout our collaboration. I would also like to thank my colleagues Mr. Go Okada and Mr. Thomas Meyer for friendship and assistance, Dr. George Belev for his help at the Canadian Light Source and Dr. Ramaswami Sammynaiken for his guidance regarding electron paramagnetic resonance.

Finally, but not the least, I would like to thank my family who have been a constant source of support and encouragement throughout my studies and my life.

Dedication

I lovingly dedicate this thesis to my husband Omid, who has always been there through the hard times.

Table of Contents

page

Permission to Use i

Abstract ii

Acknowledgments iv

List of Tables viii

List of Figures ix

List of Abbreviations xvi

1 Introduction and Organization of the Thesis 1
1.1 Introduction 1
1.1.1. Objective 4
1.1.2. Experimental Techniques 5
1.2. Organization of the Thesis 7
2 Theoretical Background 10
2.1 Microbeam Radiation Therapy (MRT) 10
2.1.1 Prospective Dosimeters for MRT 14
2.1.1.1 Gafchromic Film Dosimetry 14
2.1.1.2 Ionization Chambers 15
2.1.1.3 Alanine Dosimeters 15
2.1.1.4 Polymer Gels 16
2.1.1.5 Thermoluminescence Detectors 16
2.1.1.6 Fluorescent Nuclear Track Detectors (FNTDs) 17
2.1.1.7 MOSFET Detectors 17
2.1.1.8 Silicon Strip Detector 18
2.1.1.9 PRESAGE™ Radiochromic Plastic 19
2.1.1.10 High Resolution Optical Calorimetry 19
2.1.1.11 Radiophotoluminescence Glass Dosimeters 20
2.2 Rare-Earth (RE) Ion Doped Glasses 20
2.2.1 Electronic Structure of RE Ions 20
2.2.2 Samarium and Europium Ions 21
2.2.2.1 Emission Spectra (Photoluminescence) 22
2.2.2.2 Excitation Spectra 24
2.2.3 Effect of RE Doping on the Glass Structure 25
2.2.4 Valency Conversion of RE Ions under High Energy Irradiation 26
2.2.5 Photodarkening Effect and Defect Centers 27
2.2.5.1 Defect Centers in Phosphate Glasses 30
2.2.5.2 Electron Spin Resonance (ESR) Spectroscopy 31
2.2.5.2.1 Saturation 33
2.2.5.2.2 Hyperfine Splitting 34
2.2.5.2.3 Lineshapes 35

2.3 References 36
3 X-ray Induced Sm^{3+} to Sm^{2+} Conversion in Fluorophosphate and Fluoroaluminate Glasses for the Monitoring of High-doses in Microbeam Radiation Therapy 45
3.1 Abstract 46
3.2 Introduction 46
3.3 Experimental 48
3.4 Results and Discussion 50
3.5 Conclusion 69
Acknowledgment 70
3.6 Appendix: Modeling of Thermal Enhancement 70
3.7 References 74
4 Optically Erasable Samarium-Doped Fluorophosphate Glasses for High-Dose Measurements in Microbeam Radiation Therapy 78
4.1 Abstract 78
4.2 Introduction 79
4.3 Experimental 82
4.4 Results and Discussion 84
4.5 Conclusion 98
Acknowledgments 100
4.6 References 100
5 ESR Study of Samarium Doped Fluorophosphate Glasses for High-Dose, High-Resolution Dosimetry 105
5.1 Abstract 105
5.2 Introduction 106
5.3 Experimental 109
5.4 Results and Discussion 111
5.4.1 ESR Spectra 111
5.4.2 Effect of Sm Doping Concentration on Defects 114
5.4.3 Effect of Thermal Annealing on Defects 118
5.5 Conclusion 123
Acknowledgments 124
5.6 References and Links 125
6 Conclusion and Suggestions for Future Work 131
6.1 Summary and Conclusions 131
6.2 Suggestions for Future Work 135
Appendix: X-Ray Irradiation and Dose Calculation 136
A.1 Faxitron X-Ray Cabinet 136
A.2 Canadian Light Source 139
A.3 References 140

List of Tables

Table page

Table 4.1 The comparison of central wavelengths (λ), central energies (*E*), and widths (*W*) of Gaussian absorption bands (G1–G6) observed in the present paper with earlier data by Ebeling *et al.* [40] The widths (*W*) of Gaussian bands refer to the full width at half maximum (FWHM). 92

Table 4.2 The lines used for approximating the ESR signals of FP10 glass doped with 0.5% of Sm^{3+} and X-ray irradiated for 2 h. The total dose delivered is ~6 kGy. Three doublets have Gaussian (Γ) and two have Lorentzian (L) lineshapes. $g^{(1)}$ and $g^{(2)}$ are the effective *g*-values for each line of a doublet. $g_{average}$ is the average of $g^{(1)}$ and $g^{(2)}$. *A* is a splitting of two lines of a doublet. *W* is the full width of each line at half maximum. *W* and *A* are defined for a nominal frequency of 9.8 GHz. Possible interpretation of structures related to appropriate doublet is based on comparison with Ebeling *et al.* [40]. 95

Table 5.1 The *unique set* of Lorentzians and Gaussians (characterized by positions and widths) used for approximating *the whole set of* ESR spectra obtained in our experiments. Doublets (L_1–L_2) and singlet L_3 have Lorentzian (L) and doublets (Γ_1–Γ_3) have Gaussian (Γ) lineshapes. *W* is a full width of each line at half maximum. $g^{(1)}$ and $g^{(2)}$ are the effective *g*-values for each line of a doublet. $g_{average}$ is the average of $g^{(1)}$ and $g^{(2)}$. *A* is splitting of two lines of a doublet. *W* and *A* are defined for a nominal frequency of 9.8 GHz. 113

List of Figures

Figure page

Figure 1.1 A schematic illustration of MRT concept. Broad X-ray beam generated by a synchrotron source passes through a multi-slit collimator producing the microbeam array applied to the tumor. The resulting dose profile includes large doses (peak dose) where microbeams pass and the doses between microbeams (valley dose). 2

Figure 1.2 Typical room temperature PL spectra of 0.5% Sm^{3+} doped fluoroaluminate glass measured with 405nm excitation light before and after 500 seconds of X-ray irradiation corresponding to a total dose of ~1000 Gy. The irradiation was carried out using synchrotron radiation at the BMIT-BM beamline, Canadian Light Source. The emissions at about 563, 598, 644, and 705 nm in the non irradiated glass can be attributed to the $^4G_{5/2} \rightarrow {}^6H_{5/2,\ 7/2,\ 9/2,\ 11/2}$ transitions of Sm^{3+}, respectively. The five new peaks at 683, 700, 724, 760 and 810 nm observed in the photoluminescence spectrum of the irradiated glass can be ascribed to $^5D_0 \rightarrow {}^7F_{J\,=\,0,\,1,\,2,\,3,\,4}$ transitions of Sm^{2+}, respectively. 3

Figure 2.1 Schematic dose profile of microbeams used in MRT. Microbeam geometry parameters such as beam width, center-to-center distance, peak dose and valley dose are introduced in the figure. Microbeams are usually 20-50 μm wide with a 100-400 μm center-to-center distance. Peak and valley doses are typically in the range of 150–600 Gy and 3–30 Gy, respectively. (Adapted from [13]). 11

Figure 2.2 (a) Tissue-sparing effect of MRT represented by a schematic diagram. High doses delivered by microbeams ablate the tumor tissue while, normal tissue shows extraordinary resistance to the damage and is capable of repairing the irradiation-damaged zones. (After [8]). (b) Normal CNS tissue subjected to microbeam irradiation. It is apparent that tissue has maintained its normal architecture. Paths of microbeams can be observed as white parallel lines in the inset. (After [2]). 12

Figure 2.3 Two undamaged blood vessels pass through the pathways created by microbeams (arrows). This can be evidence for the regeneration of tissue microvasculature after irradiation. (After [8]). 13

Figure 2.4 Tumor tissue and normal skin tissue from mice 24h after MRT. Tissues were stained with g-H2AX/BrdU to image the DNA damage (brown) and cell proliferation (blue). Peak and valley zones are not distinguishable in tumors because of thorough cell migration and intermingling between irradiation damaged (brown) and surviving (blue) tumor cells. On the other hand, the traces of microbeams (brown) are apparent in normal tissue and no significant cell migration is observed. Scale bar, 100 mm. (Adapted from [12]).....13

Figure 2.5 Schematic representation of the X-Tream dosimetry system. Single strip silicon detector (SSD) moves across the microbeams at a constant speed. (Adapted from [35]). 18

Figure 2.6 A PRESAGE rod with sections irradiated under different intensities of microbeams. The section indicated by the arrow includes traces of 16 microbeams (each 25 μm wide), not easily discernible with the human eye. Insert: fluorescence scan of that section (magnified 10×). (After [40]).....19

Figure 2.7 Electronic configuration of rare earth ions: 4f shell is shielded from surrounding host glass ions. (After [55]).....21

Figure 2.8 Fluorescence spectrum and energy level diagram for emission of Sm^{3+} ions in phosphate glass. (Adapted from [60]).....22

Figure 2.9 Photoluminescence spectrum (a) (adapted from [63]) and Energy diagram (b)(after [65]) for Sm^{2+} ions in a host glass. 23

Figure 2.10 Energy diagram for Eu^{2+} and Eu^{3+} ions. (After [66]). 24

Figure 2.11 Excitation spectra of Sm^{3+} and Sm^{2+} in fluoroaluminate glass with emissions at 596 nm and 722nm, respectively. (After [67]). 25

Figure 2.12 The proposed model for the structure of Sm^{3+} doped $Li_2O–SrO–B_2O_3$ glass. It is suggested that non-bridging oxygen and the structural bridging oxygen of the borate groups surround the Sm^{3+} ions. (After [68]).....26

Figure 2.13 Radiation-induced defects in oxygen containing glasses. (After [90]). 28

Figure 2.14 Suggested structures for the r-POHC (right side) and l-POHC (left side) defects. Small spheres symbolize oxygen atoms, while large spheres represent phosphorus or silicon. (After [95]).....30

Figure 2.15 Models for the P1, P2, and P4 defect centers. (Adapted from [102]). 31

Figure 2.16 Variation of energy levels of an unpaired electron as a function of the applied magnetic field. $h\nu_0$ is the microwave energy which is held at a constant value. Resonance occurs when the gap between the energy levels matches the energy of the microwave radiation. (Microwave energy will be absorbed by transitions between these two energy levels). Absorption is shown by dashed lines. The first derivative of absorption (red line) is recorded as the ESR signal.....33

Figure 2.17 Splitting in energy levels and ESR signal due to interaction with the local magnetic field of a nearby spin-1/2 nucleus. The gap between energy levels will match the energy of the microwave radiation ($h\nu_0$) two times (shown by purple and green arrows) as we scan the magnetic field. Thus, microwave energy will be absorbed two times by two allowed transitions (corresponding to two absorption peaks shown by the dashed lines). Thus, two ESR signals (purple line and green line) corresponding to the first derivatives of these two absorptions will be observed. These two signals are splitting by $A = a / (g\mu_B)$. 35

Figure 3.1 The spectra of optical transmittance and photoluminescence of Sm^{3+} and Sm^{2+} ions in (a) fluorophosphate and (b) fluoroaluminate glasses before (as-prepared) and after synchrotron X-ray irradiation for 2000 s corresponding to a total dose of ~3000 Gy. 52

Figure 3.2 The evolution of transmittance (a) and (b) and induced absorbance (c) and (d) as a result of X-ray synchrotron irradiation in FA (a) and (c), and FP (b) and (d) glasses. (e) and (f) present a possible band separation of optical absorbance induced by 600 s of X-ray irradiation in FA and FP glasses, respectively, as sums of Gaussians marked G1-G7 and G1-G4 at their centers. The irradiation was carried out at the Canadian Light Source. 53

Figure 3.3 (a) Comparison of experimentally measured (symbols) and calculated (solid curves) PL spectra of Sm–doped FP10 glass after synchrotron X-ray dose ~1500 Gy. (b) The emission spectra of Sm^{3+} and Sm^{2+} ions (solid lines) and induced absorbance due to POHC (broken line) used in model calculations. The irradiation was carried out at the Canadian Light Source.....55

Figure 3.4 The ratio $R(t) = PL(Sm^{2+})/PL(Sm^{3+})$ for FP (a) and FA(b) glasses doped with varying amounts of Sm^{3+} and codoped with Eu^{2+}, and the intensity of X-ray induced Gaussian absorbance bands (G1-G3 and G1-G7) vs. irradiation time/dose. The lines in (a) are based on an exponential build-up in the dose response with $\tau \approx 270$ s and varying values of R_0. All data refer to as-deposited unannealed samples except for one, closed inverted triangles (▼) that refers to the sample which had received a dose of ~3000 Gy and then was annealed at 490 °C for 30 minutes. The irradiation was carried out at the Canadian Light Source.....57

Figure 3.5 Dose profiles of microbeams used in MRT for three different X-ray exposure times. The dose information was recorded on Sm-doped FA glasses in a form of $Sm^{3+} \rightarrow Sm^{2+}$ conversion and readout using confocal fluorescence microscopy. The microbeams were 50 μm wide and had centre-to-centre separation (periodicity) of 400 μm. 59

Figure 3.6 Erasability and reproducibility of $Sm^{3+} \rightarrow Sm^{2+}$ conversion in FP glass. (a) The ratio $PL(Sm^{2+})/PL(Sm^{3+})$ and (b) absorbance vs. dose of radiation before and after annealing at 550 °C for 30 min. The X-ray irradiation was performed in a FAXITRON X-ray chamber.....61

Figure 3.7 (a) Ratios $R(t) = PL(Sm^{2+})/PL(Sm^{3+})$ of FP and FA Sm-doped glasses versus annealing temperature T_A. The concentration of Sm^{3+} is 0.5% for all glasses. One of the FA glasses is codoped with 0.2% of Eu^{2+}. A sequential step-by-step annealing treatments were carried out at increasing temperatures. The time duration for every annealing step is 30 min. The irradiation was carried out at the Canadian Light Source. Lines are guides to the eye. (b) Spectral shift of $^5D_0 \rightarrow {}^7F_0$ singlet in Sm^{2+} emission in FP and FA glasses from (a) versus annealing temperature T_A. Lines are guides to the eye. (c) The integrated optical absorbance in FP and FA glasses from (a) versus annealing temperature T_A. The integrated optical absorbance was calculated as an integrated area of G1-G3 bands for FP

glass and G1-G6 bands in FA glass. The definition of Gaussians G1-G3 and G1-G6 is given in Figure 3.2. Lines are guides to the eye. (d) Heat capacity (C_p) vs. temperature scan extracted from MDSC thermograms recorded at a heating rate 2 °C/min. The values on the scans show the inflection point, which was used as the operational definition of T_g 62

Figure 3.8 Variation of PL spectra of Sm^{2+} ions in FA (a) and FP (b) host glasses in the vicinity of $^5D_0 \rightarrow {}^7F_J$ (J = 0,1,2) transitions as a result of thermal annealing at temperatures shown in the figure. The duration of all annealing periods is 30 min. The label "as irr" stands for as-irradiated samples prior to all annealing events. The X-ray irradiation was done using a FAXITRON X-ray chamber. 64

Figure 3.9 The effect of isothermal annealing at 400 °C on (a) ratio $R(t) = PL(Sm^{2+})/PL(Sm^{3+})$; (b) induced absorbance; (c) spectral position of the Sm^{2+} ion in the $^5D_0 \rightarrow {}^7F_0$ emission maximum in Sm doped FP glass X-ray irradiated in a FAXITRON X-ray chamber. The lines in figures are fitting curves with parameters as shown in the figures. 66

Figure 3.10 The effect of intense 472 nm illumination on $PL(Sm^{2+})/PL(Sm^{3+})$ ratio in X-ray irradiated Sm doped FP glass before and after annealing. Label "as irradiated" stands for glass irradiated in FAXITRON prior to annealing. The annealing was done at 420 °C for 30 min. Symbols are experimental data. Lines are the best fits using the formulas and fitting parameters as shown in the figure. 67

Figure 3.11 The comparison of model predictions with experimental data. (a) Ratios $R(t) = PL(Sm^{2+})/PL(Sm^{3+})$ of FA Sm-doped glasses versus annealing temperature T_A. The samples and experimental procedure are the same as in Figure 3.7. The lines are fitting curves with parameters as shown in the figure. (b) Spectral shift of $^5D_0 \rightarrow {}^7F_0$ singlet in Sm^{2+} emission of the same glasses versus annealing temperature T_A. The lines are fitting curves with parameters as shown in the figures. (c) Calculated concentrations of divalent Sm ions in (1) metastable and (2) stable configurations. 73

Figure 4.1 X-ray irradiation dose profile images (a) two dimensional and (b) one dimensional before and after optical erasure for different durations of erasure illumination. The peak dose was ~5 kGy. PL excitation wavelength was 470 nm. The optical erasure source was a laser diode emitting at a wavelength of 405 nm. The average erasure illumination power density was ~30 mW/cm ^{2} on the sample. 84

Figure 4.2 The effect of intense 405 nm illumination (erasure) on (a) the photoluminescence and (b) optical transmittance of FP10 glass doped with Sm^{3+}, and previously X-ray irradiated for 2 h (total dose delivered was ~14 kGy). The "as-prepared" trace was measured on the same glass prior to X-ray irradiation. "As irradiated" traces refer to the glass prior to any erasure. The times (durations) of erasure are values in minutes indicated above the corresponding curves. The spectra in (a) are shifted vertically to facilitate the comparison. The erasure illumination was at 405 nm (from an LED) with a power density of ~100 mW/cm ^{2}on the sample. 86

Figure 4.3 The effects of intense (~100 mW/cm^2 on the sample) 405 nm illumination (erasure) from an LED (a) on the response $R(t) = PL(Sm^{2+})/PL(Sm^{3+})$; (b)X-ray induced transmittance; (c) ESR signals in FP10 glasses doped with 0.5% of Sm^{3+} and previously X-ray irradiated for 2 h. All values are shown with respect to their initial values measured in "as irradiated" samples prior to any erasure. (a) Displays the PL twice: in linear and log-log scales. The labeling of Gaussians in (b) is done in accordance with Figure 4.5 and Table 4.1 . The labeling of ESR lines in (c) is done in accordance with Figure 4.6 and Table 4.2 . All lines are guides to the eye. 87

Figure 4.4 Response vs. dose behavior, and the influence of X-ray irradiation before and after two consecutive cycles of optical erasure. The values above the curves in the figure show adjustable parameters giving the best fit to experimental data. Notice that the slope of $R(t)$ vs dose is the same in all three cases. (The erasure illumination was at 405 nm from an LED with a power density ~100 mW/cm^2 on the sample).....89

Figure 4.5 X-ray induced absorbance in FP10 glass doped with 0.5% of Sm^{3+} and initially X-ray irradiated for 2 h (total dose of ~14 kGy) (a)–(d) and nominally undoped FP10 glass irradiated for 30 min (e). Note that (a)–(c) show the evolution of X-ray induced absorbance under intense 405 nm illumination (erasure). (d) demonstrates the effect of annealing at 350 °C for 30 min. The experimental data (symbols) are approximated by a sum of Gaussians (thick solid lines). The individual Gaussians from G1 to G6 are shown by thin (solid and broken) lines. All Gaussians but G6 are marked at their centers. The center of G6 lies outside of the present figure. The broken line in (a) shows that the presence of the band G5 is not necessary prior to erasure in Sm-doped samples. 90

Figure 4.6 The ESR signal of FP10 glass doped with 0.5% of Sm^{3+} and X-ray irradiated for 2 h (total dose of ~6 kGy). (a) is an overview of a spectrum where the two rectangles (b) and (c) show the regions which are presented in (b) and (c), respectively. (b) shows strong and narrow lines in the central part of the spectrum, while (c) shows the weak wings of a spectrum. Experimental data (symbols) are approximated by a model (thick solid line) which is a sum of Lorentzians in (b) and Gaussians in (c), shown by thin broken lines. The Lorentzians in (b) are usually associated with phosphorous-oxygen hole centers (POHC), while the Gaussians in (c) represent three doublets (Γ_1-Γ_3) which are normally associated with POEC. The effective g-values shown in the figure correspond to the centers of corresponding Lorentzian and Gaussian components. 93

Figure 4.7 Response $R = PL(Sm^{2+})/PL(Sm^{3+})$ of FP 10 glass at different delivered doses versus doping (Sm^{3+}) concentration. The PL excitation wavelength was 470 nm.....98

Figure 5.1 The electron spin resonance (ESR) signal of FP glass doped with 0.2% of Sm^{3+} and X-ray irradiated for 2 hours (total dose of ~6 kGy). The spectra were measured after annealing the irradiated sample at 100°C and cooling back to room temperature. The experimental data (thick solid lines) are approximated by a sum of five doublets and one singlet (symbols). Two doublets (L_1 and L_2) and the singlet L_3 have Lorentzian lineshapes while the other three doublets (Γ_1–Γ_3) are Gaussians. The singlet and the individual components of each doublet are shown by thin solid lines and are marked by superscript (1) or (2). Note the change of scale (compression over the x-axis and stretching over y-

axis by a factor of 50) in the wings, (a) and (c), of the graph. The lower scale is shown for a nominal frequency of 9.85 GHz. 111

Figure 5.2 Variation of ESR spectra of FP glass samples as a result of changing the concentration of Sm^{3+} (C_0) in the range of 0–0.5 at.%. All the samples were X-ray irradiated for 2 hours prior to the ESR measurement. Symbols are approximation of experimental data based on the approach presented in Figure 5.1 and Table 5.1. All the signal intensities are normalized to the mass of the samples. 114

Figure 5.3 Variation of ESR signal components ascribed to POHC and POEC according to Table 5.1 versus Sm doping concentration (C_0). All the samples were X-ray irradiated for 2 hours prior to the ESR measurement. ESR signal intensities were normalized to the mass of the samples. I is the intensity of POHC related Lorentzian and POEC related Gaussian lines presented in Table 5.1. In case of Lorentzians, I is the summed intensity of L_1−L_3. Note that the first derivative of these lines sum up to simulate the ESR signal (symbols in Figure 5.2). I_0 is the corresponding intensity in the undoped glass irradiated for the same time (same dose). Lines are the fits using the formulas and the fitting parameters as shown in the figure. (The maximum C_0 value along the x-axis is 1×10^{20} cm^{-3}.) 115

Figure 5.4 The evolution of EPR spectra of the same sample (FP doped with 0.2% of Sm^{3+}) experiencing a step-by-step annealing treatment carried out at increasing temperatures (100°C−300°C) and cooled back to room temperature after each step. The time duration for every annealing step is 30 min. The sample was X-ray irradiated for 2 hours prior to annealing. The experimental ESR data (thick solid lines) are approximated by a sum (symbols) of functions presented in Table 5.1 and Figure 5.1. 119

Figure 5.5 The variation of ESR signal components (a) and (c) and induced absorbance bands (b) and (d) (symbols) versus annealing temperatures (100°C−300°C) related to the same sample of Figure 5.4 (doped with 0.2% of Sm^{3+} and X-ray irradiated for 2 hours prior to annealing). Symbols in (a) and (c) correspond to the intensity of lines presented in Table 5.1 used for approximation of experimental data of Figure 5.4. Symbols in (b) and (d) correspond to the intensity of bands G1−G6 introduced in [30]. (a) and (b) correspond to POHC related bands while (c) and (d) to POEC related bands. All the intensities are normalized to their value at room temperature (20°C) just after irradiation for 2 hours. Lines are guides to eye. 120

Figure 5.6 (a) ESR signal of undoped and doped (0.2% of Sm^{3+}) FP samples recorded in a very wide range. All the samples were X-ray irradiated for 2 h prior to annealing and ESR measurements. The annealing duration was 30 min. Inset shows the corresponding photoluminescence spectra (shifted vertically to facilitate the comparison). Narrow ESR lines observed in the range g = 1.7−2.6 are the same kind of lines shown in Figure 5.4 related to X-ray induced defects. Note the wide range deviation of the ESR signal in samples which show Sm^{2+} photoluminescence. 122

Figure A.1 Outline drawing of Faxitron standard X-ray tube. 136

Figure A.2 X-ray spectra from Faxitron cabinet X-ray system operating at 110 kVp calculated for 1 min irradiation at 5cm from the anode (Air kerma = 50 Gy).....137

Figure A.3 calculated μ/ρ and μ_{en}/ρ and their ratio μ_{en}/μ for FP glass samples.....138

Figure A.4 The normalized spectrum of the X-rays from the BMIT-BM beamline. 139

List of Abbreviations

AL−OHC ..... Aluminum Oxygen Hole Center

BM ..... Bend Magnet

BMIT ..... Biomedical Imaging and Therapy

BOHC ..... Boron Oxygen Hole Center

CLS ..... Canadian Light Source

CNS ..... Central Nervous System

EC ..... Electron Center

ESR ..... Electron Spin Resonance

Eu ..... Europium

Eu^{2+} ..... Divalent Europium

Eu^{3+} ..... Trivalent Europium

FNTD ..... Fluorescent Nuclear Track Detector

FA ..... Fluoroaluminate

FP ..... Fluorophosphate

Gy ..... Gray

HC ..... Hole Center

MOSFET ..... Metal-Oxide-Semiconductor Field-Effect Transistor

MRT ..... Microbeam Radiation Therapy

MSC ..... Multi-Slit Collimator

OHC ..... Oxygen Hole Center

PL ..... Photoluminescence

PO ..... Phosphorus Oxygen

POEC ..... Phosphorus-Oxygen Electron Center

POHC ..... Phosphorous-Oxygen Hole Center

PVDR ..... Peak-to-Valley Dose Ratio

RE ..... Rare-Earth

RT ..... Radiation Therapy

Sm ..... Samarium

Sm^{2+} ..... Divalent Samarium

Sm^{3+} ..... Trivalent Samarium

SSD ..... Silicon Strip Detector

TL ..... Thermoluminescence

TLD ..... Thermoluminescence Detector

TMDSC ..... Temperature Modulated Differential Scanning Calorimeter

UV ..... Ultraviolet

1 Introduction and Organization of the Thesis

1.1 Introduction

Radiation therapy (RT) has been used as a cancer treatment for more than a century. In this method, the ionizing radiation dose delivered to cancerous tumors is limited (up to 80 Gy) to minimize the damage to the normal tissue. Detectors such as ion chambers, semiconductor detectors, films and thermoluminescence detectors (TLDs) are usually used for RT dosimetry applications. However, recently there is a demand for detectors with larger dynamic range and higher spatial resolution due to development of new radiation therapy techniques such as Microbeam Radiation Therapy (MRT). MRT has the advantage of delivering higher doses (~500 Gy) to tumors with less damage to the normal tissue. (A high dose is understood to mean a lethal dose.) Instead of applying a broad beam, a microplanar array of synchrotron-generated parallel X-ray beams (microbeams) delivers a high dose rate to the tumors as shown in Figure 1.1. (The dose rate is the dose delivered per unit time). Microbeams are typically tens of micrometers wide and spaced hundreds of micrometers apart. This specific configuration poses a dosimetry challenge which is measuring dose with a very large gradient (hundreds of grays over only several microns). It is almost impossible to record the microbeam 'peak dose' and the dose between microbeams ('valley dose') simultaneously with current dosimetry techniques. None of the current conventional detectors has the required spatial resolution and large dynamic range for this purpose. The ideal detector should also be sensitive to high dose rates and reusable.

A novel approach for high-dose, high-resolution dosimetry, suitable for MRT, is investigated in this dissertation which is based on the valence conversion of rare-earth (RE) ions upon exposure to X-ray irradiation in a suitable host. Such oxidation state change inevitably leads to changes in the fluorescence spectrum of the irradiated material. For example, a Sm^{3+} - doped

material after irradiation with ionizing radiation, will contain some Sm^{2+} ions (some of the Sm^{3+} ions will be converted under the action of radiation to Sm^{2+} ions). As a result

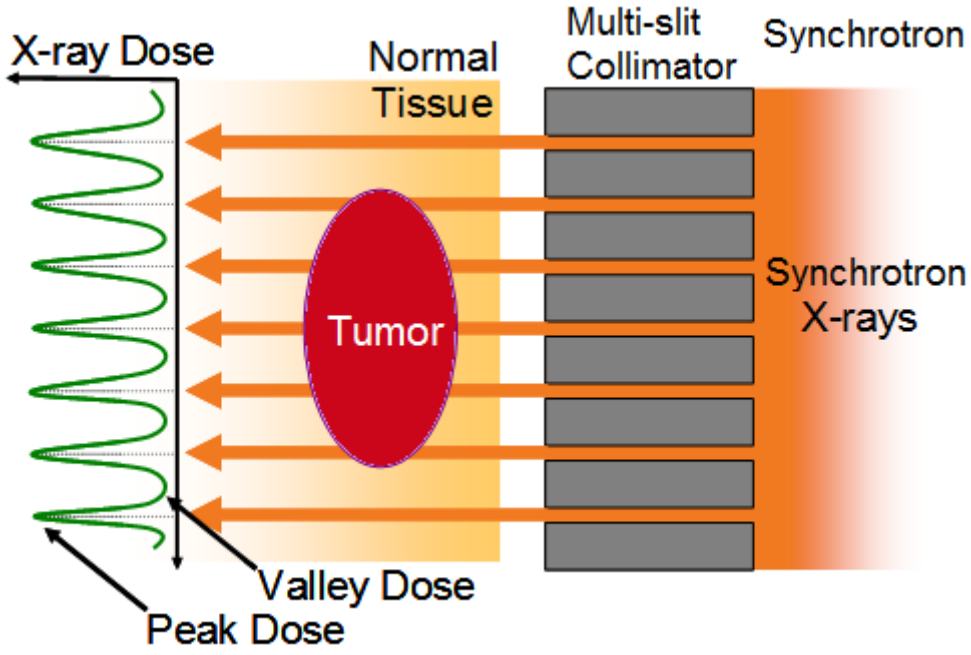

Figure 1.1 A schematic illustration of MRT concept. Broad X-ray beam generated by a synchrotron source passes through a multi-slit collimator producing the microbeam array applied to the tumor. The resulting dose profile includes large doses (peak dose) where microbeams pass and the doses between microbeams (valley dose).

of such conversion, the fluorescence spectra of the irradiated material will possess lines or bands that are associated with optical transitions due to the Sm^{2+} ions as illustrated in Figure 1.2. The intensity of these new bands is proportional to the concentration of Sm^{2+} ions which in its turn is proportional to the radiation dose received by the material. Thus, after suitable calibration, the intensity of certain fluorescence lines or bands characteristic for the Sm^{2+} ions can be directly converted to radiation dose. By suitably imaging the fluorescent emission over the RE-doped plate with a high resolution imaging system (for example confocal microscopy), the fluorescence signal can be converted to the spatial variation in the incident dose.

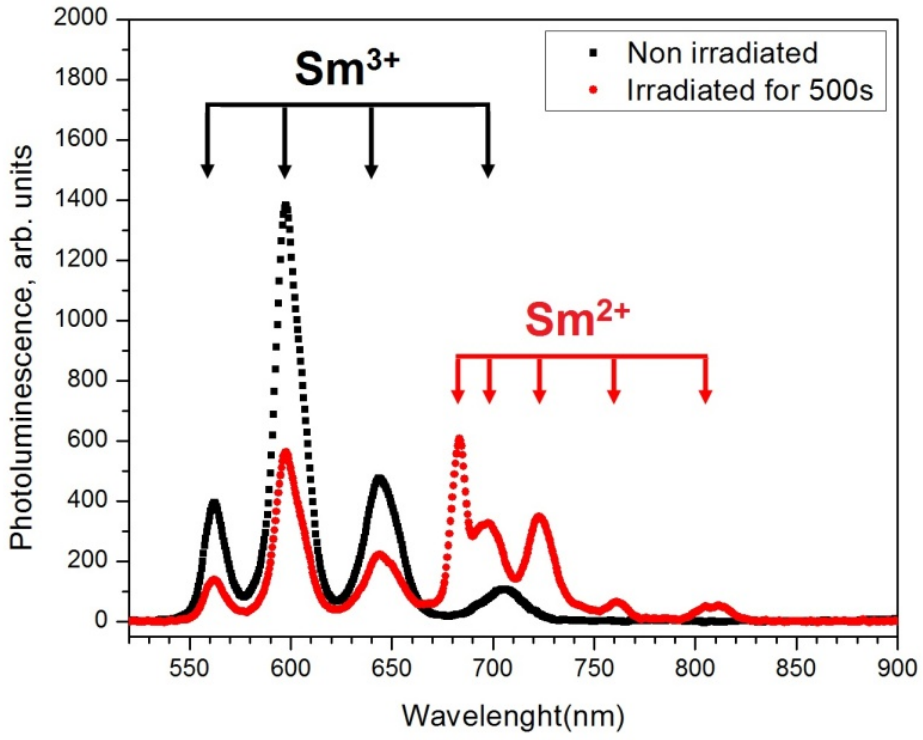

Figure 1.2 Typical room temperature PL spectra of 0.5% Sm^{3+} doped fluoroaluminate glass measured with 405nm excitation light before and after 500 seconds of X-ray irradiation corresponding to a total dose of ~1000 Gy. The irradiation was carried out using synchrotron radiation at the BMIT-BM beamline, Canadian Light Source. The emissions at about 563, 598, 644, and 705 nm in the non irradiated glass can be attributed to the $^4G_{5/2} \rightarrow {}^6H_{5/2,\ 7/2,\ 9/2,\ 11/2}$ transitions of Sm^{3+}, respectively. The five new peaks at 683, 700, 724, 760 and 810 nm observed in the photoluminescence spectrum of the irradiated glass can be ascribed to $^5D_0 \rightarrow {}^7F_{J\,=\,0,\ 1,\ 2,\ 3,\ 4}$ transitions of Sm^{2+}, respectively.

Among the candidates for the dosimeter material, RE doped glasses are particularly promising because glasses are easy to produce with a variety of compositions and easy to work with. Moreover, compared with crystals glasses allow very high resolution fluorescent readout using the technique of confocal microscopy. Among the rare earth ions, Sm^{3+} to Sm^{2+} conversion is of particular interest because the dominant emission bands of Sm^{3+} and Sm^{2+} ions are very easy to distinguish, all dominant bands are situated in the red region of the spectrum, and so there is a good match to silicon based detectors used in optical measurements. Preliminary studies at

University of Saskatchewan showed that among a large variety of Sm doped glasses, only Sm-doped Fluorophosphate (FP) and Fluoroaluminate (FA) glasses show significant X-ray induced Sm^{3+} to Sm^{2+} conversion. The latter glasses were prepared at the Victoria University of Wellington (New Zealand).

1.1.1. Objective

The objective of this thesis is to characterize the optical and thermal properties of Sm-doped FP and FA glasses for application in high-dose, high-resolution X-ray dose measurements suitable for MRT. This thesis aims to investigate processes occurring in Sm-doped FP and FA glasses under X-ray irradiation, so that provide a fundamental knowledge required for developing the prospective detector. To achieve this purpose, there are several project objectives described below:

- Study the photoluminescence signature of both Sm^{3+} and Sm^{2+} ions in FP and FA host glasses to select the most useful fluorescence emission bands to detect the $Sm^{3+} \leftrightarrows Sm^{2+}$ conversion.
- Study the optical absorbance of Sm-doped FP and FA glasses. It should be mentioned here that X-ray irradiation of glasses results in the creation of defects in the glass structure including electron centers (ECs) and hole centers (HCs). These defects cause absorption of light in the UV and the visible regions of the spectrum. This results in undesired transmission loss or photodarkening of the glass. We should examine the effect of photodarkening in the same wavelength range where PL spectra of Sm^{3+} and Sm^{2+} are recorded. The ideal host is the host that would allow the best transmission in the above mentioned range. Optical absorbance study will also give us good information about the nature of X-ray induced defects.

- Find a method for mathematically describing the $Sm^{3+} \leftrightarrows Sm^{2+}$ conversion. So that we could calculate the detector "response" to the dose delivered.
- Record the dose- response curves in order to estimate the dynamic range of the prospective detector.
- Find the optimum concentration of the Sm ion in these glasses that would allow the plate to respond with a good efficiency and respond to larger doses without saturation, and hence achieve a larger dynamic range.
- Investigate the effect of co-doping with different RE ions such as Eu on the dynamic range of the detector.
- Study the effect of other processes such as defect center formation on the dynamic range and the response of the detector.
- Study the spatial resolution of the detector plates by recording the dose profile of microbeams.
- Investigate whether the detector results are reproducible under identical exposure conditions.
- The detector plates should be restorable, that is used many times rather than just once. To achieve this goal, we need to examine processes that would restore the Sm-ion conversion and erase the photodarkening such as thermal treatment (annealing) at high temperatures or optical illumination. The restored samples would be irradiated again to test the reproducibility.

1.1.2. Experimental Techniques

In order to fully characterize the optical and thermal properties of the RE-doped glasses, the following techniques and devices are used:

- X-ray tube: Faxitron cabinet X-ray system with tungsten anode operating at 110 peak kilovoltage (kVp) is used to irradiate most of the samples (refer to the appendix for more details).
- Synchrotron beam application: The BMIT-BM beamline 05B1-1 at the Canadian Light Source (CLS) is employed to create highly collimated X-ray beams similar to those used in MRT (details included in the appendix). Microbeams (50 μm wide and with a centre-to-centre distance of 400 μm) will be generated by passing the beam through an 8 mm thick Tungsten/Air multi-slit collimator. Thus, we can irradiate Sm doped glass plates through the microbeams to investigate if they can record the dose profile with adequate spatial resolution. Synchrotron beam was also used for irradiating some of the samples.
- Confocal fluoroscopic microscopy technique: To read out the $Sm^{3+} \rightarrow Sm^{2+}$ conversion pattern on microbeam irradiated samples and hence obtain the dose profile of microbeams.
- Photoluminescence spectroscopy: This technique was used to record the emission spectra from Sm doped glasses before and after irradiation and during processes such as thermal annealing or optical illumination.
- Optical absorbance spectroscopy: The optical transmittance spectra of Sm-doped glasses are recorded before and after irradiation and during thermal annealing or optical illumination. The induced absorbance spectra are then calculated for further studies.
- Heat treatment: Using a temperature controlled furnace we will anneal the samples at a high temperature for certain duration of time to investigate their erasability.
- Optical illumination: Another possible method for restoring the glass samples is using intense optical illumination at 405 nm.

- Temperature-Modulated Differential Scanning Calorimetry (TMDSC): This technique is used to obtain the temperature dependence of heat capacity $C_p(T)$ and hence the glass transition temperature (T_g).
- Electron spin resonance (ESR) spectroscopy: Since X-ray induced ECs and HCs are paramagnetic, ESR technique is used to study the nature of these defects.

1.2. Organization of the Thesis

This thesis is organized in a manuscript-based style. Published manuscripts are included in Chapter 3, Chapter 4 and Chapter 5 of this dissertation. Chapter 2 provides the theoretical background required for understanding the following manuscript-based Chapters.

In Chapter 2, MRT is introduced and potential dosimeters for MRT are reviewed. Some relevant backgrounds about RE ion (especially Sm and Eu) doped glasses and their optical and structural properties are presented. Then, effects of ionizing radiation on these glasses including the valency conversion of RE ions and the formation of defect centers are reviewed. Electron Spin Resonance (ESR) is also introduced as a method for investigating these defects and its basic concepts are described.

The manuscript included in Chapter 3 evaluates FP and FA glasses doped with trivalent samarium as detector plates for MRT dosimetry. The spatial resolution and the dynamic range of the prospective detector as well as erasability and reusability are studied in this manuscript. Practical methods for calculating the detector response $R(t) = \mathrm{PL}(Sm^{2+})/\mathrm{PL}(Sm^{3+})$ in FP and FA glasses are discussed. Irradiation induced photo darkening and its effect on the response is also examined. Dose-response curves for FP and FA glass plates doped with different concentrations of Sm^{3+} are acquired to investigate the dynamic range and the efficiency of the future detector. The correlation of induced absorbance bands with the the response as well as the effect of

codoping (with Eu^{2+}-ions) on the dynamic range is investigated. Using a confocal fluorescence microscopy technique, the dose profile of microbeams is recorded to investigate the spatial resolution of the potential detector. In order to investigate the erasability and reusability of the detector plates, the plates are subjected to a step by step annealing. This allows us to find the best annealing temperature for erasure of the plates and examine the evolution of induced absorbance, PL spectra and response at different temperatures below or above the glass transition temperature (T_g). A model is suggested for explaining the effects of annealing including the "thermally stimulated enhancement" of the response and the shift in the Sm^{2+} PL spectra which occur at temperatures slightly lower than T_g. The erased plates are irradiated again to verify if they are reusable i.e. the response is reproducible.

Manuscript included in chapter 4, addresses another method for erasure which employs intense optical radiation at 405 nm. This method is tested for erasing the dose profile of Synchrotron-generated microbeams recorded on Sm-doped FP glasses. The erasure processes including Sm^{2+} to Sm^{3+} reconversion and the disappearance of X-ray induced defect centers are investigated by recording the PL, induced absorbance and ESR spectra after each step of illumination. The reusability of the erased samples is also investigated. The underlying physics is studied by combined analysis of induced absorbance and ESR spectra. A model is suggested for explaining the observed phenomena. Finally, the response as a function of different Sm doping concentration is studied at different delivered doses.

The discussions in Chapter 3 and Chapter 4, suggest that a more detailed study of X-ray induced defects is of curtail importance as valency change of Sm ions seems to be correlated with the formation of ESR and/or optically active defect centers. This study can also provide a better understanding of the erasure processes. Therefore, in the manuscript included in chapter 5,

we study defect center formation in a Sm-doped FP glass under the influence of X-ray irradiation. FP glasses are deliberately chosen rather than FA glasses inasmuch as FP glasses are among the more thoroughly investigated glasses, and their properties are much better understood. The investigation is based on ESR and optical absorption spectroscopy. The effect of samarium doping concentration and thermal annealing (at different temperatures) on X-ray induced defect centers, including phosphorus-oxygen hole and electron centers (POHC and POEC), are investigated. A model is developed for explaining the results.

Finally, Chapter 6 concludes and summarizes the contributions of this thesis and suggests some ideas for future studies.

2 Theoretical Background

2.1 Microbeam Radiation Therapy (MRT)

Microbeam Radiation Therapy (MRT) is an experimental form of radiation treatment which is well known for causing less damage to normal tissue while delivering higher doses to tumor in comparison with other kinds of radiotherapy. This is based on the so-called dose-volume effect implying that the normal tissue can tolerate higher doses as irradiated volumes of tissue are made smaller [1]. For this purpose, the synchrotron generated X-ray beam passes through a multi-slit collimator (MSC) and is applied to the tumor target in the form of an array of planar microbeams (typically~20–50 μm width) usually spaced 100–400 μm apart as illustrated in Figure 2.1. It is also apparent from Figure 2.1 that spatial dose distribution has high dose and low dose areas that alternate. While the 'peak dose' (~150–600 Gy) provides lethal radiation for damaging tumors, the 'valley dose' (~3–30 Gy) spares sufficient minimally irradiated tissue [2-4].

MRT was first introduced in 1992 by Slatkin *et al*. [5]. Since then, many studies on animal models including rats, mice and piglets have shown that normal tissue including central nervous system (CNS) tissue can tolerate very high doses (hundreds of Gy) delivered by microbeams. The tissue will maintain its architecture as illustrated in Figure 2.2 and no tissue necrosis will occur [2, 6-8].

The exact mechanisms underlying this 'tissue-sparing' effect are not well understood. One proposed mechanism is that surviving blood vessels in the valley zones repair the tissue microvasculature through an angiogenesis process (Figure 2.3) [8-10]. Dilmanian *et al*. [11] suggested that a "beneficial" bystander effect causes surviving neighboring cells to respond by proliferation, migration, and differentiation which lead to tissue restoration. Crosbie *et al.* [12] suggested that tumor and normal cells have different responses to MRT. Spared tumor tissue

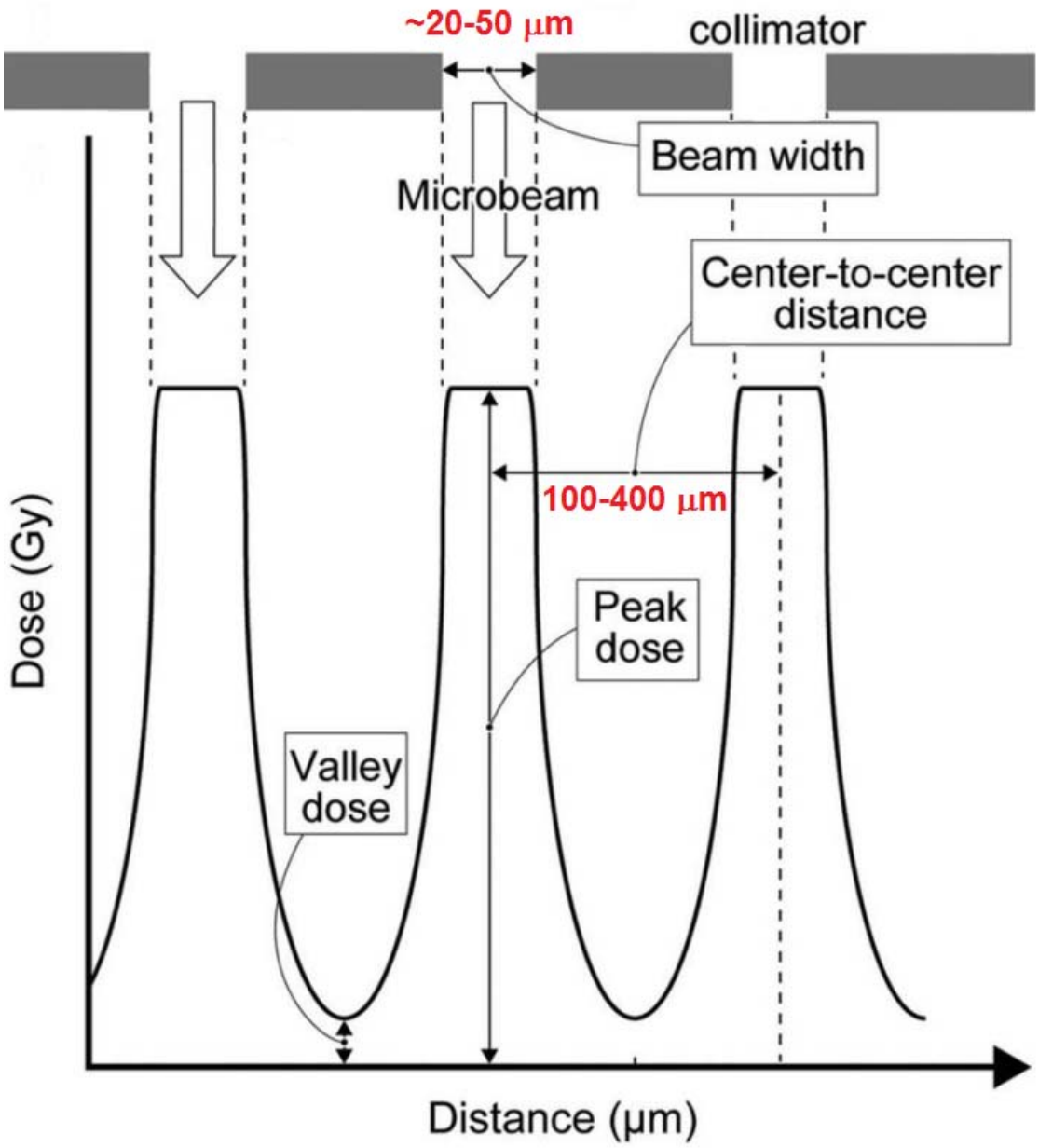

Figure 2.1 Schematic dose profile of microbeams used in MRT. Microbeam geometry parameters such as beam width, center-to-center distance, peak dose and valley dose are introduced in the figure. Microbeams are usually 20-50 μm wide with a 100-400 μm center-to-center distance. Peak and valley doses are typically in the range of 150–600 Gy and 3–30 Gy, respectively. (Adapted from [13]).

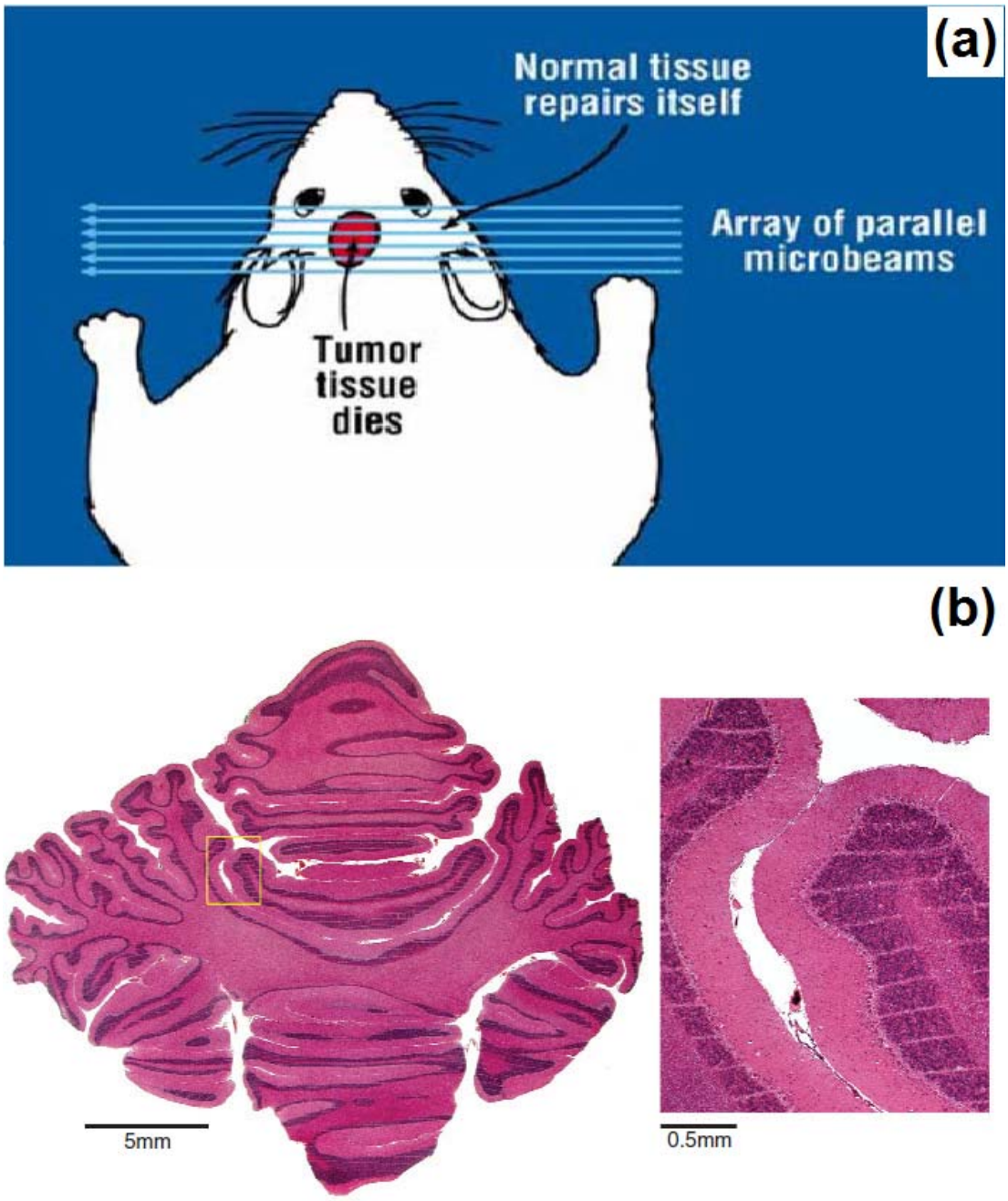

Figure 2.2 (a) Tissue-sparing effect of MRT represented by a schematic diagram. High doses delivered by microbeams ablate the tumor tissue while, normal tissue shows extraordinary resistance to the damage and is capable of repairing the irradiation-damaged zones. (After [8]). (b) Normal CNS tissue subjected to microbeam irradiation. It is apparent that tissue has maintained its normal architecture. Paths of microbeams can be observed as white parallel lines in the inset. (After [2]).

would be ablated by migration of lethally irradiated tumor cells to 'valley zones'. On the other hand, no evidence of migration was observed in normal tissue (Figure 2.4).

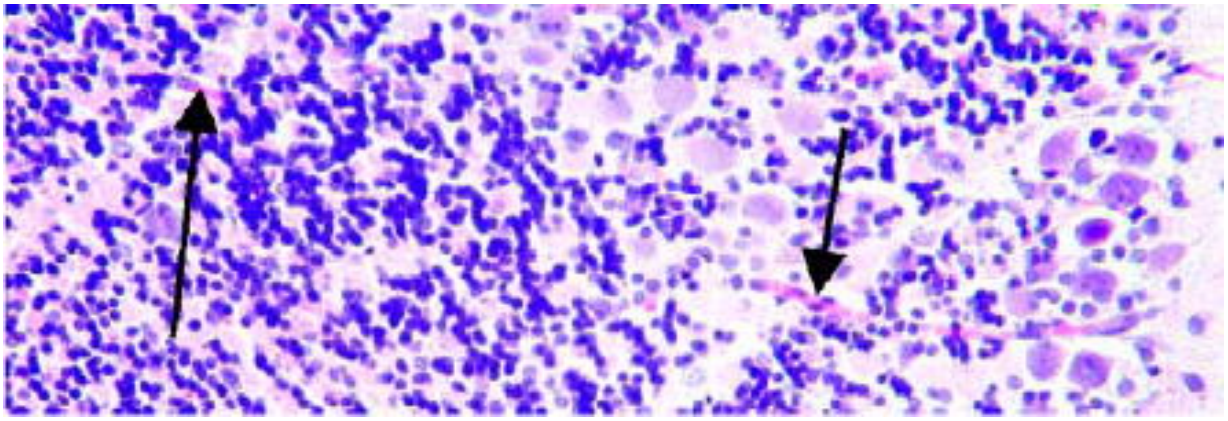

Figure 2.3 Two undamaged blood vessels pass through the pathways created by microbeams (arrows). This can be evidence for the regeneration of tissue microvasculature after irradiation. (After [8]).

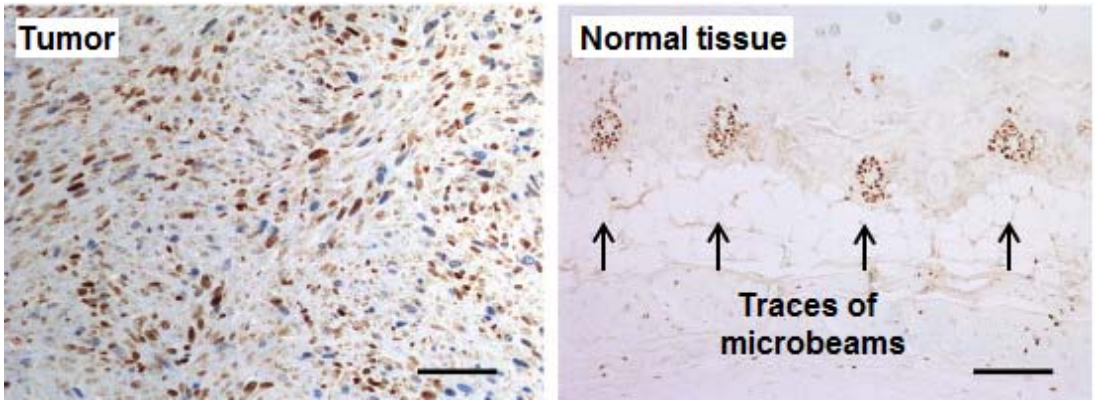

Figure 2.4 Tumor tissue and normal skin tissue from mice 24h after MRT. Tissues were stained with g-H2AX/BrdU to image the DNA damage (brown) and cell proliferation (blue). Peak and valley zones are not distinguishable in tumors because of thorough cell migration and intermingling between irradiation damaged (brown) and surviving (blue) tumor cells. On the other hand, the traces of microbeams (brown) are apparent in normal tissue and no significant cell migration is observed. Scale bar, 100 mm. (Adapted from [12]).

From the above discussion, while the peak dose has to be high enough for maximum damage to the tumors, the valley dose should not exceed a certain threshold to assure that inadequate normal tissue is remained. Thus, the accurate measurement of peak-to-valley dose ratio (PVDR) is of crucial importance for a successful MRT. It should be stressed here that for a successful MRT, high rate doses are also required to avoid scattering of the microbeams by tissue cardiosynchronous movements. However, measuring high rate doses with a large gradient

(hundreds of Grays over several microns) in the whole X-ray energy range of interest for MRT (50-250 keV) is an extremely challenging task. The accurate simultaneous recording of peak and valley doses is beyond the capability of many current detectors. Monte Carlo simulation [14] can predict dose profiles and PVDR, but Monte Carlo simulations need to be verified by experiments before clinical application. Further, dose profile measurements are needed for the proper adjustment of the X-ray source and the collimator. The ideal detector for MRT should provide not only a very wide dynamic range (from ~1Gy to ~500 Gy) and very high spatial resolution (a few microns), but also it should withstand very high dose rates. The response should be reproducible and should not be energy dependent. For clinical practice, uncertainty in measuring the absolute dose can not be more than 3%. Reusability, 3D or 2D dose measurement, tissue equivalency and real-time dosimetry are also distinct advantages. In the following, we will review some commercial and experimental dosimeters with regard to their potential applications in MRT.

2.1.1 Prospective Dosimeters for MRT

2.1.1.1 Gafchromic Film Dosimetry

Film dosimetry has been a promising method for conventional radiation therapy applications over years [15]. However, Gafchromic films have a limited dynamic range and cannot cover the whole range of MRT dosimetry even though they have a spatial resolution as high as 0.8 microns [16]. HD-810 Gafchromic films can respond to high doses over a wide dynamic range (50 -2500 Gy) [17]. Thus, they are promising for measuring the peak dose. On the other hand, more sensitive Gafchromic films including MD-V2-55 (1 Gy to 250 Gy) and EBT (0.2–100 Gy) models[17] are suitable for recording the valley dose. Consequently, for MRT applications usually two films of different sensitivity are employed to measure the peak and valley doses

separately. The readout of the films is usually done with a microdensitometer [18] or a microscope [19]. The calibration curves then will be used to convert the response of the radiochromic film into absolute dose. Although the advantage of this method is its ease of use, the downsides include the requirement of two-time irradiation, instability of the response in time (takes 24 hours to stabilize) and the large uncertainty [18].

2.1.1.2 Ionization Chambers

Ionization chambers are among the most commonly used dosimeters in radiation therapy [20]. An ionization chamber consists of a gas filled chamber with two electrodes with a potential applied between them. Electrodes may have parallel plate or cylindrical geometry. Ionizing irradiation generates ion pairs in the filled gas which will be drifted toward opposite polarity electrodes. The accumulated charge creates an ionization current which is a measure of the total dose received. Although ionization chambers provide precise real time dosimetry, they do not have the high spatial resolution and wide dynamic range required for MRT dosimetry.

2.1.1.3 Alanine Dosimeters

Alanine dosimetry has been a reliable method for conventional radiotherapy. Alanine is an α-amino acid with the chemical formula $CH_3CH(NH_2)COOH$. Alanine detector consists of alanine rods and a binding material. Irradiation with ionizing radiation results in the formation of alanine radicals. The concentration of free radicals which is proportional to the dose absorbed can be measured using an electron spin resonance spectrometer [21-22]. Alanine detectors have the advantage of being tissue equivalent and can measure doses ranging from 5 to 10^5 Gy. Still, they cannot provide spatial resolution required for MRT.

2.1.1.4 Polymer Gels

Polymer gels which consist of monomers such as acrylamide dissolved in a gelatin are commercially available in different formulations. Irradiation with ionizing radiation results in radiolysis of water and formation of free radicals. Monomers will be polymerized when interacting with these radicals. This polymerization reaction is dependent on the absorbed dose. The dose will be then calculated using techniques such as computed tomography, magnetic resonance imaging, vibrational spectroscopy or ultrasound. Gels are tissue equivalent and allow for 3D imaging of the dose distribution in a wide dose range from 0.01 to 100 Gy. However, the pixel size of the imaging system puts a limitation on the spatial resolution, so that the resolution is not typically better than 200 μm [23]. Wong *et al.* tried to overcome this limitation and could improve it to 30 micrometers using a strong magnetic field scanner [24]. However, it is still not meeting the MRT standard. Moreover, commercial polymer gels are not capable of tolerating the MRT very high dose rates without saturation. Another drawback is that gels are very instable in time.

2.1.1.5 Thermoluminescence Detectors

LiF:Mg,Cu,P (MCP-N)-based TL foils and a TLD reader equipped with a CCD camera were used for 2D MRT dosimetry. Light scattering within the detector and the reader properties limited the spatial resolution to ~100μm [25]. Another disadvantage is strong dose rate and energy dependence [26]. AbdulRahman *et al.* [27] showed that the dosimetry based on the thermoluminescence (TL) yield obtained from irradiated Ge-doped silica optical fibers (of ~125μm core diameter) using a Solaro TL reader could provide a very wide dynamic range (with a linear response from 1Gy to 2000Gy and non linear response up to 10000 Gy). But, they did not specify the range of spatial resolution. The TL-yield reproducibility was within 4%. The

energy dependence and dose rate dependence was not studied. It should also be stressed that a significant drawback for TL based detectors is their instability in time.

2.1.1.6 Fluorescent Nuclear Track Detectors (FNTDs)

Dosimetry based on 750 nm fluorescence from radiation induced oxygen vacancy defects in aluminum oxide doped with carbon and magnesium (Al_2O_3: C, Mg) crystals was first introduced in 2006 [28-29] and was originally used for detecting the heavy charged particles and neutrons [28]. Recently, Bartz *et al*. studied the applicability of FNTD detectors for MRT dosimetry and showed that these detectors could provide very high spatial resolution (1 μm). However, these detectors can measure the delivered dose only up to 30 Gy before saturation. Moreover, the detector sensitivity is dependent on the concentration of color centers which varies between different detectors. Another drawback is the high uncertainty (>5%)[30].

2.1.1.7 MOSFET Detectors

Metal-Oxide-Semiconductor Field-Effect Transistor (MOSFET) dosimetry is based on irradiation induced shift in the threshold voltage (V_{th}) of a sandwich type semiconductor device with an insulated (by an oxide layer) floating gate [31]. Carriers created in the oxide layer under ionizing irradiation will be trapped in the silicon substrate. The charge buildup makes a change in threshold voltage between the gate and the substrate. The changes of V_{th} will be digitalized (logical “0” or “1”) [32] in commercial devices. As a result, very special algorithms and energy calibrations are necessary for translating the digital information to absolute dose information. Using these detectors, submicron spatial resolution (< 1μm) can be achieved for MRT. However, disadvantages include the requirement of a very unique readout mode, strong energy dependence, limited dynamic range (0.01-100Gy) and uncertainty [32-34].

2.1.1.8 Silicon Strip Detector

A Silicon diode dosimeter is a p-n junction diode. Irradiation of the diode results in a current of charged particles which generates a signal. If no bias is applied, the generated voltage will be proportional to the dose rate. The absolute dose then can be calculated by integrating the dose rate. However, commercial silicon diodes are not fitting with the particular requirements of MRT dosimetry.

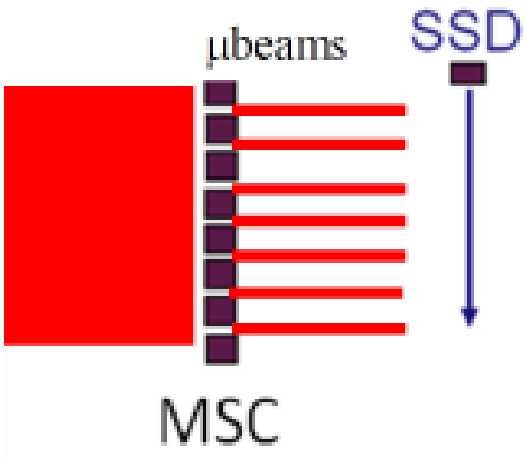

Figure 2.5 Schematic representation of the X-Tream dosimetry system. Single strip silicon detector (SSD) moves across the microbeams at a constant speed. (Adapted from [35]).

A custom designed silicon diode based dosimetry system (called X-Tream) was used for real-time MRT dosimetry at European Synchrotron Radiation Facility (ESRF) [35-37]. A single thin microstrip silicon detector (SSD) will be scanned with a constant speed across the microbeam array as shown in Figure 2.5. The spatial resolution is equal to the depletion width of the detector (10–12 µm). This method provides on-line and real time dosimetry and can be used for a fast pre-treatment quality assurance. However, for absolute dose measurement, corrections and calibrations should be improved. Strong energy dependence should be corrected and the dose rate dependence has to be investigated.

2.1.1.9 PRESAGE™ Radiochromic Plastic

A new dosimetry method for MRT based on irradiation-induced color change of radiochromic polymer named PRESAGE™ is currently under investigation. The color change of PRESAGE™ rod which is proportional to the absorbed dose can be readout using optical computed tomography (in 3D) [38-39] or fluorescent microscopy [40].

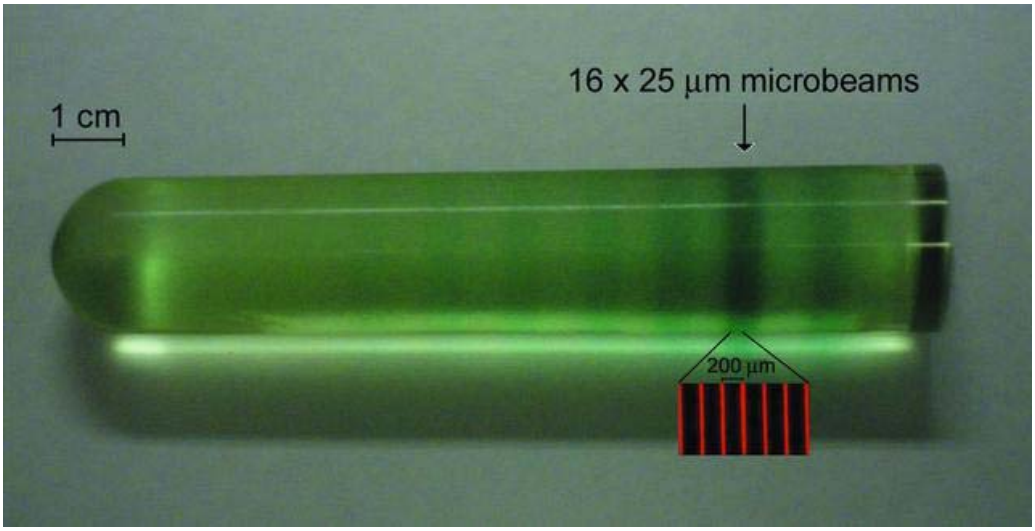

Figure 2.6 A PRESAGE rod with sections irradiated under different intensities of microbeams. The section indicated by the arrow includes traces of 16 microbeams (each 25 µm wide), not easily discernible with the human eye. Insert: fluorescence scan of that section (magnified 10×). (After [40]).

The spatial resolution which is ~40 µm is not yet adequate for use in MRT and calibration for measuring the absolute dose is under investigation.

2.1.1.10 High Resolution Optical Calorimetry

Ackerly *et al*. [41] introduced a new concept for MRT dosimetry based on the changes in the refractive index of a water bath heated by X-ray illumination. The rate of refractive index changes from which the absolute absorbed dose can be calculated will be mapped using reference image topography. This method can provide the required resolution (~1 µm) in 2D.

However, the main drawback is the uncertainty (~10%) caused by thermal diffusion of water which changes the heat distribution during its measurement.

2.1.1.11 Radiophotoluminescence Glass Dosimeters

Maki *et al*. [42] have recently introduced a new dosimetry system which can achieve a spatial resolution as high as ~3 μm. The irradiated silver activated phosphate glass produces radiophotoluminescence under UV excitation which is readout using a confocal laser microscope. However, obstacles such as low sensitivity and background noise have to be overcome and are under investigation.

2.2 Rare-Earth (RE) Ion Doped Glasses

Seventeen elements in periodic table are known as rare earth elements including fifteen elements positioned in lanthanides group plus scandium (Sc) and yttrium (Y). Rare earth ions specifically when introduced into a host solid operate as luminescence centers [43-44]. Glasses are known as excellent host materials for rare-earth ions for applications in fiber lasers [45-46], optical amplifiers and telecommunication [47-48] and high density optical memories [49].

2.2.1 Electronic Structure of RE Ions

RE ions are characterized by a Xe core and an incompletely filled 4f electron shell. $4f^n$ shell lies within the outer $5s^2$ $5p^6$ filled shells and therefore is partly shielded from surrounding host glass ions (Figure 2.7). However, it is still affected by ligand-field splitting [50]. The resulting Energy-level structure can be approximated using “Dieke diagram” originally obtained in the $LaCl_3$ host by Dieke [51] and further developed by Carnall [52]. Since the effect of host ions is weak, the same diagram can be used for different host materials with a good precision. Optical absorption transitions between levels inside 4f shell are strongly forbidden by the parity selection

rule. However, theses ions show very sharp spectral lines which can be explained by Judd-Ofelt theory [53-54].

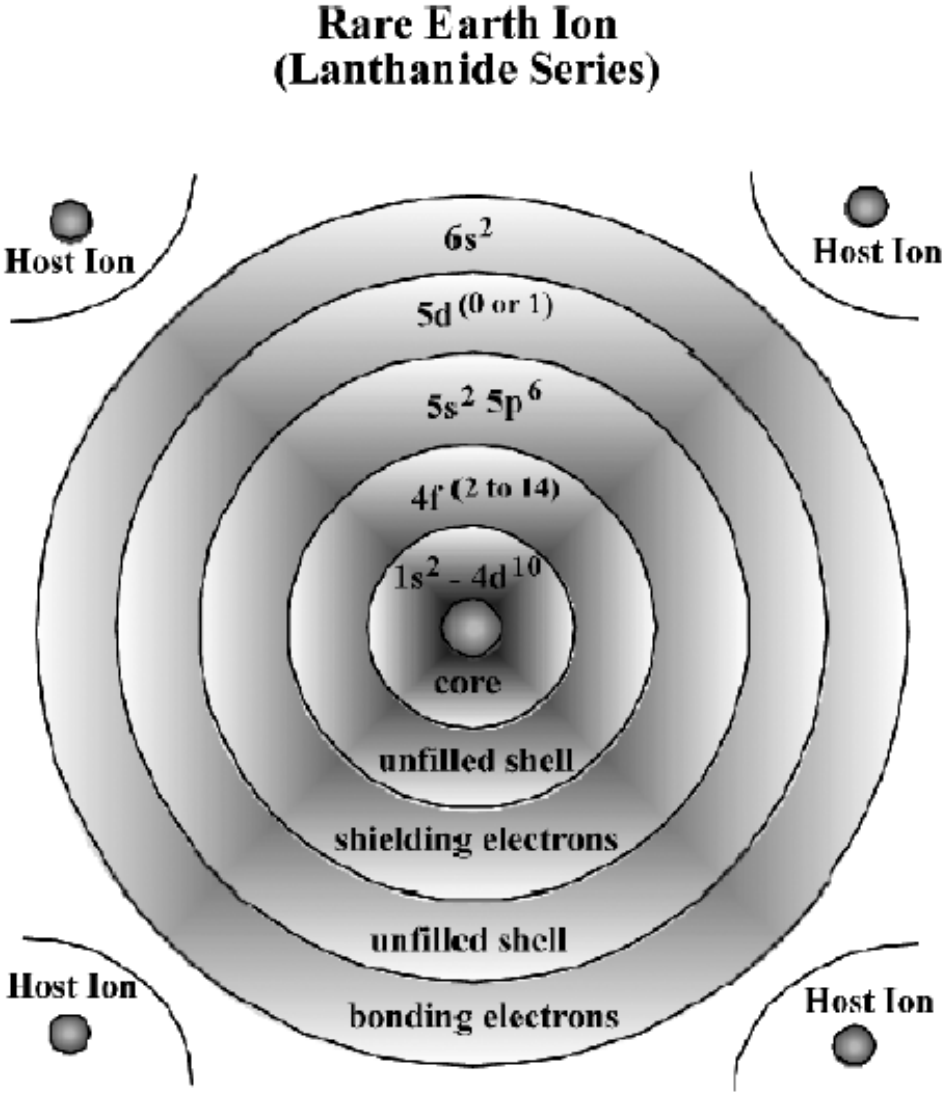

Figure 2.7 Electronic configuration of rare earth ions: 4f shell is shielded from surrounding host glass ions. (After [55]).

2.2.2 Samarium and Europium Ions

Samarium and Europium ions can exist in divalent or trivalent state in glasses. These ions are most stable in their trivalent state in glasses that have been prepared by conventional glass melting techniques. The electronic configuration of Sm^{3+} ion is [Xe] $4f^5$ with a free ion ground

state of $^6H_{5/2}$. Sm^{3+} has an odd number of electrons in the 4f shell and therefore is regarded as a Kramer's ion, which means that energy levels of this ion have double degeneracy caused by the ligand-field. Sm^{2+} and Eu^{3+} ions have [Xe] $4f^6$ electron configuration with $^7F_0$ as the lowest state and $^5D_0$ as the lowest excited state. These ions are non-kramer ions as they have an even number of electrons in their 4f shell. This results in a series of doublet and singlet energy levels. Eu^{2+} is [Xe] $4f^7$ with a free ion ground state of $^8S_{7/2}$. The first excited state is $4f^65d$.

2.2.2.1 Emission Spectra (Photoluminescence)

Sm^{3+} ions show $^4G_{5/2} \rightarrow {}^6H_{5/2,\ 7/2,\ 9/2,\ 11/2}$ transitions corresponding to luminescence bands at about 563, 598, 644 and 705nm respectively [56-59] as demonstrated in Figure 2.8.

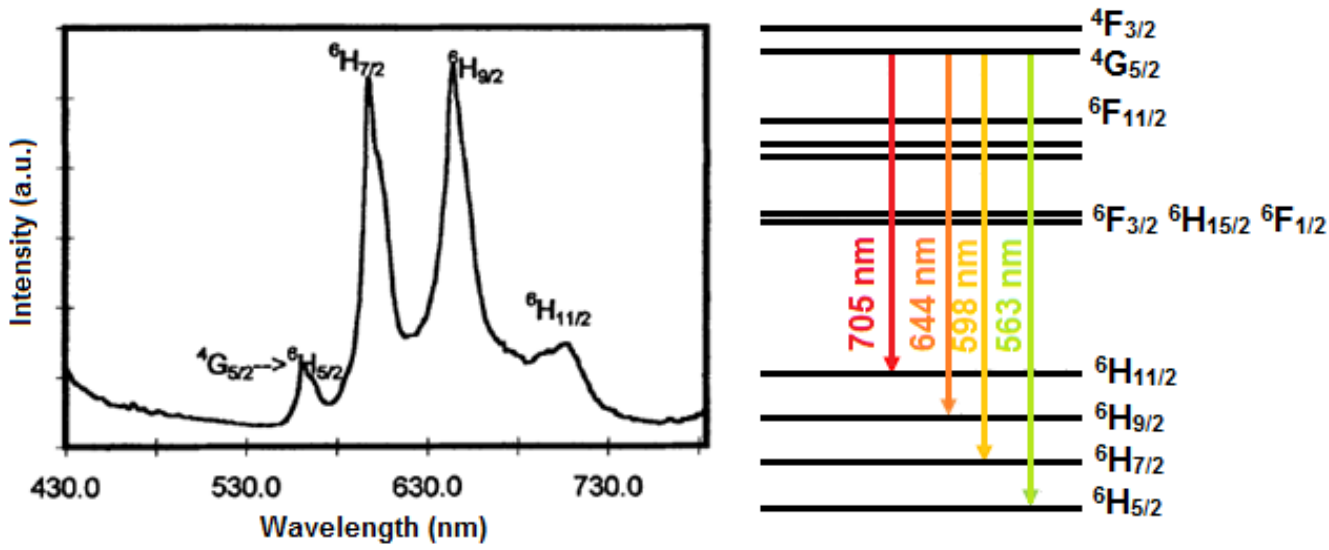

Figure 2.8 Fluorescence spectrum and energy level diagram for emission of Sm^{3+} ions in phosphate glass. (Adapted from [60]).

The photoluminescence of Sm^{2+} ion is associated with the $4f^55d$-$^5D_0$ non-radiative relaxation and with the 4f →4f radiative transitions ($^5D_0 \rightarrow {}^7F_J$; J= 0, 1, 2, 3, 4) in red corresponding to luminescence peaks at around 683, 700, 724, 760 and 810 nm respectively. These ions also show 5d →4f transitions as shown in Figure 2.9.

^5D_J (J=0, 1, 2) to ^7F_J (J=0-4) transitions of Eu^{3+} ions correspond to strong emissions at 500-600nm. Eu^{3+} ions also show a wide band attributed to $4f^5 5d^1$-$4f^6$ transitions [61-63]. On the other hand, Eu^{2+} shows transitions in ultraviolet including a broad emission band associated with the transition from $4f^6 5d^1 \rightarrow 4f^7$ (~400nm) and a sharp line at 360nm due to parity forbidden $4f^7 \rightarrow 4f^7$ ($^6P_{7/2}$-$^8S_{7/2}$) transition. Energy diagram for Eu^{2+} and Eu^{3+} ions is shown in Figure 2.10 [64].

It should be stressed here that in the case of Sm, all dominant bands are situated in the red region of the spectrum, and so there is a good match to silicon based detectors used in optical measurements.

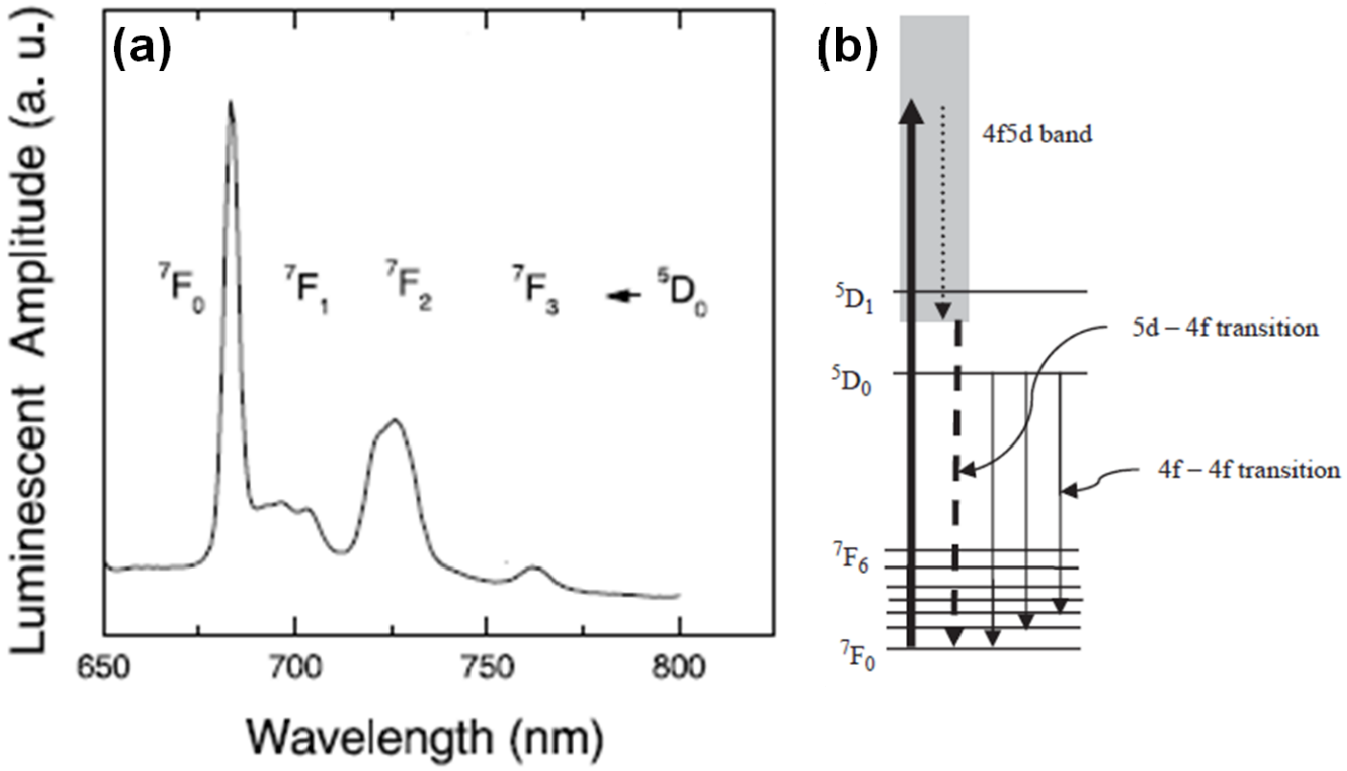

Figure 2.9 Photoluminescence spectrum (a) (adapted from [63]) and Energy diagram (b)(after [65]) for Sm^{2+} ions in a host glass.

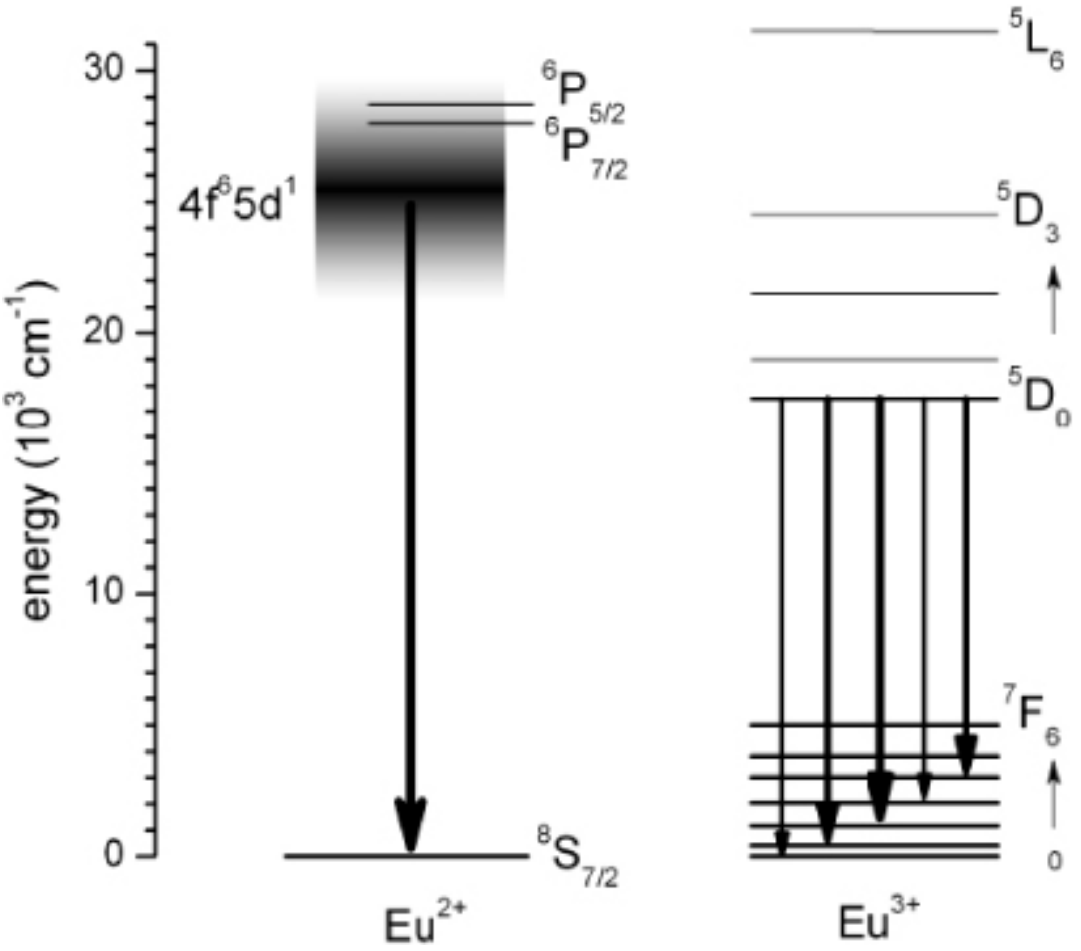

Figure 2.10 Energy diagram for Eu^{2+} and Eu^{3+} ions. (After [66]).

2.2.2.2 Excitation Spectra

Excitation spectra can be used to determine the excitation wavelength required for obtaining the maximum photoluminescence. It is apparent from Figure 2.11, that an excitation wavelength of 405 nm can excite both Sm^{2+} and Sm^{3+} ions if present. Another possible choice for exciting both ions would be around 470 nm. For some specific applications, a wavelength of 350 nm (for example) may be selected to excite only an Sm^{2+} spectrum [67].

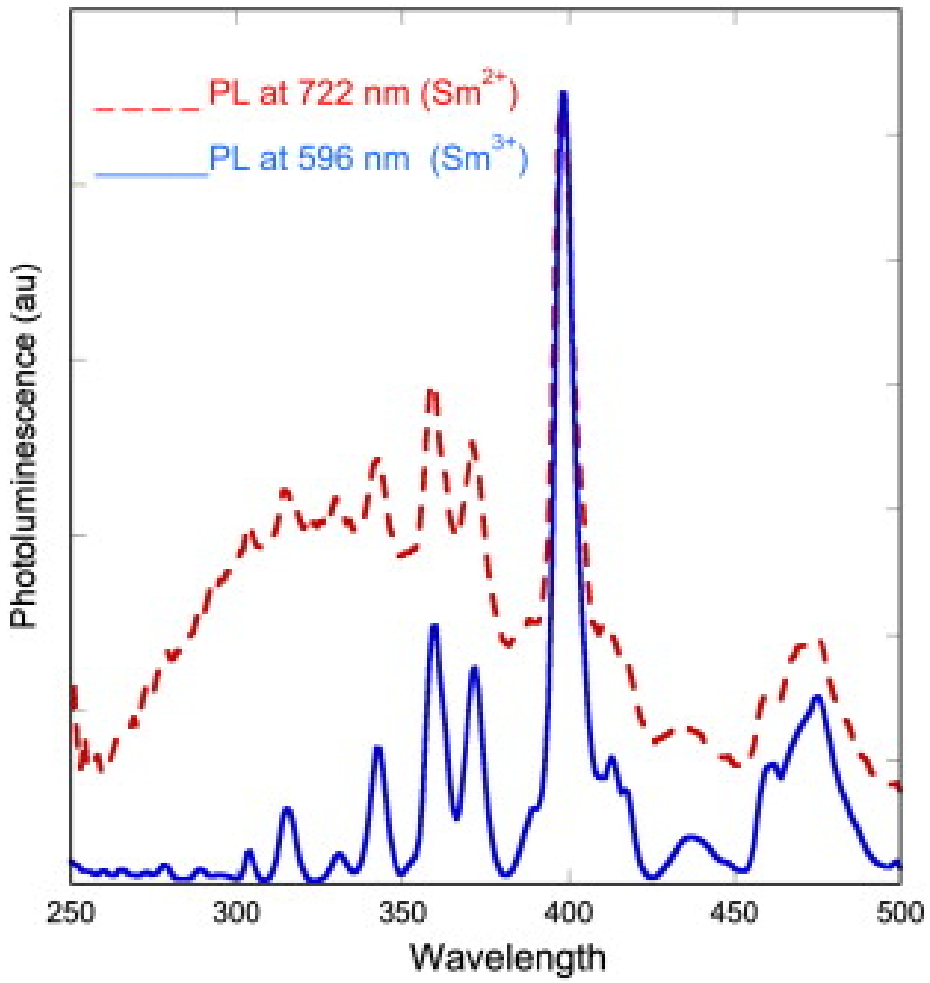

Figure 2.11 Excitation spectra of Sm^{3+} and Sm^{2+} in fluoroaluminate glass with emissions at 596 nm and 722nm, respectively. (After [67]).

2.2.3 Effect of RE Doping on the Glass Structure

In glasses such as phosphate glasses which have a high concentration of non-bridging oxygen, the incorporation of RE ions is more convenient. When RE^{3+} ions are comprised to the glass matrix, they take the place of a network modifier (such as Sr^{2+}) and will be surrounded by non-bridging oxygen and the structural bridging oxygen (Figure 2.12) [68]. In glasses like pure silica with a lack of non-bridging oxygen, RE ions cluster which results in the reduction of radiative transitions.

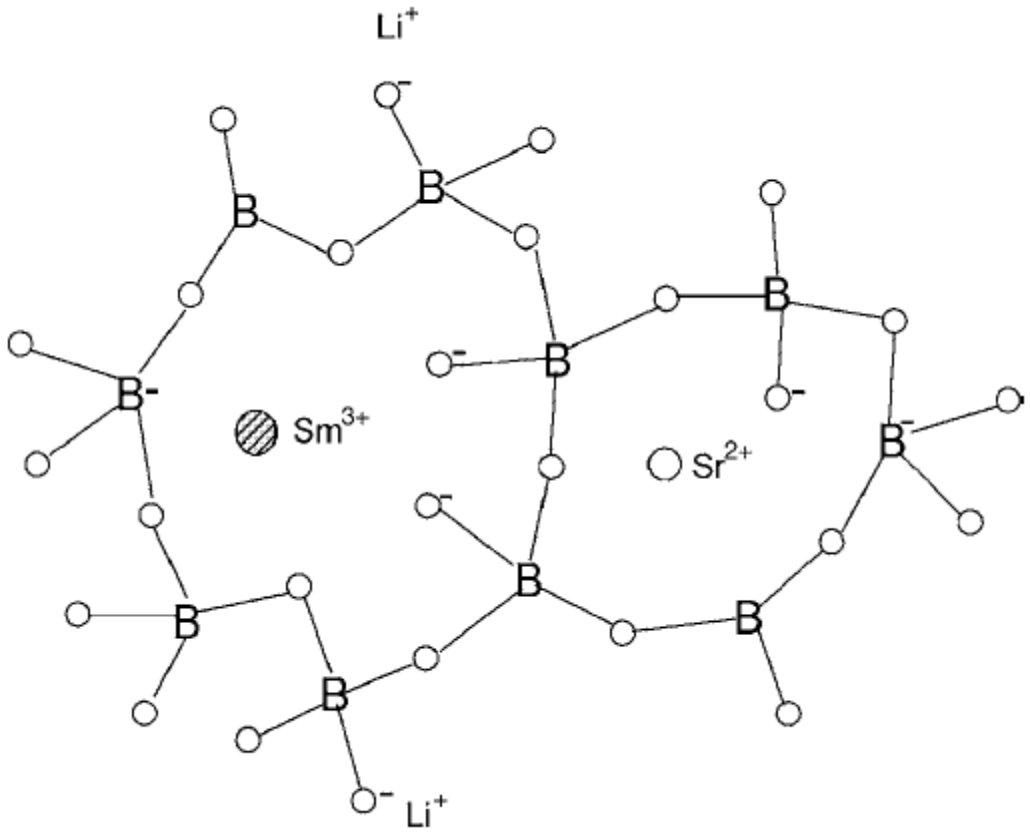

Figure 2.12 The proposed model for the structure of Sm^{3+} doped $Li_2O–SrO–B_2O_3$ glass. It is suggested that non-bridging oxygen and the structural bridging oxygen of the borate groups surround the Sm^{3+} ions. (After [68]).

2.2.4 Valency Conversion of RE Ions under High Energy Irradiation

It is well known that, in many host glasses, the trivalent RE^{3+} ions can be converted to their divalent form (RE^{2+}) upon exposure to high energy radiation. The valence change of Sm^{3+} and Eu^{3+} ions to their divalent form (Sm^{2+} and Eu^{2+}) can be optically detected because the dominant emission bands of trivalent and divalent forms of these ions can be readily distinguished. The reduction of these ions has been reported in fluorophosphates [69], fluoroaluminate [49, 62, 70], sodium aluminoborate [58], alkaline earth borophosphate ($SrO–BaO–P_2O_5–B_2O_3$) [71], sodium borate[72], lithium barium borate ($Li_2O–BaO–B_2O_3$)[73], $Li_2O–SrO–B_2O_3$[68], oxyfluoroborate [74], borosilicate [75], aluminoborosilicate [76], $Al_2O_3–SiO_2$ [65, 77] and fluorozirconate [78]

glasses under X-ray, gamma, beta and femtosecond laser irradiation. On the other hand, it is reported that $Sm^{3+} \rightarrow Sm^{2+}$ conversion could not be detected in Sm^{3+} - doped fluorochlorozirconate glasses and glass-ceramics, SiO_2–NaO–Al_2O_2–LaF_3–PbF_2-SmO_3 glasses, LaO_3–$B2O_3$–GeO_2–SmO_3 glasses and borophosphate glasses prepared from the $SrBPO_5$ and $BaBPO_5$ polycrystalline materials even after irradiation to very high doses [79]. It's worth mentioning here that the nature of host composition has a significant effect on reducing Sm^{3+} ions. For example, Sm^{3+}-doped silica glasses and Sm^{3+}-doped silicate glasses containing metal oxides such as Na_2O, B_2O_3, and TiO_2 do not show any reduction of Sm ions while, Al_2O_3-containing silicate glasses show the reduction of Sm^{3+} ions under irradiation with femtosecond laser [65].

$RE^{3+} \rightarrow RE^{2+}$ conversion is usually reversible. It has been observed that optical-illumination decreases the fluorescence intensity of the Sm^{2+} ions (photo-bleaching)[80]. Moreover, annealing the glass at high temperatures may cause the effect of converting Sm^{2+} back to Sm^{3+} [77].

2.2.5 Photodarkening Effect and Defect Centers

Almost all glasses exhibit photodarkening when they are irradiated with X-rays [61, 68, 73, 77, 81-83]. In other words, X-ray irradiation leads to creation of several optical absorption bands in the glass **(**photo-induced absorption). This results in undesired transmission loss of the glass**.** The rate of darkening is a function of intensity of the exciting beam, duration of irradiation and the host material [79, 84].

Usually, photodarkening is attributed to creation of defect centers in the glass. Irradiation of glass results in the creation of free electrons and holes which can be trapped by precursors in the glass leading to the formation of defect centers including electron centers (EC) and hole centers (HC), respectively. Electronic transitions of these defects often cause high absorbances in the

UV and the visible region [85-87]. As these centers are paramagnetic, the technique used to investigate the nature of them is generally Electron Spin Resonance (ESR) method [88-90]. The photodarkening is usually reversible. Annealing or illuminating the sample may reduce the induced absorption, probably by removing defect centers [49, 91-92].

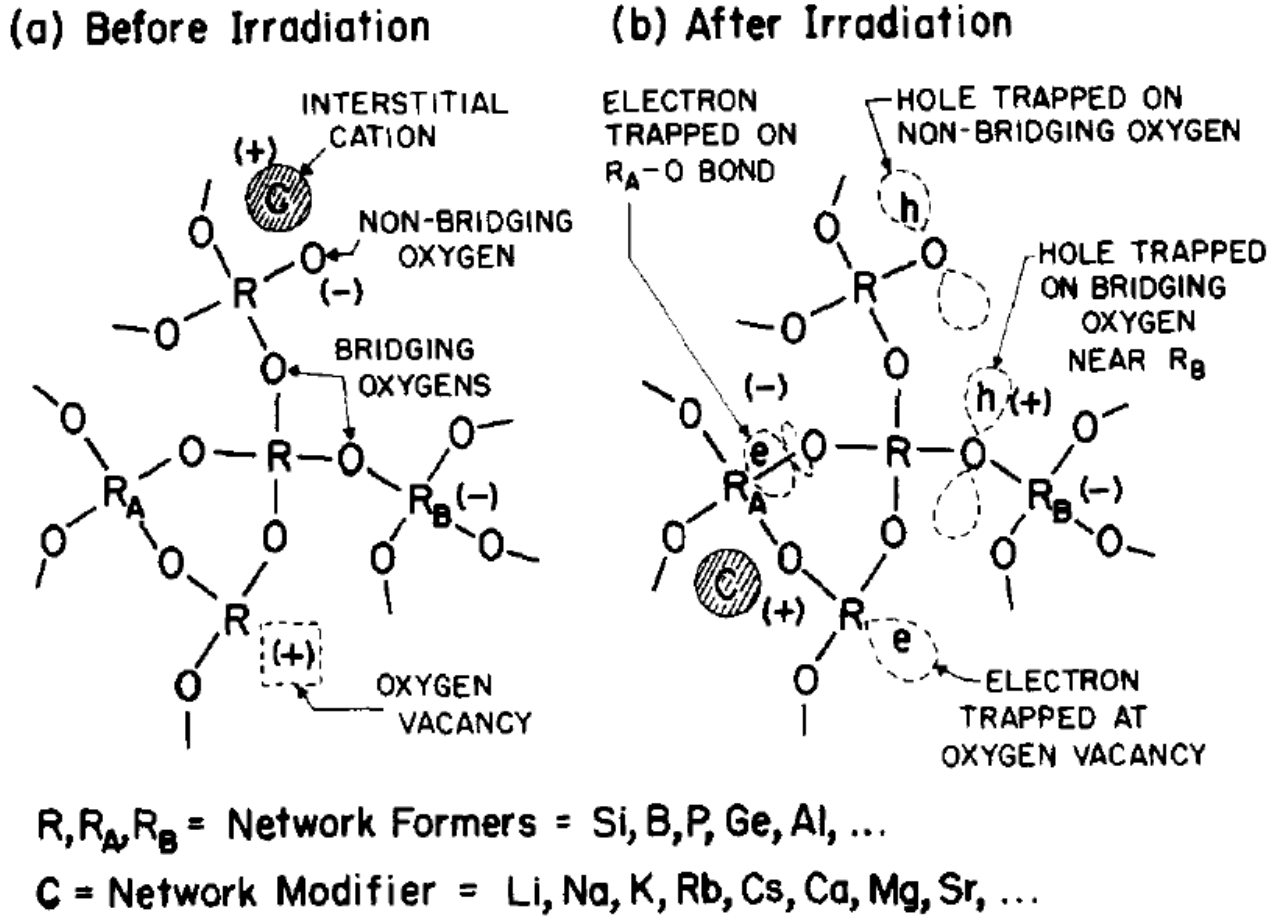

Figure 2.13 Radiation-induced defects in oxygen containing glasses. (After [90]).

Generally, radiation-induced defects in oxygen containing glasses include oxygen-associated trapped hole centers and oxygen-vacancy-associated trapped electron centers as well as interstitial cation and anion associated electron and hole centers.

Figure 2.13 schematically demonstrates the formation of several types of defect centers in oxygen containing glass. Figure 2.13 (a) shows the pre-existing precursors such as oxygen

vacancies, substitutional impurities, bridging and non-bridging oxygen in the glass matrix before irradiation. Figure 2.13 (b) shows the electron and holes trapped on precursors (defect centers) after irradiation. Oxygen-associated trapped hole centers usually form when a network modifier (C= Li, Na, K, Rb, Cs, Ca, Mg, Sr, Sm, Eu,…) is added to the glass matrix. This addition can lead to creation of "non-bridging oxygens" near the network modifiers as shown in Figure 2.13 (a). These non-bridging oxygens may be looked up on as negative point defect which can trap holes (Figure 2.13(b)). Holes may also be trapped on bridging oxygen as illustrated in Figure 2.13. This happens when network formers with three valence electrons such as B or Al (R_B) are found in tetrahedral coordination. As a result, the complex $(R_B)O_4$ may look like a negative point defect which is a hole trap [90]. Oxygen-associated trapped hole centers are usually referred to as POHC [93-96], BOHC [68, 74, 76, 90, 97] and Al-OHC [65, 77, 98-99] depending on the structure of the glass.

Interstitial cations and anions themselves may serve as electron traps or hole traps, respectively. Another kind of electron trap consists of oxygen vacancies in tetrahedral coordination. The resulting complex looks like positively charged point defect which may trap electrons. Electron traps may also form when a network modifier (R_A) with a greater electron affinity is doped into tetrahedral network of R. Electron can be trapped in R_A-O orbital. These centers stabilize when an interstitial cation is present nearby (Figure 2.13) [90].

The total defect concentration (any type) usually saturates at a value $\sim < 10^{18}$ cm^{-3} upon high energy irradiation at room temperature. Saturation concentration has an inverse dependence on temperature and is a function of glass composition [100-101].

2.2.5.1 Defect Centers in Phosphate Glasses

Oxygen-associated trapped hole centers in phosphate glasses are usually referred to as POHCs (Phosphorus-Oxygen Hole Centers). Two different types of POHCs have been reported in phosphate containing glasses. One type of POHC is characterized by an unpaired spin sharing between the two non-bridging oxygens. Another variant of POHC in which the unpaired spin is not shared, was reported to be stable only at low temperatures by Griscom [102]. However, Origlio [95] *et al.* showed that this structure can be observed at room temperature also. Origlio named these two variants r-POHC and l-POHC, respectively (Figure 2.14).

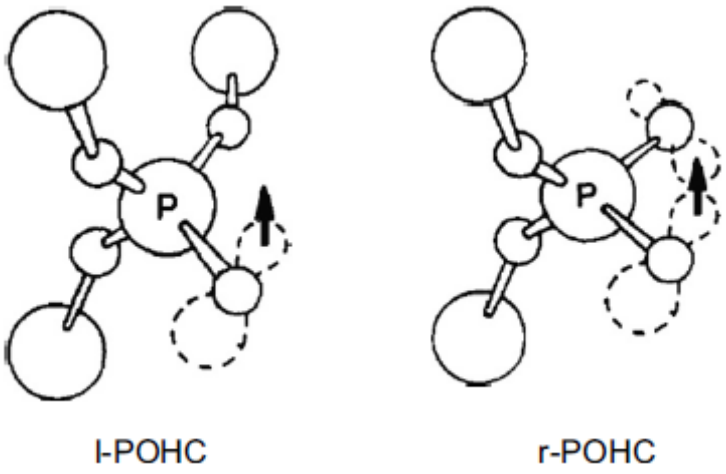

Figure 2.14 Suggested structures for the r-POHC (right side) and l-POHC (left side) defects. Small spheres symbolize oxygen atoms, while large spheres represent phosphorus or silicon. (After [95]).

Oxygen-vacancy-associated trapped electron centers in phosphate glass include defects such as PO_2, PO_3 and PO_4 complexes (shown in Figure 2.15) which consist of electrons trapped on phosphorus precursors. These defects were referred to as P4, P1 and P2 defects by Griscom, respectively [93, 95, 102]. We refer to these defects as POEC in this thesis.

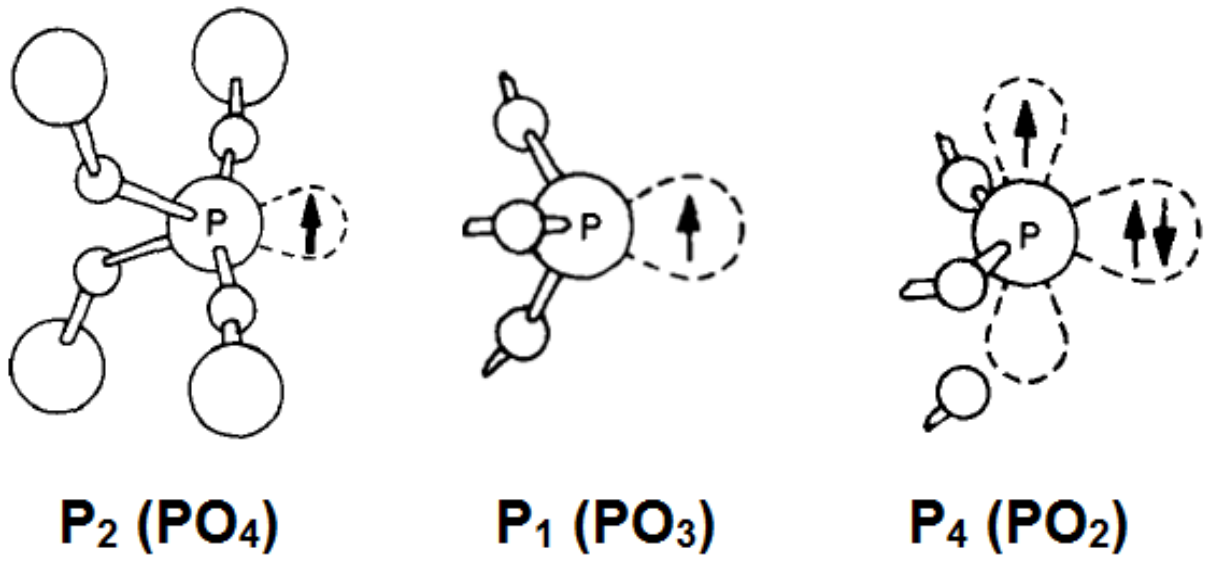

Figure 2.15 Models for the P1, P2, and P4 defect centers. (Adapted from [102]).

2.2.5.2 Electron Spin Resonance (ESR) Spectroscopy

Electron spin resonance (ESR) is a technique for investigating paramagnetic centers. Fundamentally, ESR is based on the absorption of the microwave radiation by unpaired electrons in the presence of an applied magnetic field. When an electron is subjected to an external magnetic field, its energy levels split due to Zeeman effect [103]. Electron energy levels are described by the *spin Hamiltonian*:

$$\hat{H}_s = g\mu_B B\,\hat{\boldsymbol{S}}_z \qquad (2.1)$$

where g is called the g-value ($g_e = 2.00232$ for a free electron [104]), μ_B stands for the Bohr magneton which has a value of 9.274×10^{-28} J G^{-1} if we measure the magnetic field strength (B) in Gauss, and $\mathbf{S}_z$ is the component of the spin angular momentum operator in the field direction. Since, a free electron can exist in one of two quantum states $\left|+\tfrac{1}{2}\right\rangle$ and $\left|-\tfrac{1}{2}\right\rangle$ ($m_s = \pm$ ½), only two energy states can be found from the above equation:

$$E\pm = \pm\tfrac{1}{2} g\mu_B B \qquad (2.2)$$

The splitting ΔE between these two energy levels is equal to $g\mu_B B$. Applying a microwave radiation ($h\nu_0$) which matches ΔE, results in the absorption. Thus, we obtain the most basic equation of ESR, i.e. the resonance condition:

$$h\nu = g\mu_B B \tag{2.3}$$

In practice, usually the magnetic field is scanned while the microwave frequency is held at a constant value. Typically, an X-band microwave with a frequency of $\nu_0 \sim 9.5$ GHz is used. By increasing the magnetic field strength B, the gap between the energy levels of $m_s = +1/2$ and $m_s = -1/2$ is widened until it matches the energy of the microwave radiation $h\nu_0$ as shown in Figure 2.16 . At this point, the unpaired electrons can be subject to a transition between these two states. It should be stressed here that, microwave energy can induce each absorption or emission. Absorption and emission are proportional to the spin populations in the lower state (N_-) and upper state (N_+), respectively. Thus, the net absorption of energy is proportional to $N_- - N_+$. We measure the latter value (the net absorption) while recording the ESR spectra.

It should be noted that practically, the first derivative of absorption is recorded (Figure 2.16) to achieve a better resolution. For this purpose, the magnetic field is typically modulated with a frequency of 100 kHz. The modulation amplitude is usually adjusted at a value equal to one-third of the line-width [105-107].

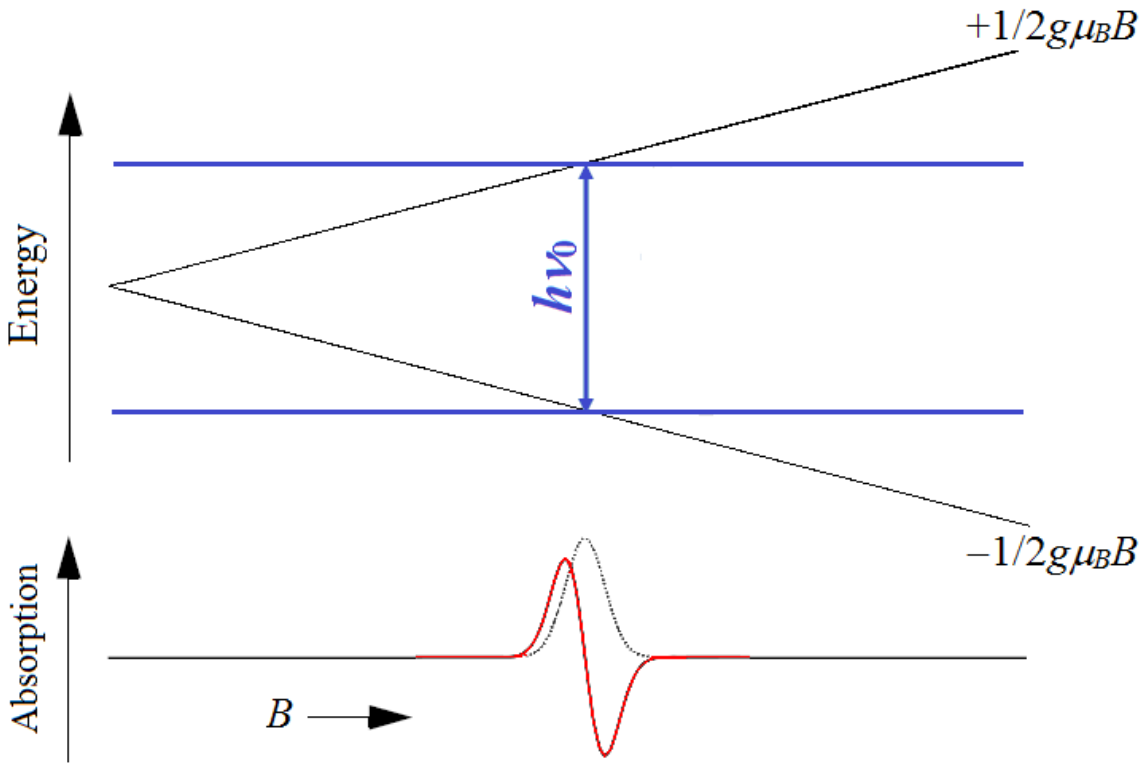

Figure 2.16 Variation of energy levels of an unpaired electron as a function of the applied magnetic field. $h\nu_0$ is the microwave energy which is held at a constant value. Resonance occurs when the gap between the energy levels matches the energy of the microwave radiation. (Microwave energy will be absorbed by transitions between these two energy levels). Absorption is shown by dashed lines. The first derivative of absorption (red line) is recorded as the ESR signal.

2.2.5.2.1 Saturation

In thermal equilibrium, N_+ and N_- are determined by the Boltzmann distribution:

$$N_+ / N_- = \exp(-\Delta E / kT) \qquad (2.4)$$

Under microwave radiation with sufficient power supply, the population of upper level increases until $N_+ = N_-$, i.e. the net absorption (ESR signal) tends to zero. This is called "saturation".

However, the system can return to thermal equilibrium by losing the energy to the lattice through a non-radiative process called "spin-lattice relaxation". If spin lattice relaxation characteristic time (T_1) is short enough, i.e. in case of strong spin-lattice coupling, the spin system will lose

energy as rapidly as the radiation field supply it; thus remains in thermal equilibrium. On the other hand, weak coupling (long T_1) can easily lead to saturation. In practice, the saturation can be avoided by adjusting the power supply [106, 108-109].

2.2.5.2.2 Hyperfine Splitting

The above approach is over simplified. We should consider that the unpaired electron spin may interact not only with external magnetic field but also with magnetic dipole moments of nuclei in its vicinity. The latter is called the hyperfine interaction and splits electron spin levels into $(2I + 1)$ sublevels where I is the nucleus spin. This results in splitting of the resonance line[106]. Hyperfine interaction adds a second term ($a\,\vec{\boldsymbol{I}}.\vec{S}$) to the spin Hamiltonian:

$$\hat{H}_s = g\mu_B B\,\hat{\boldsymbol{S}}_z + a\,\vec{\boldsymbol{I}}.\vec{S} \qquad (2.5)$$

where, a is in energy units (joule) and is called the hyperfine coupling parameter. In case of interaction with a spin-1/2 nucleus (supposing small hyperfine interaction, $a << g\mu_B B$) the energies become:

$$E = \pm\tfrac{1}{2} g\mu_B B \pm \tfrac{1}{2} a \qquad (2.6)$$

These energy levels are shown Figure 2.17. Practically, only $\Delta m_S = \pm 1$, $\Delta m_I = 0$ transitions will be observed as ESR signal. Thus, resonance occurs two times according to two transitions. In this case, the splitting between the two ESR signals would be $A = \dfrac{a}{g\mu_B}$ (in Gauss unit) as illustrated in Figure 2.17 [106, 110].

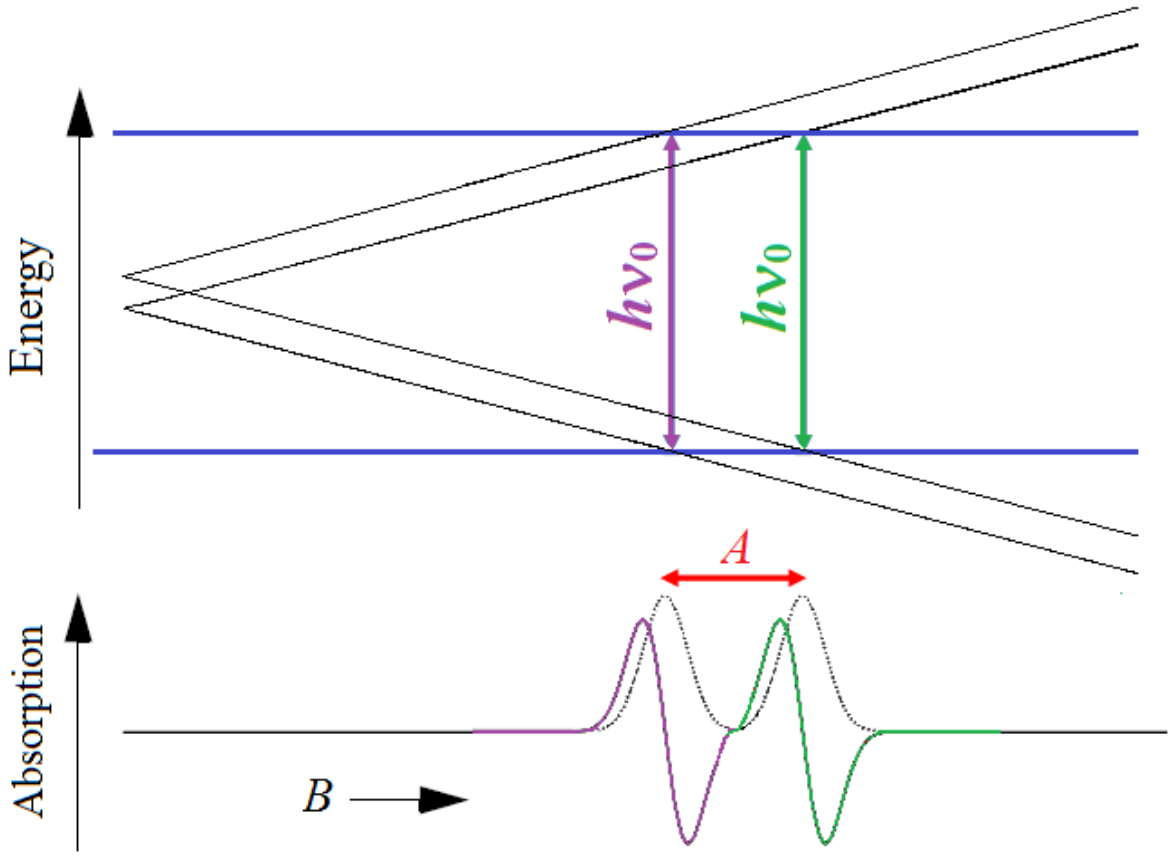

Figure 2.17 Splitting in energy levels and ESR signal due to interaction with the local magnetic field of a nearby spin-1/2 nucleus. The gap between energy levels will match the energy of the microwave radiation ($h\nu_0$) two times (shown by purple and green arrows) as we scan the magnetic field. Thus, microwave energy will be absorbed two times by two allowed transitions (corresponding to two absorption peaks shown by the dashed lines). Thus, two ESR signals (purple line and green line) corresponding to the first derivatives of these two absorptions will be observed. These two signals are splitting by $A = a / (g\mu_B)$.

2.2.5.2.3 Lineshapes

Gaussian and Lorentzian lineshapes are usually employed to describe the shape of ESR lines [105-106, 110]. Expressions for these lines in terms of measurable experimental parameters are as follows:

Lorentzian: $$Y = Y_{\max} \frac{(W/2)^2}{(W/2)^2 + (x - x_0)^2} \quad (2.7)$$

Gaussian: $$Y = Y_{\max} \exp[\frac{-(\ln 2)(x - x_0)^2}{(W/2)^2}] \quad (2.8)$$

where W is the full-width at half-maximum (FWHM) and $Y_{\max}$ is the peak amplitude. The integrated area A under each curve can be calculated as follows:

Lorentzian: $$A = \frac{WY_{\max}}{2}\pi \quad (2.9)$$

Gaussian: $$A = \frac{WY_{\max}}{2}(\frac{\pi}{\ln 2})^{1/2} \quad (2.10)$$

2.3 References

1. H. Rodney Withers, J. M. G. Taylor, and B. Maciejewski, "Treatment volume and tissue tolerance," International Journal of Radiation Oncology*Biology*Physics **14**, 751-759 (1988).

2. J. A. Laissue, H. Blattmann, H. P. Wagner, M. A. Grotzer, and D. N. Slatkin, "Prospects for microbeam radiation therapy of brain tumours in children to reduce neurological sequelae," Developmental Medicine and Child Neurology **49**, 577-581 (2007).

3. P. Regnard, G. Le Duc, E. Brauer-Krisch, I. Tropres, E. A. Siegbahn, A. Kusak, C. Clair, H. Bernard, D. Dallery, J. A. Laissue, and A. Bravin, "Irradiation of intracerebral 9L gliosarcoma by a single array of microplanar x-ray beams from a synchrotron: balance between curing and sparing," Phys Med Biol **53**, 861-878 (2008).

4. A. Bouchet, A. Boumendjel, E. Khalil, R. Serduc, E. Brauer, E. A. Siegbahn, J. A. Laissue, and J. Boutonnat, "Chalcone JAI-51 improves efficacy of synchrotron microbeam radiation therapy of brain tumors," Journal of Synchrotron Radiation **19**, 478-482 (2012).

5. D. N. Slatkin, P. Spanne, F. A. Dilmanian, and M. Sandborg, "Microbeam radiation therapy," Med Phys **19**, 1395-1400 (1992).

6. J. A. Laissue, H. Blattmann, M. Di Michiel, D. N. Slatkin, N. Lyubimova, R. Guzman, W. Zimmermann, S. Birrer, T. Bley, P. Kircher, R. Stettler, R. Fatzer, A. Jaggy, H. M. Smilowitz, E. Brauer, A. Bravin, G. Le Duc, C. Nemoz, M. Renier, W. Thomlinson, J. Stepanek, and H. P. Wagner, "The weanling piglet cerebellum: a surrogate for tolerance to MRT (microbeam radiation therapy) in pediatric neuro-oncology," Penetrating Radiation Systems and Applications Iii **4508**, 65-73 (2001).

7. R. Serduc, T. Christen, J. Laissue, R. Farion, A. Bouchet, B. van der Sanden, C. Segebarth, E. Brauer-Krisch, G. Le Duc, A. Bravin, C. Remy, and E. L. Barbier, "Brain tumor vessel response to synchrotron microbeam radiation therapy: a short-term in vivo study," Physics in Medicine and Biology **53**, 3609-3622 (2008).

8. F. A. Dilmanian, Y. Qu, S. Liu, C. D. Cool, J. Gilbert, J. F. Hainfeld, C. A. Kruse, J. Laterra, D. Lenihan, M. M. Nawrocky, G. Pappas, C. I. Sze, T. Yuasa, N. Zhong, Z. Zhong, and J. W. McDonald, "X-ray microbeams: Tumor therapy and central nervous system research," Nucl Instrum Meth A **548**, 30-37 (2005).

9. J. A. Laissue, G. Geiser, P. O. Spanne, F. A. Dilmanian, J. O. Gebbers, M. Geiser, X. Y. Wu, M. S. Makar, P. L. Micca, M. M. Nawrocky, D. D. Joel, and D. N. Slatkin, "Neuropathology of ablation of rat gliosarcomas and contiguous brain tissues using a microplanar beam of synchrotron-wiggler-generated X rays," Int J Cancer **78**, 654-660 (1998).

10. R. Serduc, P. Verant, J. C. Vial, R. Farion, L. Rocas, C. Remy, T. Fadlallah, E. Brauer, A. Bravin, J. Laissue, H. Blattmann, and B. Van der Sanden, "In vivo two-photon microscopy study of short-term effects of microbeam irradiation on normal mouse brain microvasculature," Int J Radiat Oncol **64**, 1519-1527 (2006).

11. F. A. Dilmanian, Y. Qu, L. E. Feinendegen, L. A. Pena, T. Bacarian, F. A. Henn, J. Kalef-Ezra, S. Liu, Z. Zhong, and J. W. McDonald, "Tissue-sparing effect of x-ray microplanar beams particularly in the CNS: Is a bystander effect involved?," Exp Hematol **35**, 69-77 (2007).

12. J. C. Crosbie, R. L. Anderson, K. Rothkamm, C. M. Restall, L. Cann, S. Ruwanpura, S. Meachem, N. Yagi, I. Svalbe, R. A. Lewis, B. R. G. Williams, and P. A. W. Rogers, "Tumor Cell Response to Synchrotron Microbeam Radiation Therapy Differs Markedly from Cells in Normal Tissues," Int J Radiat Oncol **77**, 886-894 (2010).

13. A. Uyama, T. Kondoh, N. Nariyama, K. Umetani, M. Fukumoto, K. Shinohara, and E. Kohmura, "A narrow microbeam is more effective for tumor growth suppression than a wide microbeam: an in vivo study using implanted human glioma cells," Journal of Synchrotron Radiation **18**, 671-678 (2011).

14. E. A. Siegbahn, J. Stepanek, E. Bräuer-Krisch, and A. Bravin, "Determination of dosimetrical quantities used in microbeam radiation therapy (MRT) with Monte Carlo simulations," Medical Physics **33**, 3248-3259 (2006).

15. M. J. Butson, P. K. N. Yu, T. Cheung, and P. Metcalfe, "Radiochromic film for medical radiation dosimetry," Mat Sci Eng R **41**, 61-120 (2003).

16. W. L. Mclaughlin, C. Yundong, C. G. Soares, A. Miller, G. Vandyk, and D. F. Lewis, "Sensitometry of the Response of a New Radiochromic Film Dosimeter to Gamma-Radiation and Electron-Beams," Nucl Instrum Meth A **302**, 165-176 (1991).

17. S. Devic, "Radiochromic film dosimetry: Past, present, and future," Phys Medica **27**, 122-134 (2011).

18. J. C. Crosbie, I. Svalbe, S. M. Midgley, N. Yagi, P. A. W. Rogers, and R. A. Lewis, "A method of dosimetry for synchrotron microbeam radiation therapy using radiochromic films of different sensitivity," Physics in Medicine and Biology **53**, 6861-6877 (2008).

19. N. Nariyama, T. Ohigashi, K. Umetani, K. Shinohara, H. Tanaka, A. Maruhashi, G. Kashino, A. Kurihara, T. Kondob, M. Fukumoto, and K. Ono, "Spectromicroscopic film dosimetry for high-energy microbeam from synchrotron radiation," Appl Radiat Isotopes **67**, 155-159 (2009).

20. G. Shani, *Radiation Dosimetry Instrumentation and Methods* (CRC Press, 2000).

21. W. L. Mclaughlin, "Esr Dosimetry," Radiat Prot Dosim **47**, 255-262 (1993).

22. K. Mehta, and R. Girzikowsky, "Alanine-ESR dosimetry for radiotherapy IAEA experience," Appl Radiat Isotopes **47**, 1189-1191 (1996).

23. A. Berg, M. Pernkopf, C. Waldhäusl, W. Schmidt, and E. Moser, "High resolution MR based polymer dosimetry versus film densitometry: a systematic study based on the modulation transfer function approach," Physics in Medicine and Biology **49**, 4087 (2004).

24. C. Wong, T. Ackerly, B. Patterson, C. Powell, A. Ho, G. Qiao, D. Solomon, R. Meder, and M. Geso, "Microdosimetry and small field measurements in Polymer Gels," in *World Congress on Medical Physics and Biomedical Engineering 2006*(Springer, 2007), pp. 1883-1886.

25. M. Ptaszkiewicz, E. Braurer-Kirsch, M. Klosowski, L. Czopyk, and P. Olko, "TLD dosimetry for microbeam radiation therapy at the European Synchrotron Radiation Facility," Radiat Meas **43**, 990-993 (2008).

26. P. Olko, Ł. Czopyk, M. Kłosowski, and M. P. R. Waligórski, "Thermoluminescence dosimetry using TL-readers equipped with CCD cameras," Radiat Meas **43**, 864-869 (2008).

27. A. T. A. Rahman, D. A. Bradley, S. J. Doran, B. Thierry, E. Brauer-Krisch, and A. Bravin, "The thermoluminescence response of Ge-doped silica fibres for synchrotron microbeam radiation therapy dosimetry," Nucl Instrum Meth A **619**, 167-170 (2010).

28. G. M. Akselrod, M. S. Akselrod, E. R. Benton, and N. Yasuda, "A novel Al2O3 fluorescent nuclear track detector for heavy charged particles and neutrons," Nucl Instrum Meth B **247**, 295-306 (2006).

29. M. S. Akselrod, and A. E. Akselrod, "New Al2O3 : C,Mg crystals for radiophotoluminescent dosimetry and optical imaging," Radiat Prot Dosim **119**, 218-221 (2006).

30. J. A. Bartz, G. J. Sykora, E. Brauer-Krisch, and M. S. Akselrod, "Imaging and dosimetry of synchrotron microbeam with aluminum oxide fluorescent detectors," Radiat Meas **46**, 1936-1939 (2011).

31. S. Tavernier, A. Gektin, B. Grinyov, and W. Moses, eds. *Radiation detectors for medical applications* (Springer, Dordrecht, 2006).

32. G. Cellere, A. Paccagnella, A. Visconti, M. Bonanomi, S. Beltrami, J. R. Schwank, M. R. Shaneyfelt, and P. Paillet, "Total ionizing dose effects in NOR and NAND flash memories," Ieee T Nucl Sci **54**, 1066-1070 (2007).

33. E. Brauer-Krisch, A. Bravin, M. Lerch, A. Rosenfeld, J. Stepanek, M. Di Michiel, and J. A. Laissue, "MOSFET dosimetry for microbeam radiation therapy at the European Synchrotron Radiation Facility," Medical Physics **30**, 583-589 (2003).

34. E. A. Siegbahn, E. Brauer-Krisch, A. Bravin, H. Nettelbeck, M. L. F. Lerch, and A. B. Rosenfeld, "MOSFET dosimetry with high spatial resolution in intense synchrotron-generated x-ray microbeams," Medical Physics **36**, 1128-1137 (2009).

35. M. Petasecca, A. Cullen, I. Fuduli, A. Espinoza, C. Porumb, C. Stanton, A. H. Aldosari, E. Brauer-Krisch, H. Requardt, A. Bravin, V. Perevertaylo, A. B. Rosenfeld, and M. L. F. Lerch, "X-Tream: a novel dosimetry system for Synchrotron Microbeam Radiation Therapy," J Instrum **7** (2012).

36. M. L. F. Lerch, M. Petasecca, A. Cullen, A. Hamad, H. Requardt, E. Braauer-Krisch, A. Bravin, V. L. Perevertaylo, and A. B. Rosenfeld, "Dosimetry of intensive synchrotron microbeams," Radiat Meas **46**, 1560-1565 (2011).

37. J. Kalliopuska, A. Cullen, M. Lerch, M. Petasecca, M. Santala, and A. Rosenfeld, "Evaluation of a thin microstrip detector for high spatial resolution dosimetry," Radiat Meas **46**, 1643-1645 (2011).

38. S. J. Doran, T. Brochard, J. Adamovics, N. Krstajic, and E. Brauer-Krisch, "An investigation of the potential of optical computed tomography for imaging of synchrotron-generated x-rays at high spatial resolution," Physics in Medicine and Biology **55**, 1531-1547 (2010).

39. S. J. Doran, A. T. A. Rahman, E. Brauer-Krisch, T. Brochard, J. Adamovics, A. Nisbet, and D. Bradley, "Establishing the suitability of quantitative optical CT microscopy of PRESAGER (R) radiochromic dosimeters for the verification of synchrotron microbeam therapy," Physics in Medicine and Biology **58**, 6279-6297 (2013).

40. N. Annabell, N. Yagi, K. Umetani, C. Wong, and M. Geso, "Evaluating the peak-to-valley dose ratio of synchrotron microbeams using PRESAGE fluorescence," Journal of Synchrotron Radiation **19**, 332-339 (2012).

41. T. Ackerly, J. C. Crosbie, A. Fouras, G. J. Sheard, S. Higgins, and R. A. Lewis, "High resolution optical calorimetry for synchrotron microbeam radiation therapy," J Instrum **6** (2011).

42. D. Maki, T. Ishii, F. Sato, Y. Kato, T. Yamamoto, and T. Iida, "Development of Confocal Laser Microscope System for Examination of Microscopic Characteristics of Radiophotoluminescence Glass Dosemeters," Radiat Prot Dosim **144**, 222-225 (2011).

43. H. Ebendorff-Heidepriem, and D. Ehrt, "Optical spectroscopy of rare earth ions in glasses," Glastech Ber-Glass **71**, 289-299 (1998).

44. R. Van Deun, K. Binnemans, C. Gorller-Walrand, and J. L. Adam, "Judd-Ofelt intensity parameters of trivalent lanthanide ions in a NaPO3-BaF2 based fluorophosphate glass," J Alloy Compd **283**, 59-65 (1999).

45. S. D. Jackson, "Towards high-power mid-infrared emission from a fibre laser," Nat Photonics **6**, 423-431 (2012).

46. D. J. Richardson, J. Nilsson, and W. A. Clarkson, "High power fiber lasers: current status and future perspectives," J Opt Soc Am B **27**, B63-B92 (2010).

47. B. J. Ainslie, "A review of the fabrication and properties of erbium-doped fibers for optical amplifiers," Lightwave Technology, Journal of **9**, 220-227 (1991).

48. M. Dejneka, and B. Samson, "Rare-earth-doped fibers for telecommunications applications," Mrs Bull **24**, 39-45 (1999).

49. K. Miura, J. R. Qiu, S. Fujiwara, S. Sakaguchi, and K. Hirao, "Three-dimensional optical memory with rewriteable and ultrahigh density using the valence-state change of samarium ions," Appl Phys Lett **80**, 2263-2265 (2002).

50. K. Binnemans, and C. Gorllerwalrand, "On the Color of the Trivalent Lanthanide Ions," Chem Phys Lett **235**, 163-174 (1995).

51. H. M. Crosswhite, and G. H. Dieke, *Spectra and Energy Levels of Rare Earth Ions in Crystals* (Books on Demand, 1968).

52. W. T. Carnall, G. L. Goodman, K. Rajnak, and R. S. Rana, "A Systematic Analysis of the Spectra of the Lanthanides Doped into Single-Crystal Laf3," Journal of Chemical Physics **90**, 3443-3457 (1989).

53. B. R. Judd, "Optical Absorption Intensities of Rare-Earth Ions," Phys Rev **127**, 750-761 (1962).

54. G. S. Ofelt, "Intensities of Crystal Spectra of Rare-Earth Ions," The Journal of Chemical Physics **37**, 511-520 (1962).

55. B. Di Bartolo, and O. Forte, eds. *Advances in Spectroscopy for Lasers and Sensing* (Springer, 2006).

56. V. Venkatramu, P. Babu, C. K. Jayasankar, T. Troster, W. Sievers, and G. Wortmann, "Optical spectroscopy of Sm3+ ions in phosphate and fluorophosphate glasses," Opt Mater **29**, 1429-1439 (2007).

57. C. X. Qin, Y. L. Huang, W. X. Zhao, L. Shi, and H. J. Seo, "Luminescence spectroscopy and crystallographic sites of Sm2+ doped in Sr6BP5O20," Mater Chem Phys **121**, 286-290 (2010).

58. J. R. Qiu, K. Miura, T. Suzuki, T. Mitsuyu, and K. Hirao, "Permanent photoreduction of Sm3+ to Sm2+ inside a sodium aluminoborate glass by an infrared femtosecond pulsed laser," Appl Phys Lett **74**, 10-12 (1999).

59. N. Ollier, B. Boizot, P. L'henoret, S. Guillous, and G. Petite, "Evidence of transient species occurring in the reduction process of trivalent lanthanides under 2.5 MeV electron irradiation by in situ cathodoluminescence and time-resolved photoluminescence," J Appl Phys **105** (2009).

60. P. R. Biju, G. A. Kumar, G. Jose, and N. V. Unnikrishnan, "Spectroscopic studies of Sm3+-doped phosphate glasses," B Mater Sci **21**, 415-419 (1998).

61. H. W. Song, S. Z. Lu, S. L. E, R. X. Gao, J. H. Zhang, B. J. Chen, H. P. Xia, J. L. Zhang, and Q. H. Ni, "Fluorescence properties of divalent and trivalent europium ions in aluminosilicate glasses," J Appl Phys **91**, 2959-2964 (2002).

62. J. R. Qiu, Y. Shimizugawa, Y. Iwabuchi, and K. Hirao, "Photostimulated luminescence in Eu2+-doped fluoroaluminate glasses," Appl Phys Lett **71**, 759-761 (1997).

63. V. C. Costa, Y. R. Shen, A. M. M. Santos, and K. L. Bray, "Luminescence measurements on SM2+-doped sol-gel glasses," J Non-Cryst Solids **304**, 238-243 (2002).

64. M. Nogami, and Y. Abe, "Enhanced emission from Eu2+ ions in sol-gel derived Al2O3-SiO2 glasses," Appl Phys Lett **69**, 3776-3778 (1996).

65. M. Nogami, G. Kawamura, G. J. Park, H. P. You, and T. Hayakawa, "Effect of Al3+ and Ti4+ ions on the laser reduction of Sm3+ ion in glass," J Lumin **114**, 178-186 (2005).

66. A. Baran, S. Mahlik, M. Grinberg, and E. Zych, "High pressure and time-resolved luminescence spectra of Ca3Y2(SiO4)(3) doped with Eu2+ and Eu3+," J Phys-Condens Mat **25** (2013).

67. A. Edgar, C. R. Varoy, C. Koughia, G. Okada, G. Belev, and S. Kasap, "High-resolution X-ray imaging with samarium-doped fluoroaluminate and fluorophosphate glass," J Non-Cryst Solids **377**, 124-128 (2013).

68. Y. Huang, C. Jiang, K. Jang, H. S. Lee, E. Cho, M. Jayasimhadri, and S.-S. Yi, "Luminescence and microstructure of Sm2+ ions reduced by x-ray irradiation in Li2O–SrO–B2O3 glass," J Appl Phys **103**, - (2008).

69. G. Okada, B. Morrell, C. Koughia, A. Edgar, C. Varoy, G. Belev, T. Wysokinski, D. Chapman, and S. Kasap, "Spatially resolved measurement of high doses in microbeam radiation therapy using samarium doped fluorophosphate glasses," Appl Phys Lett **99** (2011).

70. L. Y. Yang, N. Da, D. P. Chen, Q. Z. Zhao, X. W. Jiang, C. S. Zhu, and J. R. Qiu, "Valence state change and refractive index change induced by femtosecond laser irradiation in Sm3+ doped fluoroaluminate glass," J Non-Cryst Solids **354**, 1353-1356 (2008).

71. Y. D. Li, J. Y. Wang, Y. L. Huang, and H. J. Seo, "Temperature-Dependent 5D(0)-> 7F(0) Luminescence of Sm2+Ions Doped in Alkaline Earth Borophosphate Glass," J Am Ceram Soc **93**, 722-726 (2010).

72. K. Fujita, C. Yasumoto, and K. Hirao, "Photochemical reactions of samarium ions in sodium borate glasses irradiated with near-infrared femtosecond laser pulses," J Lumin **98**, 317-323 (2002).

73. Y. D. Li, K. Jang, Y. L. Huang, and C. F. Jiang, "The dependence of luminescence on reduction of Sm(2+) ions doped in lithium barium borate glasses," Appl Phys a-Mater **97**, 663-669 (2009).

74. B. H. Babu, and V. V. R. K. Kumar, "Fluorescence properties and electron paramagnetic resonance studies of gamma-irradiated Sm3+-doped oxyfluoroborate glasses," J Appl Phys **112** (2012).

75. E. Malchukova, B. Boizot, D. Ghaleb, and G. Petite, "Optical properties of pristine and gamma-irradiated Sm doped borosilicate glasses," Nucl Instrum Meth A **537**, 411-414 (2005).

76. E. Malchukova, B. Boizot, G. Petite, and D. Ghaleb, "Optical properties and valence state of Sm ions in aluminoborosilicate glass under beta-irradiation," J Non-Cryst Solids **353**, 2397-2402 (2007).

77. M. Nogami, and K. Suzuki, "Formation of Sm2+ ions and spectral hole burning in X-ray irradiated glasses," Journal of Physical Chemistry B **106**, 5395-5399 (2002).

78. J. R. Qiu, K. Kojima, K. Miura, T. Mitsuyu, and K. Hirao, "Infrared femtosecond laser pulse-induced permanent reduction of Eu3+ to Eu2+ in a fluorozirconate glass," Optics Letters **24**, 786-788 (1999).

79. e. a. G. Belev, "Valency conversion of samarium ions under high dose synchrotron generated X-ray radiation," physica status solidi (c) **8**, 2822–2825 (2011).

80. K. Jang, Y. D. Li, Y. L. Huang, and C. F. Jiang, "The dependence of luminescence on reduction of Sm(2+) ions doped in lithium barium borate glasses," Appl Phys a-Mater **97**, 663-669 (2009).

81. H. J. Seo, Y. D. Li, J. Y. Wang, and Y. L. Huang, "Temperature-Dependent 5D(0)-> 7F(0) Luminescence of Sm2+Ions Doped in Alkaline Earth Borophosphate Glass," J Am Ceram Soc **93**, 722-726 (2010).

82. H. Ebendorff-Heidepriem, and D. Ehrt, "Effect of europium ions on X-ray-induced defect formation in phosphate containing glasses," Opt Mater **19**, 351-363 (2002).

83. J. S. Stroud, "Color-Center Kinetics in Cerium-Containing Glass," Journal of Chemical Physics **43**, 2442-2450 (1965).

84. D. Ehrt, P. Ebeling, and U. Natura, "UV Transmission and radiation-induced defects in phosphate and fluoride-phosphate glasses," J Non-Cryst Solids **263**, 240-250 (2000).

85. K. Przibram, ed. *Irradiation Colours and Luminescence* (Pergamon Press, Ltd., London, 1956).

86. J. H. S. a. W. D. Compton, ed. *Color Centers in Solids* (Pergamon Press, New York, 1962).

87. D. Ehrt, and W. Vogel, "Radiation Effects in Glasses," Nucl Instrum Meth B **65**, 1-8 (1992).

88. C. A. A. J. Wong, ed. *Glass: Structure by Spectroscopy* (Marcel Dekker Inc, New York, 1976).

89. G. Lancaster, "Electron paramagnetic resonance (a review)," J Mater Sci **2**, 489-495 (1967).

90. D. L. Griscom, "Esr Studies of Radiation-Damage and Structure in Oxide Glasses Not Containing Transition Group Ions - a Contemporary Overview with Illustrations from Alkali Borate System," J Non-Cryst Solids **13**, 251-285 (1974).

91. T. V. Bocharova, G. O. Karapetyan, A. M. Mironov, N. O. Tagil'tseva, and V. D. Khalilev, "Specific features of the induced absorption spectra of fluoroaluminate glasses doped with samarium ions," Glass Phys Chem+ **29**, 7-10 (2003).

92. A. Edgar, C. R. Varoy, C. Koughia, D. Tonchev, G. Belev, G. Okada, S. O. Kasap, H. von Seggern, and M. Ryan, "Optical properties of divalent samarium-doped fluorochlorozirconate glasses and glass ceramics," Opt Mater **32**, 266-266 (2009).

93. P. Ebeling, D. Ehrt, and M. Friedrich, "X-ray induced effects in phosphate glasses," Opt Mater **20**, 101-111 (2002).

94. L. B. Fletcher, J. J. Witcher, N. Troy, S. T. Reis, R. K. Brow, R. M. Vazquez, R. Osellame, and D. M. Krol, "Femtosecond laser writing of waveguides in zinc phosphate glasses [Invited]," Opt Mater Express **1**, 845-855 (2011).

95. G. Origlio, F. Messina, S. Girard, M. Cannas, A. Boukenter, and Y. Ouerdane, "Spectroscopic studies of the origin of radiation-induced degradation in phosphorus-doped optical fibers and preforms," J Appl Phys **108** (2010).

96. H. Ebendorff-Heidepriem, and D. Ehrt, "Effect of Tb3+ ions on X-ray-induced defect formation in phosphate containing glasses," Opt Mater **18**, 419-430 (2002).

97. B. Boizot, G. Petite, D. Ghaleb, and G. Calas, "Radiation induced paramagnetic centres in nuclear glasses by EPR spectroscopy," Nucl Instrum Meth B **141**, 580-584 (1998).

98. S. Rydberg, and M. Engholm, "Experimental evidence for the formation of divalent ytterbium in the photodarkening process of Yb-doped fiber lasers," Opt. Express **21**, 6681-6688 (2013).

99. H. Gebavi, S. Taccheo, D. Tregoat, A. Monteville, and T. Robin, "Photobleaching of photodarkening in ytterbium doped aluminosilicate fibers with 633 nm irradiation," Opt Mater Express **2**, 1286-1291 (2012).

100. D. L. Griscom, "Optical Absorption of Cl2− Hole-Type Centers in Irradiated Alkali Halide–Alkali Borate Glasses," The Journal of Chemical Physics **51**, 5186-5187 (1969).

101. D. L. Griscom, P. C. Taylor, and P. J. Bray, "Paramagnetic Resonance of Room-Temperature-Stable V-Type Centers in γ-Irradidated Alkali Halide–Boron Oxide Glasses," The Journal of Chemical Physics **50**, 977-983 (1969).

102. D. L. Griscom, E. J. Friebele, K. J. Long, and J. W. Fleming, "Fundamental Defect Centers in Glass - Electron-Spin Resonance and Optical-Absorption Studies of Irradiated Phosphorus-Doped Silica Glass and Optical Fibers," J Appl Phys **54**, 3743-3762 (1983).

103. P. Zeeman, "The Effect of Magnetisation on the Nature of Light Emitted by a Substance," Nature **55**, 347-347 (1897).

104. B. Odom, D. Hanneke, B. D'Urso, and G. Gabrielse, "New Measurement of the Electron Magnetic Moment Using a One-Electron Quantum Cyclotron," Physical Review Letters **97**, 030801 (2006).

105. J. B. John Wertz, *Electron Spin Resonance: Elementary Theory and Practical Applications* (McGrow-Hill, Inc., 1972).

106. P. H. Reiger, *Electron Spin Resonance: Analysis and Interpretation* (RSC Publishing, Providence, 2007).

107. C. P. Poole, *Electron Spin Resonance: A Comprehensive Treatise on Experimental Techniques* (John Wiley & Sons, Inc., Mineola, New York, 1983).

108. J. W. ORTON, *Electron Paramagnetie Resonance* (Iliffe, London, 1968).

109. M. Jonas, "Concepts and methods of ESR dating," Radiat Meas **27**, 943-973 (1997).

110. J. B. John Weil, *Electron Paramagnetic Resonance: Elementary Theory and Practical Applications* (John Wiley & Sons, Inc., Hoboken, New Jersey, 2007).

3 X-ray Induced Sm^{3+} to Sm^{2+} Conversion in Fluorophosphate and Fluoroaluminate Glasses for the Monitoring of High-doses in Microbeam Radiation Therapy

Published as:

Shahrzad Vahedi, Go Okada, Brian Morrell, Edward Muzar, Cyril Koughia, Andy Edgar, Chris Varoy, George Belev, Tomasz Wysokinski, Dean Chapman and Safa Kasap, "X-ray induced Sm^{3+} to Sm^{2+} conversion in fluorophosphate and fluoroaluminate glasses for the monitoring of high-doses in microbeam radiation therapy", *Journal of Applied Physics*, 112, 073108, October 2012.

Author contributions:

The main experimental work and data analysis of this manuscript was performed by Shahrzad Vahedi. Go Okada, Brian Morrell and Edward Muzar performed experiments represented in Figure 3.5, Figure 3.4(a), and Figure 3.7(d), respectively. Go Okada also helped in conducting the experiments demonstrated in Figure 3.10. Shahrzad Vahedi, Cyril Koughia and Safa Kasap contributed to the preparation of the manuscript. Andy Edgar and Chris Varoy synthesized the glasses used in this manuscript. George Belev and Tomasz Wysokinski provided technical support for experiments which were performed at the Canadian Light Source. Andy Edgar and Dean Chapman helped to improve the manuscript by comments and suggestions.

Note: The dose values in this manuscript represent dose in air on the surface of the sample, and not inside the sample. Dose calculation method is discussed in the appendix. An estimation of the dose absorbed by the sample is also provided in the appendix.

3.1 Abstract

Fluorophosphate and fluoroaluminate glasses doped with trivalent samarium were evaluated as sensors of X-ray radiation for microbeam radiation therapy at the Canadian Light Source using the conversion of trivalent Sm^{3+} to the divalent form Sm^{2+}. Both types of glasses show similar conversion rates and may be used as a linear sensor up to ~150 Gy and as a nonlinear sensor up to ~2400 Gy, where saturation is reached. Experiments with a multi-slit collimator show high spatial resolution of the conversion pattern; the pattern was acquired by a confocal fluorescence microscopy technique. The effects of previous X-ray exposure may be erased by annealing at temperatures exceeding the glass transition temperature T_g while annealing at $T_A < T_g$ enhances the Sm conversion. This enhancement is explained by a thermally stimulated relaxation of host glass ionic matrix surrounding X-ray induced Sm^{2+} ions. In addition, some of the Sm^{3+}-doped glasses were codoped with Eu^{2+}-ions but the results show that there is no marked improvement in the conversion efficiency by the introduction of Eu^{2+}.

3.2 Introduction

Microbeam radiation therapy (MRT) is an experimental form of radiation treatment which has the potential to improve the treatment of many types of cancer compared to customary broad-beam radiation treatment [1-2]. It is based on the markedly different response of tumor and normal cells to this form of treatment [3]. Namely, the central nervous system of vertebrates displays extraordinary resistance to damage by microscopically narrow, multiple, parallel, planar beams of X-rays. Therefore, "imminently lethal gliosarcomas in the brains of mature rats can be inhibited and ablated by such microbeams with little or no harm to mature brain tissues and neurological function [4]." In practice, the radiation is applied in the form of a grid by passing

the highly collimated X-ray beam from a synchrotron through a microplane collimator which is a stack of parallel plates of two materials with dramatically different X-ray transparencies [5-6].

The accurate, simultaneous recording of peak and valley doses that differ by hundreds of Grays, and the large dose gradients (hundreds of Grays over several microns) in the whole X-ray energy range of interest for MRT (50–250 keV) is an extremely challenging task. No current detector can satisfactorily meet all these requirements and intensive research towards the development of detectors suitable for MRT is currently underway. Detectors such as ionization chambers, alanine dosimeters, MOSFET detectors, Gafchromic® films, radiochromic polymers, thermoluminescence detectors (TLDs), polymer gels, fluorescent nuclear track detectors, optically stimulated luminescence detectors, and floating gate-based dosimeters have been reviewed with respect to their potential applications in MRT [7].

The latest attempts to solve the problem are based on using high resolution optical calorimetry [8], confocal laser microscopy of the radiophotoluminescence of silver activated phosphate glass [9], thermoluminescence of Ge-doped silica fibers [10], and spectromicroscopic film dosimetry [11]. Another novel approach for MRT dosimetry is the effect of valence conversion of rare earth ions embedded in a suitable host material as discussed by the present group [12]. Various papers have demonstrated the possibility of valence conversion of different ions in a variety of host materials under different forms of excitation such as X-rays, γ- and β-irradiation as well as near infra red (NIR) optical excitation [13-18]. Among the rare earth ions, Sm^{3+} to Sm^{2+} conversion is of particular interest because the dominant emission bands of Sm^{3+} and Sm^{2+} ions are very easy to distinguish, all dominant bands are situated in the red region of the spectrum, and so there is a good match to silicon based detectors used in optical measurements. It should be stressed that it

was recently demonstrated that $Sm^{3+} \rightarrow Sm^{2+}$ conversion may provide submicron spatial resolution with respect to optical storage of information [14-15].

Earlier, we showed the applicability of Sm-doped fluorophosphate (FP) glasses as a potential dosimeter material to measure both the dose and the peak-to-valley dose ratio (PVDR), a critical parameter for successful MRT therapy. We demonstrated the efficiency of $Sm^{3+} \rightarrow Sm^{2+}$ conversion in these glasses and illustrated the feasibility of a spatially resolving dosimetric sensor based on the confocal detection of photoluminescence (PL) [19].

In the present paper, we discuss $Sm^{3+} \rightarrow Sm^{2+}$ conversion in fluoroaluminate (FA) glasses and compare it with FP glasses, showing the advantages of FA glasses as a Sm-ion host. We also discuss $Sm^{2+} \rightarrow Sm^{3+}$ re-conversion by means of thermal annealing at temperatures above the glass transition temperature (T_g). Finally, we discuss the phenomenon of "thermally stimulated enhancement" of $Sm^{3+} \rightarrow Sm^{2+}$ conversion at annealing temperatures below T_g and discuss the possible origins of this phenomenon.

3.3 Experimental

FP glasses can be thought of as a combination of fluoride and phosphate glasses with a variety of possible cationic species. The composition and preparation are based on the FP10 composition published by Ebendorff-Heidepriem and Ehrt [20]. The FP10 batch composition is given in mol. % as $10.0Sr(PO_3)_2$-$34.4AlF_3$-$10MgF_2$-$30.4CaF_2$-$15.2SrF_2$. The FP10 glasses were prepared with the concentration of Sm^{3+} varying from 0.001 to 0.2 mol.%. The FA glass batch composition is given in mol. % as $10MgF_2$-$35AlF_3$-$20CaF_2$-$10SrF_2$-$(15 - x)YF_3$-$10BaF_2$-$xSmF_3$. The concentration of Sm^{3+} in all investigated FA glasses was chosen to be 0.5 mol. %. Some glasses were codoped with Eu^{2+} by adding EuF_2 into the initial melt.

The X-ray irradiation was performed by two different methods. The first one used synchrotron radiation at the Biomedical Imaging and Therapy 05B1-1 bend magnet beamline, Canadian Light Source, Saskatoon, Canada. The spectrum of filtered X-ray radiation had a maximum around 50 keV [19]. The intensity of synchrotron X-ray irradiation corresponded to an approximate dose rate of 110 Gy/min. This is the maximum value and the exact dose may vary within 20% depending on the exact position of the sample inside of the X-ray beam. The second method used the emission produced by a FAXITRON X-ray cabinet with a tungsten anode operating at 110 kVp with an approximate dose rate of 50 Gy/min. The quoted dose values represent dose in air on the surface of the sample, and not inside the sample. The glasses were cut and polished flat for X-ray and optical measurements.

The steady-state PL spectra were measured from 200 nm to either 1100 nm or 1200 nm, using either a Stellar Net EPP2000 fiber input mini-spectrometer (up to 1100 nm) with spectral resolution around 4 nm or an ASEQ fiber input mini-spectrometer (up to 1200 nm) with spectral resolution better than 1 nm. The excitation source for all the photoluminescence spectra was a laser diode with an emission wavelength at 405 nm corresponding to absorption bands of Sm^{3+} and Sm^{2+} ions. The intensity of excitation was kept as low as possible to minimize the effect of $Sm^{2+} \rightarrow Sm^{3+}$ reconversion during the measurements. The transmittance spectra were measured using a Perkin-Elmer Lambda 900 spectrophotometer.

Experiments were also conducted on a temperature-modulated differential scanning calorimeter (TMDSC) in order to obtain the temperature dependence of heat capacity $C_p(T)$ and hence the glass transition temperature (T_g). The TMDSC experiments were performed as described previously on DSC Q100 and 2910 thermal analysis systems (TA Instruments), but

using an underlying heating rate of 2 °C/min and modulation amplitude of ±1 °C and a modulation period of 60 s [21].

3.4 Results and Discussion

The reduction of Sm from trivalent form to divalent form may be achieved in a straightforward way by simple chemical means [22-23]. However, numerous experiments have demonstrated that the interaction of electromagnetic radiation with various glasses results in a variety of effects including changes in the valency of ions and the formation of color centers [13-20], [24-34].

In our particular case, the desirable outcome would be simply the reduction of Sm^{3+} to Sm^{2+}. This effect may be characterized and quantified by analyzing the emission spectra of Sm^{3+} and Sm^{2+} ions, which are known to be very different. An example of emission spectra and their transformation under X-ray irradiation in Sm^{3+} doped FP and FA glasses is shown in Figure 3.1 . Generally, the response to X-ray induced reduction of Sm^{3+} may be effectively characterized by the conversion ratio $R(t) = PL(Sm^{2+})/PL(Sm^{3+})$. However, an irradiation "side-effect" is the creation of different color centers associated with electrons and holes captured in the host glass [28-29]. Figure 3.1 compares the emission spectra of Sm^{3+} and Sm^{2+} ions with the spectra of X-ray induced changes in optical transmittance of FA and FP glasses. Figure 3.1(a) clearly shows that X-ray induced optical transmittance substantially blocks Sm^{3+} and Sm^{2+} emission in FP glasses. In extreme cases of long irradiation times (i.e., large doses), the FP glasses may become so dark that PL measurements become problematic. In contrast, Figure 3.1(b) shows that in FA glasses, the changes in absorbance are mostly induced in the UV region, which causes only a small reduction in the observed Sm^{3+} and Sm^{2+} emission. From a technical point of view, this is a great advantage of FA glasses. Nevertheless, FP glasses are more thoroughly investigated and

their properties are much better understood, which therefore make them particularly interesting for scientific research. The transparency of FA glasses in the spectral region of Sm^{3+} and Sm^{2+} emission significantly simplifies the detection of the $Sm^{3+} \rightarrow Sm^{2+}$ conversion inasmuch as it may be simply measured as a response ratio R (Sm^{2+}/Sm^{3+}) of the PL intensities of two bands: $^5D_0 \rightarrow {}^7F_0$ at around 683 nm for Sm^{2+}, and $^4G_{5/2} \rightarrow {}^6H_{5/2}$ at around 600 nm for Sm^{3+}. However, Figure 3.1(a) shows that in the FP glass, the X-ray induced changes in absorption develop throughout the UV to visible region, substantially overlapping the Sm^{3+} and Sm^{2+} emission, distorting the PL spectra and reducing their intensity.

Figure 3.2 demonstrates the evolution of transmittance and induced absorbance as a result of X-ray synchrotron irradiation in FP and FA glasses. To interpret the data, it is quite common to invoke a so-called "band separation," i.e., to present the induced absorbance as a sum of Gaussians which are assigned to different electron and hole centers [29, 35]. In FP glasses, X-ray induced absorbance may be effectively simulated using 4 Gaussians as shown in Figure 3.2(f). The bands in the visible region (G1-G3) are usually associated with so-called phosphorous oxide

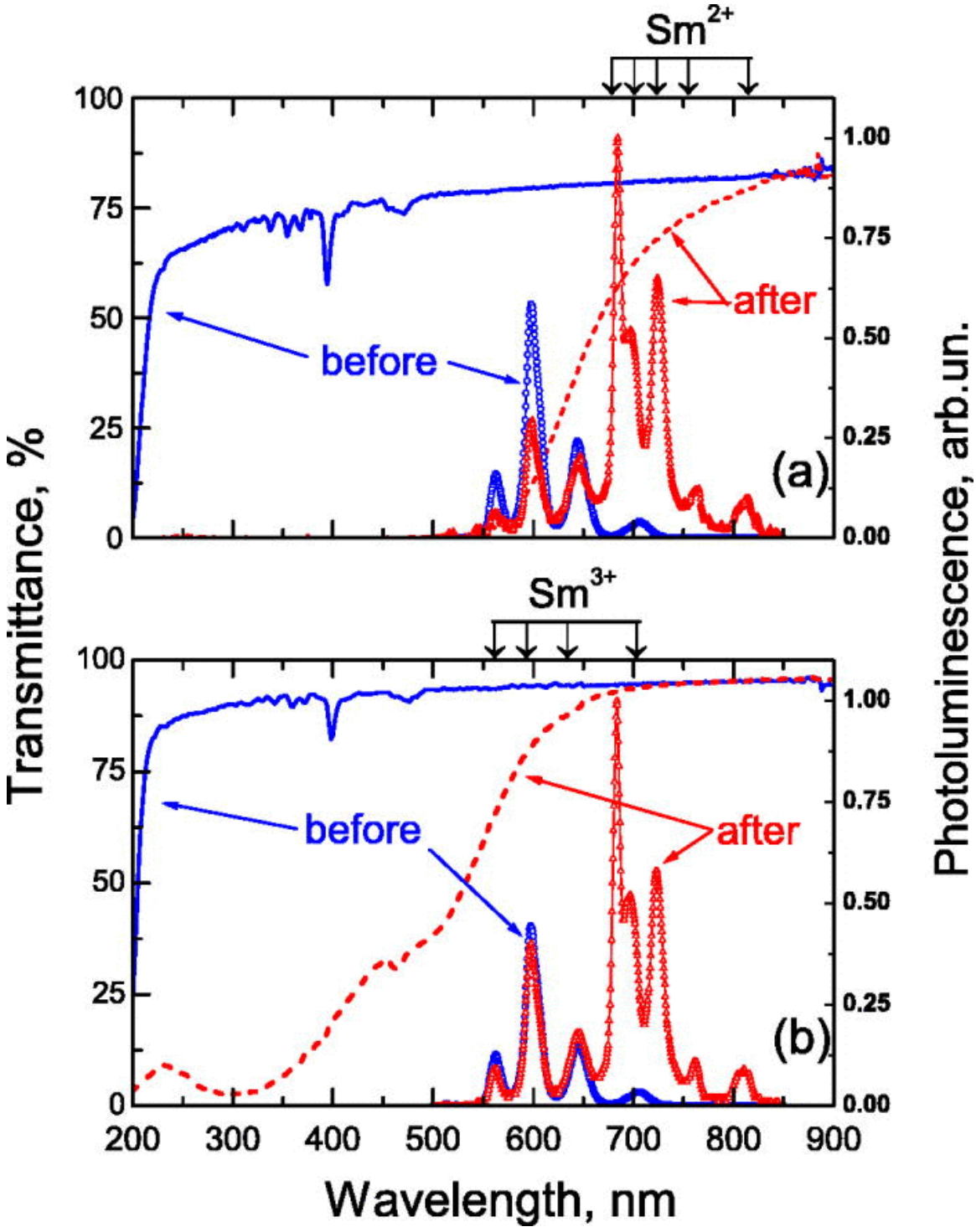

Figure 3.1 The spectra of optical transmittance and photoluminescence of Sm^{3+} and Sm^{2+} ions in (a) fluorophosphate and (b) fluoroaluminate glasses before (as-prepared) and after synchrotron X-ray irradiation for 2000 s corresponding to a total dose of ~3000 Gy.

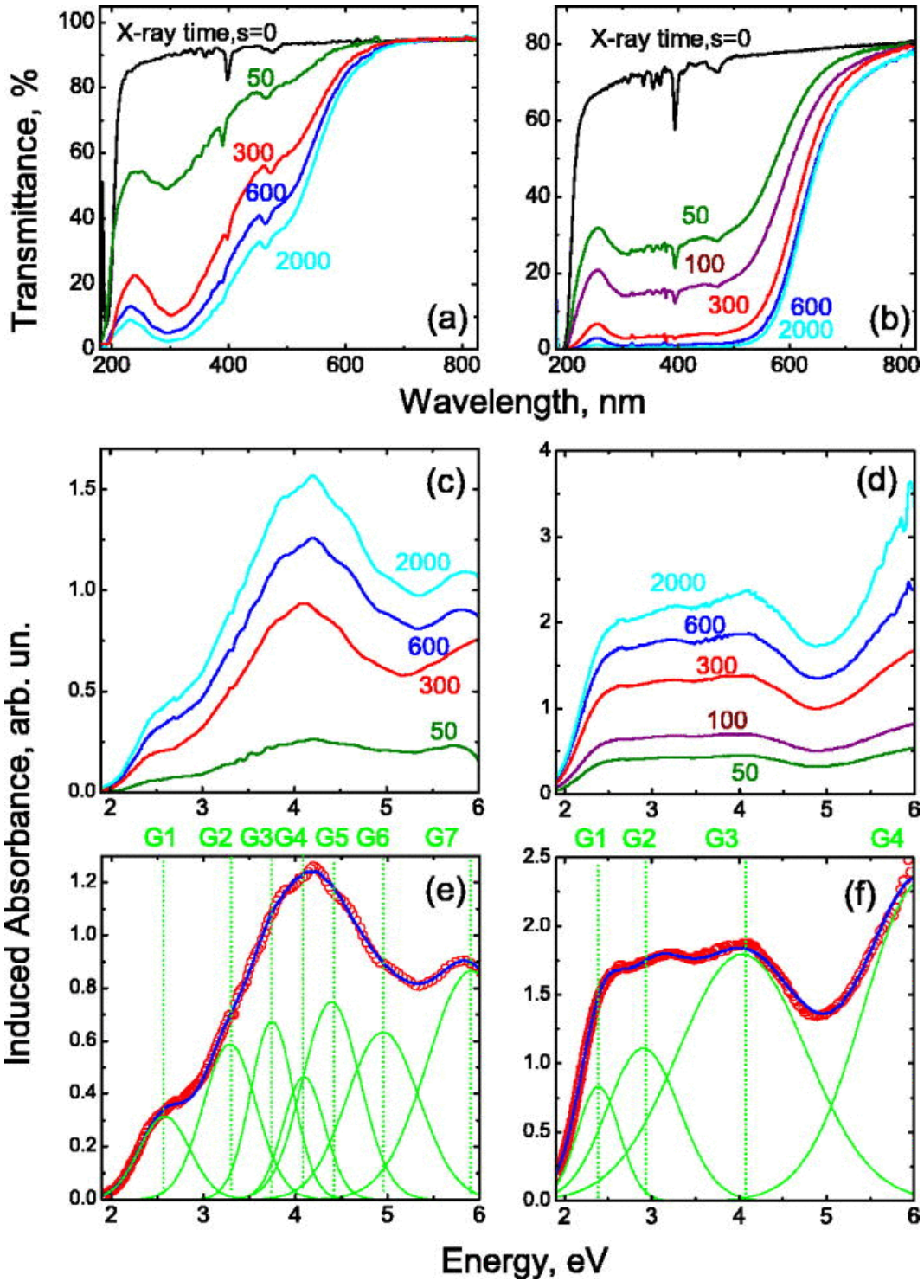

Figure 3.2 The evolution of transmittance (a) and (b) and induced absorbance (c) and (d) as a result of X-ray synchrotron irradiation in FA (a) and (c), and FP (b) and (d) glasses. (e) and (f) present a possible band separation of optical absorbance induced by 600 s of X-ray irradiation in FA and FP glasses, respectively, as sums of Gaussians marked G1-G7 and G1-G4 at their centers. The irradiation was carried out at the Canadian Light Source.

hole centers (POHC), while the UV band G4 is related to an electron center [27]. In FA glasses, the picture is more complicated and effective band separation requires a minimum of seven Gaussians shown in Figure 3.2(e) as G1-G7. They are commonly associated with fluorine complexes and oxygen contamination [24, 26, 36-37].

In the situation when Sm^{3+} and Sm^{2+} emission is partially blocked by induced absorbance as shown in Figure 3.1(a) , for FP glasses, the response ratio $R(t) = PL(Sm^{2+})/PL(Sm^{3+})$ may be measured and calculated in different ways. The first method was used in our previous paper [19]. In the latter, the response ratio was calculated as $R(t) = \int_{676}^{713} PL(Sm^{2+})d\lambda / \int_{676}^{713} PL(Sm^{3+})d\lambda$, i.e., by integration over spectral interval where the induced absorbance is small and hence its influence is minimized. However, there is another approach which gives more reliable results while producing some additional information as illustrated by Figure 3.3(a) and Figure 3.3(b). It seems appropriate here to note that the PL spectra overlap primarily with the band G1 while the influence of all other bands (G2-G4) is much less important. Figure 3.3(b) presents the normalized emission spectra of Sm^{3+} and Sm^{2+} ions and normalized Gaussian G1 centered at 2.37 eV, i.e., 524 nm. The emission spectrum may be approximated by

$$PL(\lambda)=[a_1\Phi_1(\lambda)+a_2\Phi_2(\lambda)]\exp[-a_3 POHC(\lambda)] \qquad (3.1)$$

where $\Phi_1(\lambda)$ and $\Phi_2(\lambda)$ are normalized emission spectra of Sm^{3+} and Sm^{2+}, respectively, $POHC(\lambda)$ is the normalized Gaussian G1 while a_1 to a_3 are adjustable parameters. The spectra $\Phi_1(\lambda)$ and $\Phi_2(\lambda)$ were measured independently on specially prepared samples containing Sm^{3+} and Sm^{2+} ions only. The quality of approximation is illustrated by Figure 3.3(a). Using this approach, the response $R(t) = PL(Sm^{2+})/PL(Sm^{3+})$ turns out to be equal to the ratio a_2/a_1 while a_3 turns out to be proportional to the induced absorbance.

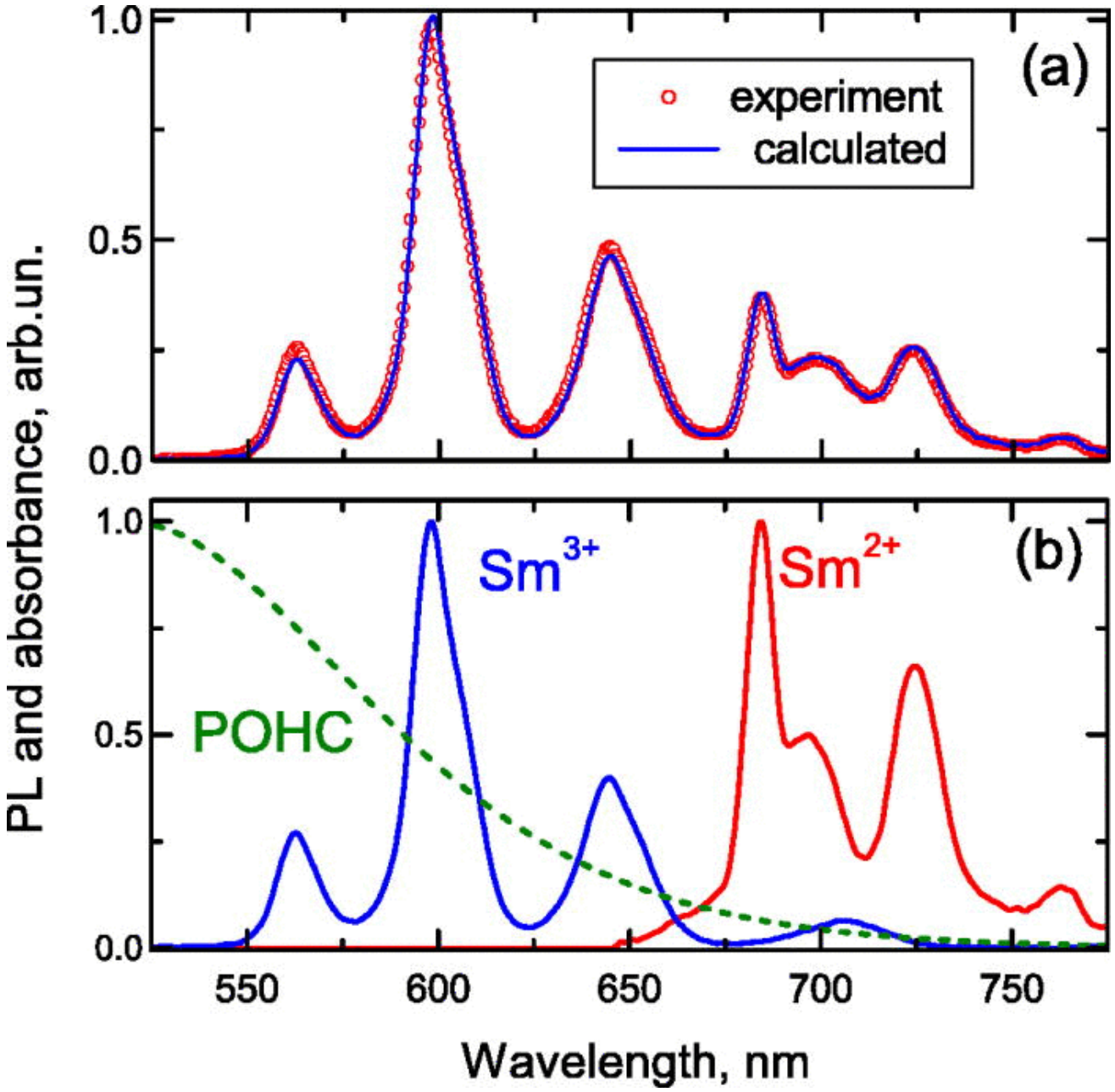

Figure 3.3 (a) Comparison of experimentally measured (symbols) and calculated (solid curves) PL spectra of Sm–doped FP10 glass after synchrotron X-ray dose ~1500 Gy. (b) The emission spectra of Sm^{3+} and Sm^{2+} ions (solid lines) and induced absorbance due to POHC (broken line) used in model calculations. The irradiation was carried out at the Canadian Light Source.

Figure 3.4 shows the response $R(t)$ in FP and FA glasses as a function of irradiation time and hence the dose over a very large range from about 0.1 Gy to 10000 Gy. As pointed out

previously, this is the advantage of the Sm^{3+}-doped glasses. The results for FP shown in Figure 3.4(a) were published and discussed in detail earlier [19]. Briefly, Figure 3.4(a) shows that for a large variety of Sm-concentrations below 0.2%, the irradiation time dependence of $R(t)$ may be universally approximated by $R(t)=R_0[1-\exp(-t/\tau)]$, with $\tau \approx 270$ s, where the parameters R_0 and τ did not exhibit strong dependence on the concentration of Sm. These results demonstrate that the present material, as it is, may be used as a quasi-linear dose recording sensor over a wide dynamic range covering about three orders of magnitude up to ~150 Gy and as a non-linear sensor up to ~2400 Gy whereupon saturation is reached.

Figure 3.4(b) shows the response $R(t) = PL(Sm^{2+})/PL(Sm^{3+})$ for FA glasses with 0.5% of Sm^{3+} and varying amounts of codoping with Eu^{2+}, and the intensity of X-ray induced Gaussian absorbance bands (G1-G7) vs. irradiation time/dose. It is worth noting that the efficiency of $Sm^{3+} \rightarrow Sm^{2+}$ conversion in FA glasses is similar to that in FP glasses. The combination of good conversion ratio, and the induced absorbance being in the UV make fluoroaluminate glasses a particularly appealing rare-earth doped material for applications in MRT dosimetry. Second, Sm^{3+}-FA glasses codoped with 0.2 mol. % Eu^{2+} essentially showed the same behavior as those FA glasses doped with Sm^{3+} only. However, higher amounts of codoping with 0.5–1 mol. % Eu^{2+} leads to a reduction in the conversion ratio R. The rationale for codoping with Eu^{2+} is discussed below and is related to the goal of accelerating the conversion of Sm^{3+} to Sm^{2+}. All data refer to as-prepared, unannealed samples except closed inverted triangles (▼) that refer to the sample which had previously received a dose of ~3000 Gy and then was annealed at 490 °C for 30 min before being reirradiated. Figure 3.4 shows also that there is remarkable correlation

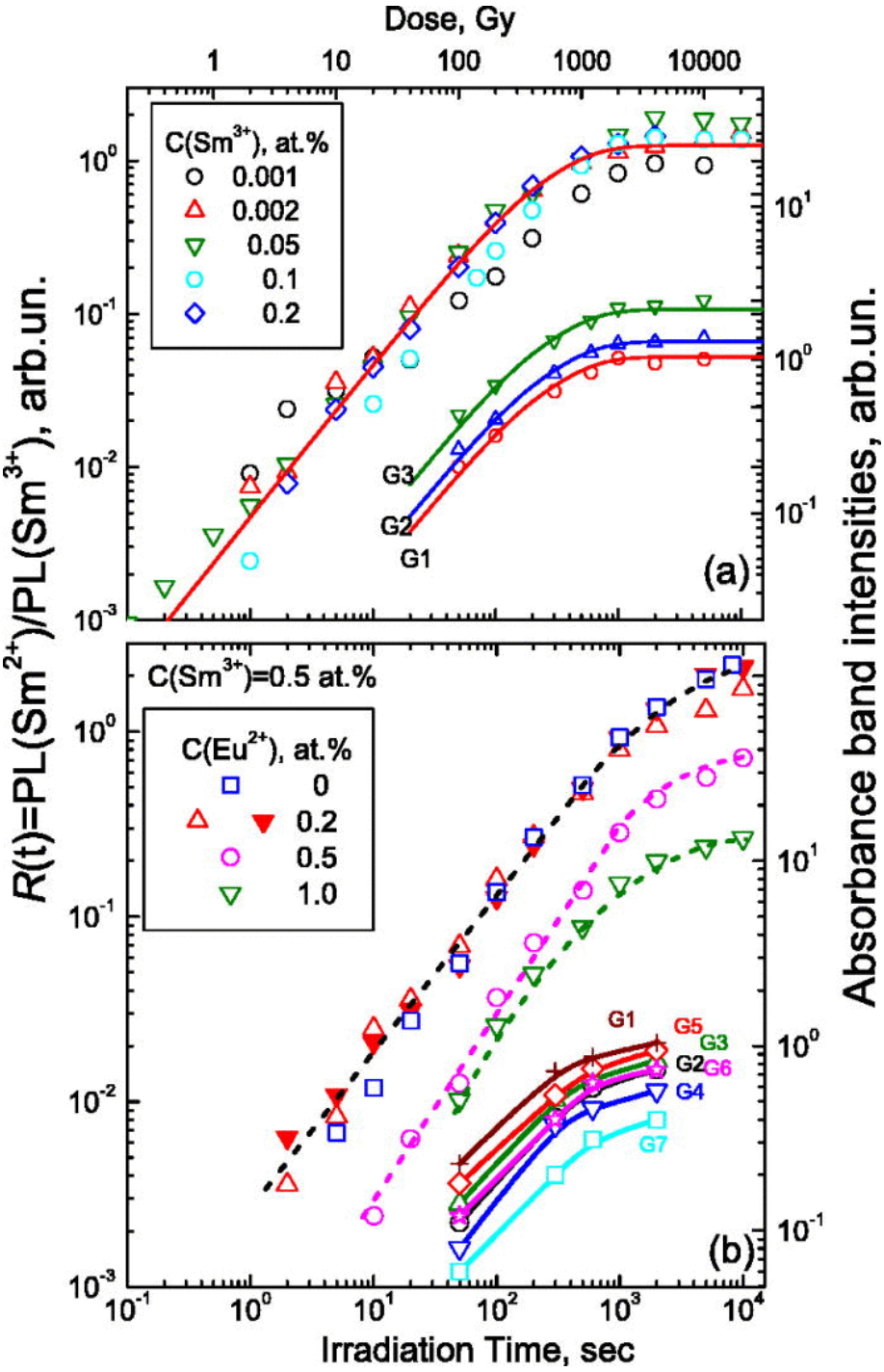

Figure 3.4 The ratio $R(t) = \mathrm{PL}(\mathrm{Sm}^{2+})/\mathrm{PL}(\mathrm{Sm}^{3+})$ for FP (a) and FA(b) glasses doped with varying amounts of Sm^{3+} and codoped with Eu^{2+}, and the intensity of X-ray induced Gaussian absorbance bands (G1-G3 and G1-G7) vs. irradiation time/dose. The lines in (a) are based on an exponential build-up in the dose response with $\tau \approx 270$ s and varying values of R_0. All data refer to as-deposited unannealed samples except for one, closed inverted triangles (▼) that refers to the sample which had received a dose of ~3000 Gy and then was annealed at 490 °C for 30 minutes. The irradiation was carried out at the Canadian Light Source.

between $R(t)$ and the amplitudes of induced absorption bands G1-G3 in Figure 3.4(a) and G1-G7 in Figure 3.4(b) .

Figure 3.5 represents the dose distributions in a Sm doped FA glass sample irradiated through an 8 mm thick Tungsten/Air microslit collimator (MSC) manufactured by Usinage et Nouvelles Technologies, Morbier, France. The microbeams are 50 μm wide and have centre-to-centre distance of 400 μm. The simplified construction of the MSC may be found elsewhere [19]. The dose profile was extracted from the $Sm^{3+} \rightarrow Sm^{2+}$ conversion pattern in two steps. First, both the Sm ions (Sm^{3+} and Sm^{2+}) were individually detected as fluorescence signals using a confocal fluoroscopic microscope, and the response was then computed as $R = PL(Sm^{2+})/PL(Sm^{3+})$, where $PL(Sm^{2+})$ and $PL(Sm^{3+})$ are fluorescence signals from Sm^{2+} and Sm^{3+}, respectively. Next, the response values were recalculated into the corresponding dose values using a dose calibration curve, which was measured separately. Figure 3.5 clearly shows that this method allows the recording of microbeams with a spatial resolution in the micrometer range and peak-to-valley ratios equal to 50–100.

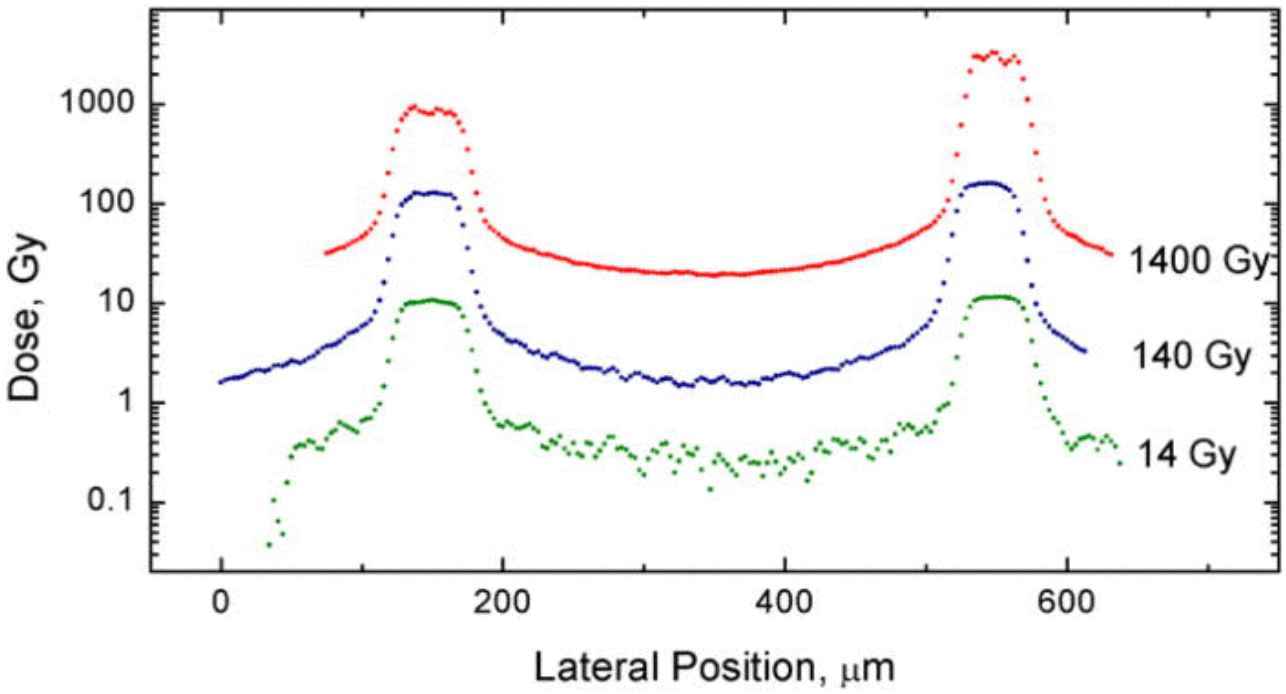

Figure 3.5 Dose profiles of microbeams used in MRT for three different X-ray exposure times. The dose information was recorded on Sm-doped FA glasses in a form of $Sm^{3+} \rightarrow Sm^{2+}$ conversion and readout using confocal fluorescence microscopy. The microbeams were 50 μm wide and had centre-to-centre separation (periodicity) of 400 μm.

The above experimental data as well as those published earlier [19] show that Sm doped FP and FA glasses may be used for effective X-ray detection with spatial resolution on the micrometer scale with a range up to 2400 Gy. However, the question of erasability and reproducibility of the X-ray pattern still needs to be addressed. Figure 3.4(b) and Figure 3.6(a) partially answer this question for FA and FP glasses, respectively. They show that the effect of X-ray irradiation may be completely erased by appropriate annealing at an elevated temperature (T_A) exceeding the glass transition temperature (T_g) which is equal to 440 °C for FA glass and 462 °C for FP glass. The subsequent irradiation leads to the close reproduction of $R(t) = PL(Sm^{2+})/PL(Sm^{3+})$ trace observed on a previous run. It is worth noting that the X-ray induced absorbance in FP glass seems to be also erasable and reproducible as shown in Figure 3.6(b). Overall, we conclude that appropriate annealing at $T_A > T_g$ seems to lead to "complete

recovery" of the glass and thereby "prepares" it for the next run of irradiation. The importance of exceeding T_g is depicted in Figure 3.7(a), which shows that the process of erasure becomes efficient only when $T_A > T_g$.

We note that the practical definition of T_g in this work is based on the following operational definition. Figure 3.7(d) shows the heat capacity C_p (T) vs. T behavior as observed in TMDSC experiments (from the reversing heat flow component in the TMDSC measurement). There is a clear glass transformation region, which, as expected, is manifested as a step-like change in the C_p (T) vs. T behavior. The T_g is operationally defined as the temperature of the inflection point of the C_p (T) vs. T curve in this region. We note that the observed T_g is independent of the thermal history and depends only on the modulation frequency as described elsewhere [21].

Figure 3.7(a) clearly shows that Sm^{2+} is successfully erased, i.e., response $R(Sm^{2+}/Sm^{3+}) \rightarrow 0$ only at $T_A > T_g$, while at smaller T_A there is a considerable and unexpected increase of R which seems to correlate with the spectral shift of emission peaks corresponding to $^5D_0 \rightarrow {}^7F_0$, $^5D_0 \rightarrow {}^7F_1$, and $^5D_0 \rightarrow {}^7F_2$ optical transitions in Sm^{2+}; see Figure 3.7(b), Figure 3.8(a), and Figure 3.8(b). Meanwhile, the induced absorbance does not show any peculiarities and decreases monotonically with increasing T_A until above T_g where the induced absorbance is totally erased as shown in Figure 3.7(c). This unusual effect of "thermally stimulated enhancement" in Sm^{2+} emission is observed in both FP and FA host glasses and seems to be affected and further amplified by the codoping of FA glass with Eu^{2+}.

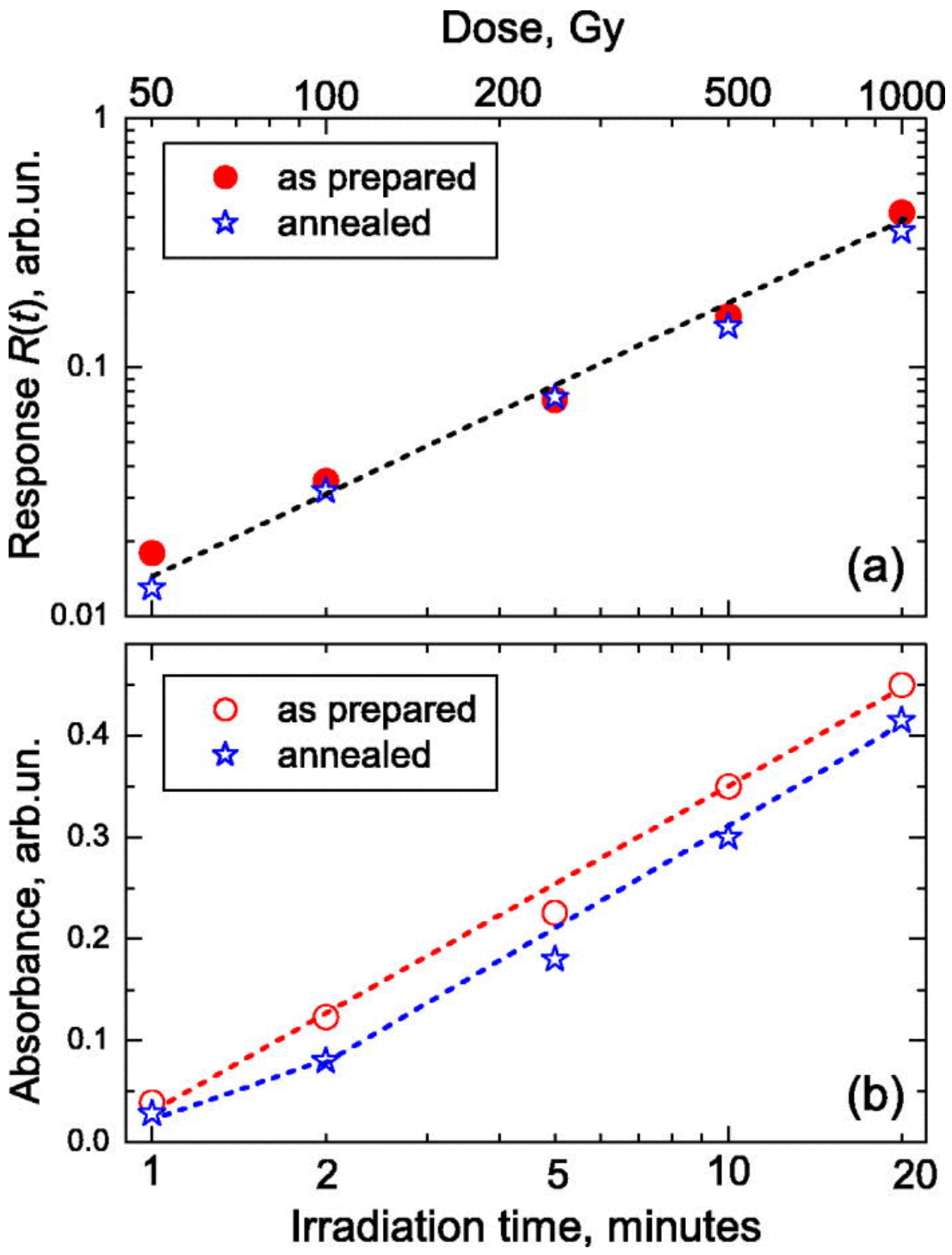

Figure 3.6 Erasability and reproducibility of $Sm^{3+} \rightarrow Sm^{2+}$ conversion in FP glass. (a) The ratio $PL(Sm^{2+})/PL(Sm^{3+})$ and (b) absorbance vs. dose of radiation before and after annealing at 550 °C for 30 min. The X-ray irradiation was performed in a FAXITRON X-ray chamber.

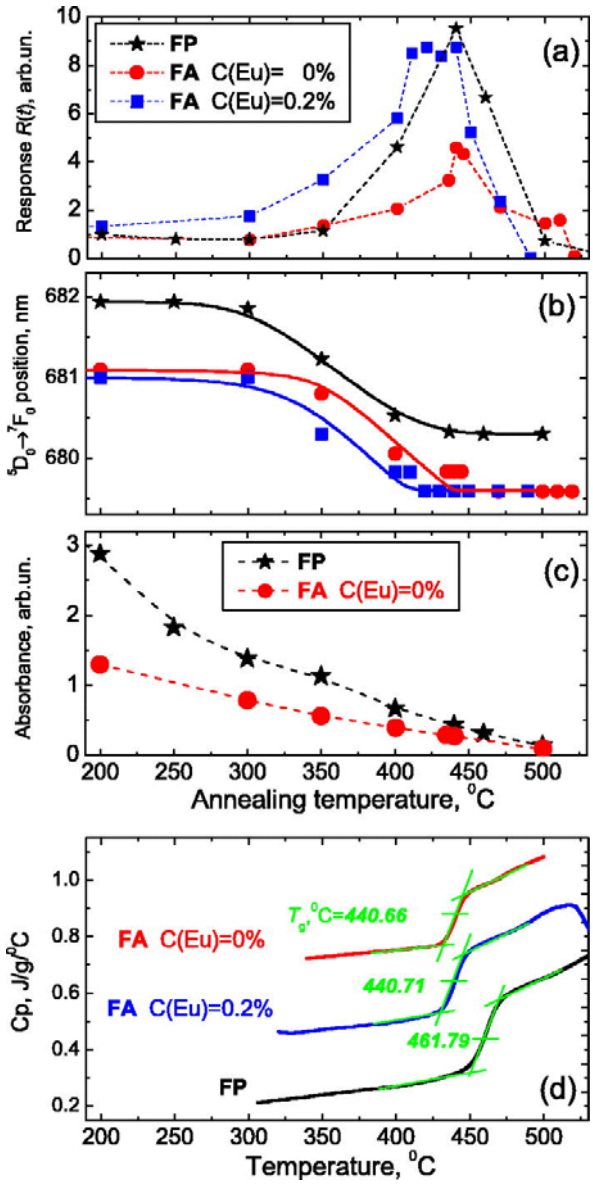

Figure 3.7 (a) Ratios $R(t) = \mathrm{PL}(Sm^{2+})/\mathrm{PL}(Sm^{3+})$ of FP and FA Sm-doped glasses versus annealing temperature T_A. The concentration of Sm^{3+} is 0.5% for all glasses. One of the FA glasses is codoped with 0.2% of Eu^{2+}. A sequential step-by-step annealing treatments were carried out at increasing temperatures. The time duration for every annealing step is 30 min. The irradiation was carried out at the Canadian Light Source. Lines are guides to the eye. (b) Spectral shift of $^5D_0 \rightarrow {}^7F_0$ singlet in Sm^{2+} emission in FP and FA glasses from (a) versus annealing temperature T_A. Lines are guides to the eye. (c) The integrated optical absorbance in FP and FA glasses from (a) versus annealing temperature T_A. The integrated optical absorbance was calculated as an integrated area of G1-G3 bands for FP glass and G1-G6 bands in FA glass. The definition of Gaussians G1-G3 and G1-G6 is given in Figure 3.2. Lines are guides to the eye. (d) Heat capacity (C_p) vs. temperature scan extracted from MDSC thermograms recorded at a heating rate 2 °C/min. The values on the scans show the inflection point, which was used as the operational definition of T_g .

Figure 3.9 shows the evolution of "thermally stimulated enhancement of Sm^{2+} emission" during the isothermal annealing at 400 °C. It can be clearly seen that, initially, the response $R(t)$ remains nearly constant while the X-ray induced absorbance rapidly decreases. At the same time, the $^5D_0 \rightarrow {}^7F_0$ emission peak position (λ_{max}) moves slowly towards shorter wavelengths as apparent in Figure 3.9(c) (see also Figure 3.8). At longer times exceeding 10 min, the induced absorbance becomes practically undetectable while $R(t)$ starts increasing and the shift in the $^5D_0 \rightarrow {}^7F_0$ peak position becomes more pronounced. The trend lines indicate that, eventually, $R(t)$ and λ_{max} reach saturation values.

We believe that there are two very general models of the observed effect of "thermally stimulated enhancement" which are worth considering. The first one is based on thermally stimulated additional direct $Sm^{3+} \rightarrow Sm^{2+}$ conversion, while the second one (which we favor) deals with the thermally stimulated reconstruction of ionic/atomic sites occupied by divalent Sm^{2+} ions.

Let us start with the first model of "thermally stimulated enhancement" due to *additional direct* $Sm^{3+} \rightarrow Sm^{2+}$ conversion. During the initial exposure, the X-ray irradiation creates electron-hole pairs. Some of the electrons are captured by Sm^{3+} ions which are converted into Sm^{2+} ions. Meanwhile, some of the other remaining electrons and holes become captured by "precursors" (which are specific configurations of ions/atoms) forming electron centers (ECs) and hole centers (HCs). During the annealing of the irradiated glass, the captured electrons and holes are released, leading to the destruction of ECs and HCs and hence to a monotonic reduction of induced absorbance. It seems natural that some of the thermally released electrons and holes may be recaptured by Sm^{3+} and Sm^{2+} ions, respectively. If, at some annealing

temperature, the release of electrons prevails over the release of holes, then we would expect additional $Sm^{3+} \rightarrow Sm^{2+}$ conversion.

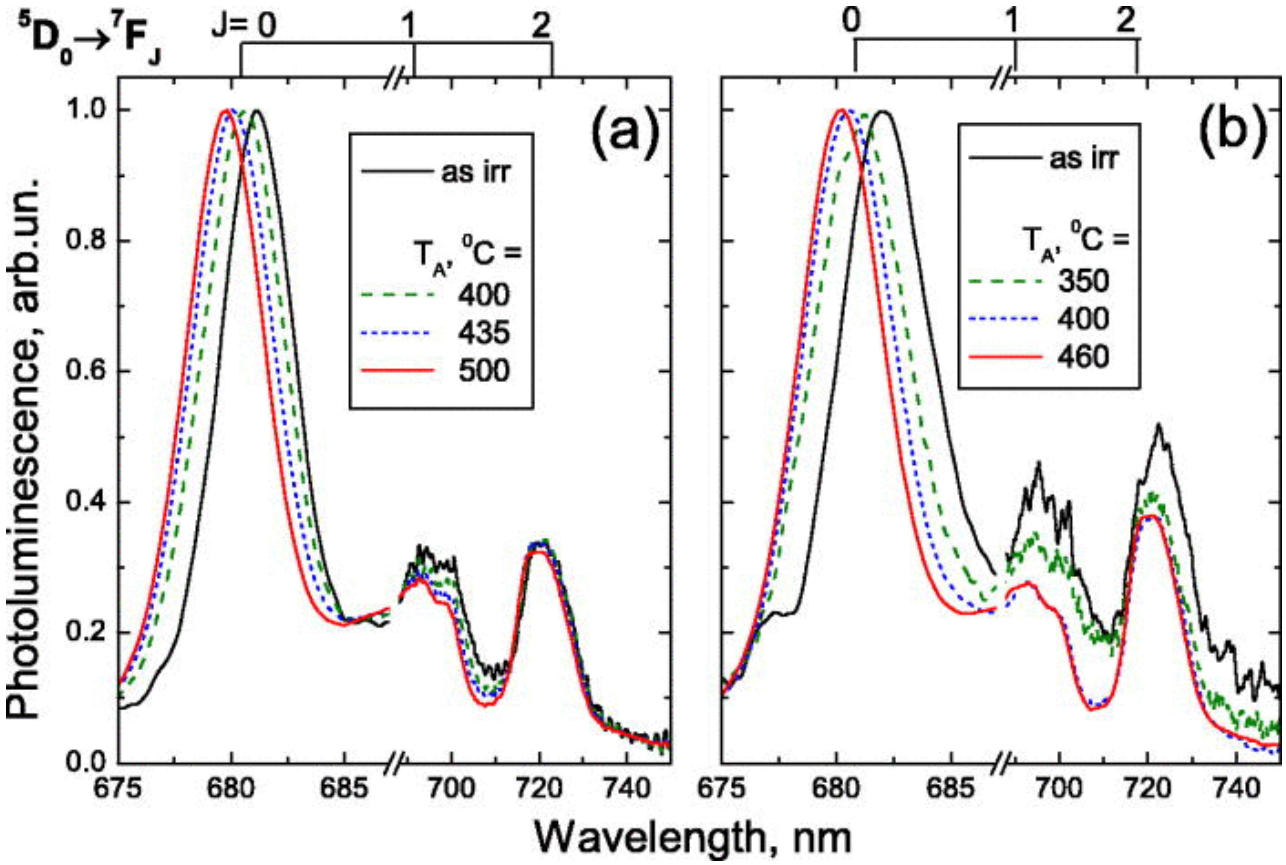

Figure 3.8 Variation of PL spectra of Sm^{2+} ions in FA (a) and FP (b) host glasses in the vicinity of $^5D_0 \rightarrow ^7F_J$ (J = 0,1,2) transitions as a result of thermal annealing at temperatures shown in the figure. The duration of all annealing periods is 30 min. The label "as irr" stands for as-irradiated samples prior to all annealing events. The X-ray irradiation was done using a FAXITRON X-ray chamber.

In other words, the whole idea of additional direct $Sm^{3+} \rightarrow Sm^{2+}$ conversion is based on the balance between electron and hole release rates from ECs and HCs, which may be influenced or controlled by introducing additional ions, for example Eu^{2+}. The latter ions are known to convert easily into Eu^{3+} under X-ray irradiation [30]. The trick is to choose the right concentration of Eu^{2+}. Figure 3.4(b) shows that the excessive addition of Eu^{2+} with concentrations exceeding 0.5% substantially decreases the efficiency of $Sm^{3+} \rightarrow Sm^{2+}$ conversion and makes FA glass

uninteresting for the present study. However, a moderate addition of Eu^{2+} in amounts ≤0.2% does not spoil the efficiency of the $Sm^{3+} \rightarrow Sm^{2+}$ conversion as can be seen in Figure 3.4(b) . Moreover, the $C_p(T)$ vs. T behavior remains the same as for undoped samples. In moderately codoped samples, the increase in R in "thermally stimulated enhancement" at annealing temperatures below T_g may be due to the thermally stimulated $Eu^{2+} \rightarrow Eu^{3+} + e^-$ reaction leading to the appearance of extra electrons, some of which can be captured by Sm^{3+} with the formation of Sm^{2+}. Figure 3.7(a) seems to support this idea and it does show that this moderate addition of 0.2% Eu leads to a substantial increase of the ratio $R(Sm^{2+}/Sm^{3+})$ in the annealing characteristics of these types of glasses, i.e., more thermally enhanced Sm^{2+} emission.

Unfortunately, there are three strong arguments against this model. First, despite our best efforts we could not detect the emission of Eu^{3+} which contradicts the idea of efficient X-ray induced $Eu^{2+} \rightarrow Eu^{3+}$ conversion. In these experiments, we used excitation with a laser diode operating at 532 nm which corresponded to the excitation of trivalent Eu^{3+} and Sm^{3+} only. Second, this model cannot provide an inherent explanation of the spectral shift of $^5D_0 \rightarrow {}^7F_j$ (j = 0, 1, 2) emission bands. Third, it does not provide any logical explanation for the observation of "photobleaching." Figure 3.10 shows that intense illumination may lead to partial or complete erasure of the PL of Sm^{2+}, an effect known as "photobleaching." Figure 3.10 indicates that in the as-irradiated sample, photobleaching is very effective and may lead to the complete disappearance of PL related to Sm^{2+} while for samples annealed at $T_A < T_g$, photobleaching is much less effective and never erases the conversed Sm^{2+} completely. Mathematically, this idea may be presented as shown in Figure 3.10 . Before annealing, $R(t)$ may be presented as a sum of two stretched exponentials approaching zero for long illumination

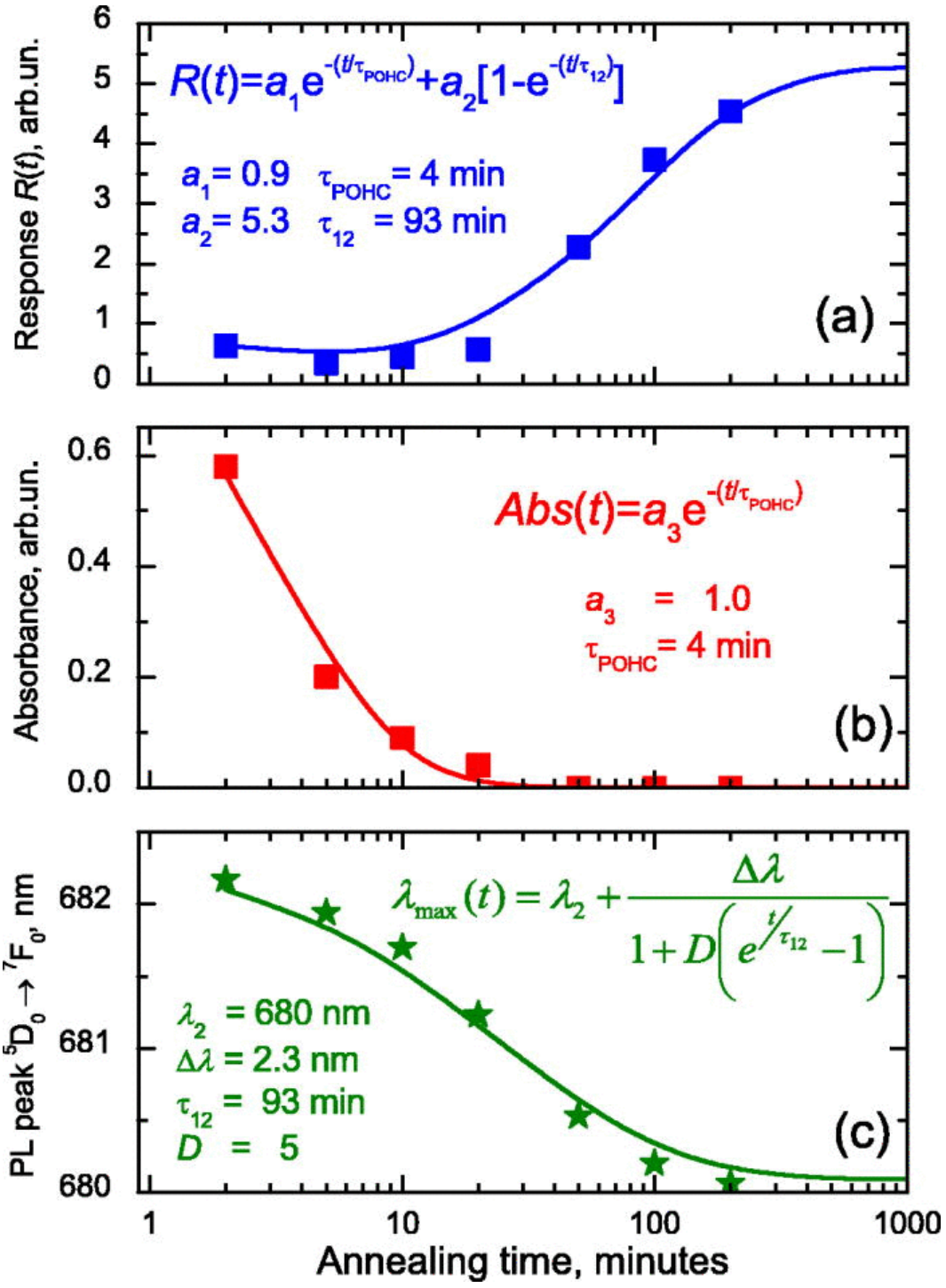

Figure 3.9 The effect of isothermal annealing at 400 °C on (a) ratio $R(t)$ = PL(Sm^{2+})/PL(Sm^{3+}); (b) induced absorbance; (c) spectral position of the Sm^{2+} ion in the $^5D_0 \rightarrow {}^7F_0$ emission maximum in Sm doped FP glass X-ray irradiated in a FAXITRON X-ray chamber. The lines in figures are fitting curves with parameters as shown in the figures.

times, i.e., $\lim_{t\to\infty} R(t) = 0$. After annealing at 420 °C $R(t)$ may be approximated by a sum of stretched exponential and a constant (R_∞) which means that $\lim_{t\to\infty} R(t) = R_\infty$. In other words, the photobleaching cannot completely erase the presence of divalent Sm^{2+}. In our opinion, the above three arguments rule out the model of *additional direct* $Sm^{3+} \rightarrow Sm^{2+}$ conversion.

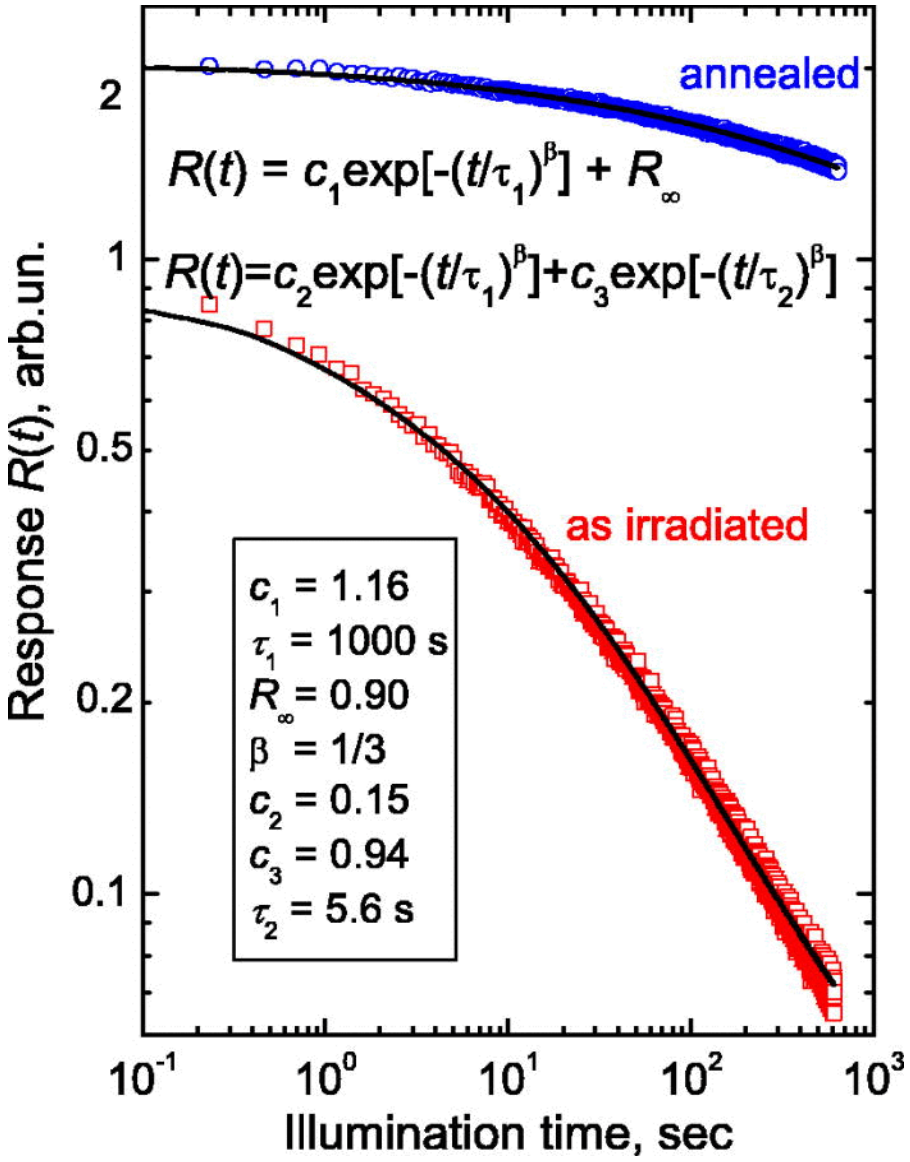

Figure 3.10 The effect of intense 472 nm illumination on PL(Sm^{2+})/PL(Sm^{3+}) ratio in X-ray irradiated Sm doped FP glass before and after annealing. Label "as irradiated" stands for glass irradiated in FAXITRON prior to annealing. The annealing was done at 420 °C for 30 min. Symbols are experimental data. Lines are the best fits using the formulas and fitting parameters as shown in the figure.

An alternative explanation of the observed effects is based on idea that at room temperature, a Sm^{3+} ion captures an X-ray generated electron to form Sm^{2+}, but the glass structure around it is "frozen" in place and cannot make the complete adjustment from the equilibrium environment around a Sm^{3+} ion to the equilibrium one around a Sm^{2+} ion until the sample is annealed. These Sm^{2+} ions with "frozen" unrelaxed environment are sometimes referred to as $(Sm^{3+})^{-}$ to distinguish them from stable Sm^{2+} ions [32]. The annealing process at moderate temperatures relaxes metastable Sm^{2+} into regular stable Sm^{2+}. Experimentally, the idea of different possible sites for Sm^{2+} ions is strongly supported by spectroscopic research showing that, in some glasses, the radiation induced divalent Sm^{2+} may reside in different sites characterized by a diverse ionic environment [31]. This relaxation of Sm^{2+} ionic environment is accompanied by the shifts of the position of $^5D_0 \rightarrow {}^7F_j$ (j = 0, 1, 2) emission bands, as in Figure 3.8, and may lead to the increase of PL intensity because an electron bound to a thermally relaxed Sm^{2+} site seems to be more tightly bound than one at an unrelaxed site (as follows from bleaching experiments shown in Figure 3.10). This tighter bond would increase simultaneously the efficiency of absorption too because in our PL experiments we use an excitation that corresponds to direct absorption by Sm^{2+} ions. From a general point of view, the idea of relaxed Sm^{2+} being a more efficient absorber and emitter than the unrelaxed one seems to be reasonable because unrelaxed Sm^{2+} may be considered as an "intermediate step" from Sm^{3+} to Sm^{2+} which is known to be approximately 300 times more effective as a light emitter than Sm^{3+} [38]. The above considerations allow us to develop a mathematical treatment of the model, which is summarized in the Appendix. The next problem to address is the reason for the "thermally stimulated enhancement" being stronger in the FA glass codoped with Eu^{2+}as in Figure 3.7(a). According to our DSC data on a glass that has no Eu codopant, the onset crystallization temperature is equal to 542.4 °C while the addition

of 0.2% of Eu increases it to 547.1 °C and it reaches 549.2 °C when the Eu-concentration is 0.5%. Further additions of Eu leads to the appearance of multiple crystallization peaks (not shown) which is evidence for the formation of a structure that is likely to be inhomogeneous. Therefore, the addition of 0.2% of Eu^{2+} clearly leads to some reconstruction of the glass matrix which might facilitate the relaxation of Sm^{2+} ionic environment stimulating absorption and emission.

3.5 Conclusion

Fluorophosphate and fluoroaluminate glasses doped with trivalent samarium were tested as sensors of X-ray radiation for microbeam radiation therapy. X-ray irradiation causes the reduction of trivalent Sm^{3+} to divalent Sm^{2+} form. The photoluminescence emission spectrum from Sm^{2+} is distinctly different than that from Sm^{3+}, which allows the ratio *R* of the two PL spectra to be used as a means to monitor the irradiation dose; *R* is effectively the response of this Sm-doped glass sensor to the dose delivered. Both materials show comparable sensitivity in terms of *R* vs. dose behavior, and may be used as a linear sensor up to ~150 Gy and as a nonlinear sensor up to ~2400 Gy where saturation is reached. Confocal fluorescence microscopy was used to measure the spatial variation of the dose across the incident beam. Experiments with a microslit collimator show high spatial resolution of the conversion pattern. Sequential X-ray irradiations show good reproducibility of the results. The effects of previous X-ray exposure may be erased by annealing at temperatures exceeding the glass transition temperature of the doped glass. The annealing at lower temperatures causes the effect of "thermally stimulated enhancement" of the photoluminescence associated with divalent samarium. The observed effects are explained assuming the existence of metastable Sm^{2+} in an unrelaxed ionic environment which is the direct result of X-ray irradiation. The subsequent annealing leads to the

relaxation and the appearance of stable Sm^{2+}. Some of the Sm-samples were codoped with Eu^{2+} but codoping did not provide any additional benefits.

Acknowledgment

We thank NSERC and the New Zealand Ministry for Science and Innovation for financial support and Teledyne-DALSA for sponsoring the project through NSERC. (Irradiation experiments described in this paper were performed at the Canadian Light Source, which is supported by NSERC, NRC, the Canadian Institutes of Health Research, the Province of Saskatchewan, Western Economic Diversification, Canada, and the University of Saskatchewan.)

3.6 Appendix: Modeling of Thermal Enhancement

The above considerations may be presented as a simple mathematical model. It assumes that Sm^{3+} ions coexist with Sm^{2+} ions in metastable (unrelaxed) and stable (relaxed) ionic environment, which for simplicity will be referred to as "stable" and "metastable" Sm^{2+} ions. Each state of the Sm-ion may be characterized by a potential energy, i.e., E_0 for Sm^{3+} and E_1 and E_2 for metastable and stable Sm^{2+}, respectively. The concentrations of Sm^{3+} and Sm^{2+} ions in metastable and stable ionic environments are assumed to be n_0, n_1, and n_2, respectively. In all practical cases, $n_0 \gg n_1$ and n_2, i.e., only small fraction of Sm^{3+} is actually reduced to Sm^{2+}.

In accordance with the experiments, the Sm-ions may be interconverted by applying different treatments. Thus, X-ray irradiation unambiguously causes Sm^{3+} conversion into metastable Sm^{2+} while the exact effect of thermal treatment depends on the temperature. Below T_g, the conversion of Sm^{2+} from metastable to stable configuration seems to be dominant while, at higher temperatures, the Sm^{2+} to Sm^{3+} reconversion is the major process. Both processes are

thermally activated, and may be characterized by activation energies and characteristic times (reciprocals of characteristic attempt to escape frequencies) as $\tau_{12}(T)=\tau_0\exp(\Delta E_{12}/kT)$ and $\tau_{20}(T)=\tau_0\exp(\Delta E_{20}/kT)$. Here, τ_{12} and ΔE_{12} are the characteristic time and activation energy of conversion of the metastable Sm^{2+} ion into stable one, and τ_{20} and ΔE_{20} are the analogous characteristics for the Sm^{2+} into Sm^{3+} reconversion. Although the exact value of the pre-exponential factor τ_0 is unknown, for the following, we assume it to be close to reciprocal phonon frequency, i.e., $\tau_0 \approx 10^{-12}$s.

In the present model, the Sm^{3+} to Sm $^{2+}$ conversion response may be calculated as

$$R(t) \propto \frac{n_1 D_1 + n_2 D_2}{n_0 D_0} \propto n_1 + n_2 D \qquad (3.2)$$

here, $D=D_2/D_1$ where D_0, D_1, and D_2 are the quantities characterizing the abilities of different Sm-ions to absorb excitation and to emit light. The product n_0D_0 refers to Sm^{3+} and is assumed to be constant. The products n_1D_1 and n_2D_2 refer to metastable and stable Sm^{2+} ions, respectively. Intuitively, D_0, D_1, and D_2 are related to oscillator strengths. The concentrations n_1 and n_2 are interrelated through a system of two differential equations

$$\frac{dn_1}{dt} = \frac{-n_1}{\tau_{12}} \qquad (3.3)$$

and

$$\frac{dn_2}{dt} = \frac{n_1}{\tau_{12}} - \frac{n_2}{\tau_{20}} \qquad (3.4)$$

Equation (3.3) describes the relaxation and conversion of metastable Sm^{2+} ions to stable ones, while Eq. (3.4) expresses the appearance of stable Sm^{2+} and its reconversion to Sm^{3+}. The exact solution of the system (3.3) and (3.4) depends on boundary conditions which, of course, depend on the conditions imposed on the experiments. In the case of a step by step annealing (Figure 3.7), the samples were annealed for $\Delta t = 30$ min sequentially at increasing temperatures.

Therefore, the boundary conditions for the first step of annealing should be taken as $n_{11}(0) = 1$ and $n_{21}(0) = 0$, i.e., after X-ray irradiation prior to any annealing all Sm^{2+}-ions are metastable and there is no stable Sm^{2+} at all. For the following steps, the recurrent boundary conditions may be applied as $n_{1k}(0) = n_{1k-1}(\Delta t)$ and $n_{2k}(0) = n_{2k-1}(\Delta t)$, i.e., the initial concentrations of metastable and stable Sm^{2+} ions in the beginning of the kth annealing step at temperature T_k are equal to final concentrations reached during the previous $(k-1)$th annealing step at T_{k-1}. With these boundary conditions, the solutions for a step (k) are

$$n_{1_k}(t) = n_{1_{k-1}}(\Delta t)e^{-\frac{t}{\tau_{12}}} \tag{3.5}$$

$$\begin{aligned} n_{2_k}(t) = & \frac{\tau^*(T_k)\, n_{1_{k-1}}(\Delta t)}{\tau_{12}(T_k)} \\ & \times\left[\left(\frac{\tau_{12}(T_k)\, n_{2_{k-1}}(\Delta t)}{\tau^*(T_k)\, n_{1_{k-1}}(\Delta t)}+1\right)e^{-\frac{t}{\tau_{20}(T_k)}} - e^{-\frac{t}{\tau_{12}(T_k)}}\right] \end{aligned} \tag{3.6}$$

where $1/\tau^* = 1/\tau_{12} - 1/\tau_{20}$.

The result of calculations of $n_1(t)$ and $n_2(t)$ is shown in Figure 3.11(c) . By applying Eq. (3.2) one can get reasonable agreement with the experimental data shown in Figure 3.11(a). A set of adjustable parameters that give the best agreement with experimental data for each FA glass is shown in Figure 3.11(a).

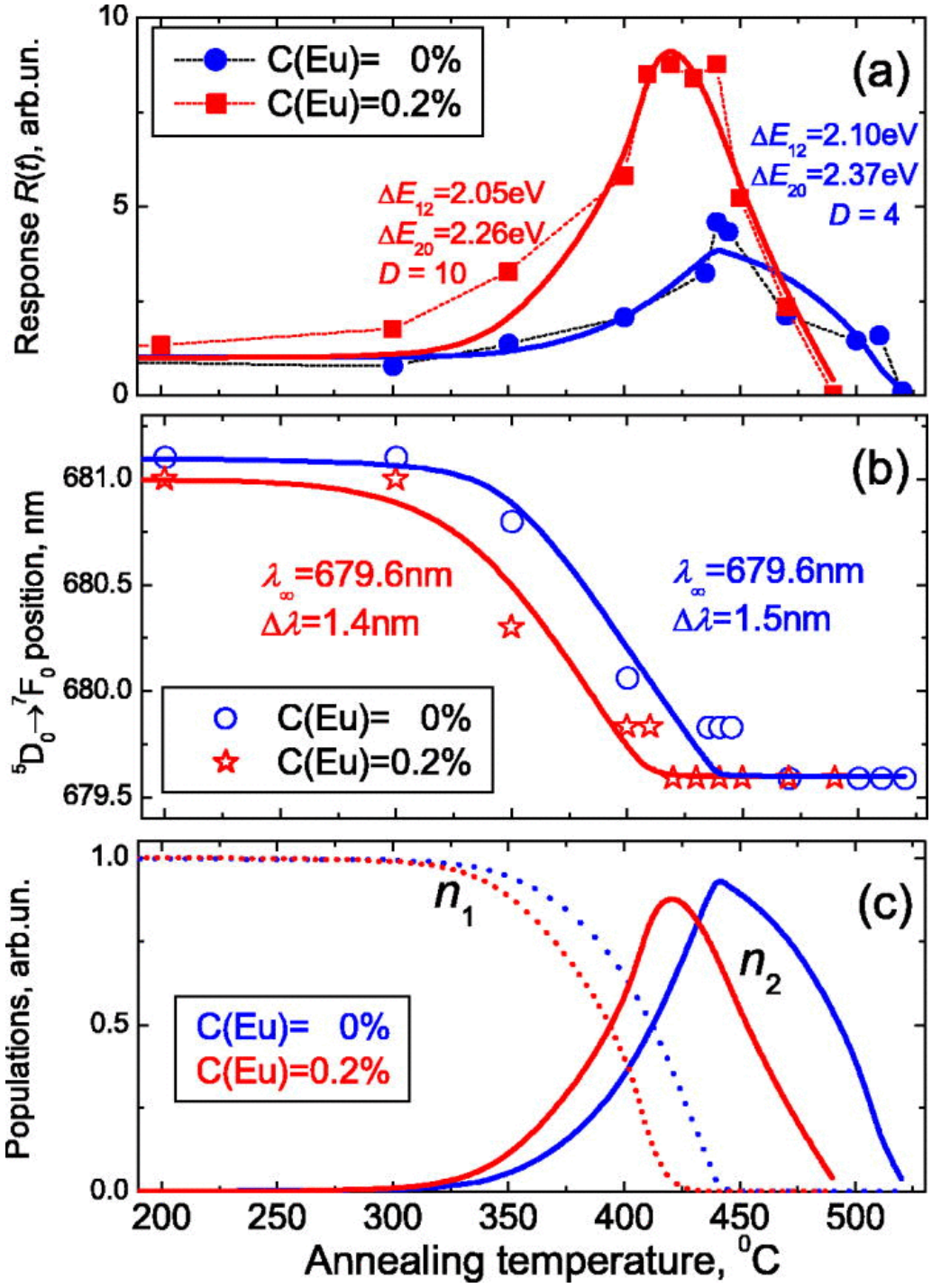

Figure 3.11 The comparison of model predictions with experimental data. (a) Ratios $R(t) = \mathrm{PL}(Sm^{2+})/\mathrm{PL}(Sm^{3+})$ of FA Sm-doped glasses versus annealing temperature T_A. The samples and experimental procedure are the same as in Figure 3.7. The lines are fitting curves with parameters as shown in the figure. (b) Spectral shift of $^5D_0 \rightarrow {}^7F_0$ singlet in Sm^{2+} emission of the same glasses versus annealing temperature T_A. The lines are fitting curves with parameters as shown in the figures. (c) Calculated concentrations of divalent Sm ions in (1) metastable and (2) stable configurations.

This approach may be also used to calculate the spectral shift of the maximum of the $^5D_0 \rightarrow {}^7F_0$ emission spectrum. Let us assume that $\Phi_1(\lambda)$ and $\Phi_2(\lambda)$ are the normalized spectra of metastable and stable Sm^{2+} with maxima at λ_1 and λ_2, respectively. In this case, the emission spectrum is a mixture of both spectra

$$\Phi(\lambda) = n_1 D_1 \Phi_1(\lambda) + n_2 D_2 \Phi_2(\lambda) \propto \Phi_1(\lambda) + D\frac{n_2}{n_1}\Phi_2(\lambda) \qquad (3.7)$$

Assuming that $\Phi_1(\lambda)$ and $\Phi_2(\lambda)$ are smooth functions around λ_1 and λ_2 and spectral shift is small $\Delta\lambda = \lambda_1 - \lambda_2 \ll \lambda_1, \lambda_2$ one can easily get the shift of spectral maximum as

$$\lambda_{\max}(t) = \lambda_\infty + \frac{\Delta\lambda}{1 + D\dfrac{n_2(t)}{n_1(t)}} \qquad (3.8)$$

here, $\lambda_\infty = \lambda_2$ and $\Delta\lambda = \lambda_1 - \lambda_2$. The best fit to experimental data along with required adjustable parameters is given in Figure 3.11(b).

In a similar way, we can model the effects of isothermal annealing for the FP glass, which are shown in Figure 3.9 for $T_A = 400$ °C. The results of calculations are shown as solid lines.

3.7 References

1. D. N. Slatkin, P. Spanne, F. A. Dilmanian, and M. Sandborg, "Microbeam radiation therapy," Med Phys **19**, 1395-1400 (1992).

2. F. A. Dilmanian, P. Romanelli, Z. Zhong, R. L. Wang, M. E. Wagshul, J. Kalef-Ezra, M. J. Maryanski, E. M. Rosen, and D. J. Anschel, "Microbeam radiation therapy: Tissue dose penetration and BANG-gel dosimetry of thick-beams' array interlacing," European Journal of Radiology **68**, S129-S136 (2008).

3. J. C. Crosbie, R. L. Anderson, K. Rothkamm, C. M. Restall, L. Cann, S. Ruwanpura, S. Meachem, N. Yagi, I. Svalbe, R. A. Lewis, B. R. G. Williams, and P. A. W. Rogers, "Tumor Cell Response to Synchrotron Microbeam Radiation Therapy Differs Markedly from Cells in Normal Tissues," Int J Radiat Oncol **77**, 886-894 (2010).

4. J. A. Laissue, N. Lyubimova, H.-P. Wagner, D. W. Archer, D. N. Slatkin, M. Di Michiel, C. Nemoz, M. Renier, E. Brauer, P. O. Spanne, J.-O. Gebbers, K. Dixon, and H. Blattmann, "Microbeam radiation therapy," in *Proc. SPIE*(1999), pp. 38-45.

5. M. Torikoshi, Y. Ohno, N. Yagi, K. Umetani, and Y. Furusawa, "Dosimetry for a microbeam array generated by synchrotron radiation at SPring-8," European Journal of Radiology **68**, S114-S117 (2008).

6. E. Brauer-Krisch, H. Requardt, T. Brochard, G. Berruyer, M. Renier, J. A. Laissue, and A. Bravin, "New technology enables high precision multislit collimators for microbeam radiation therapy," Review of Scientific Instruments **80** (2009).

7. E. Brauer-Krisch, A. Rosenfeld, M. Lerch, M. Petasecca, M. Akselrod, J. Sykora, J. Bartz, M. Ptaszkiewicz, P. Olko, A. Berg, M. Wieland, S. Doran, T. Brochard, A. Kamlowski, G. Cellere, A. Paccagnella, E. A. Siegbahn, Y. Prezado, I. Martinez-Rovira, A. Bravin, L. Dusseau, and P. Berkvens, "Potential High Resolution Dosimeters For MRT," 6th International Conference on Medical Applications of Synchrotron Radiation **1266**, 89-97 (2010).

8. T. Ackerly, J. C. Crosbie, A. Fouras, G. J. Sheard, S. Higgins, and R. A. Lewis, "High resolution optical calorimetry for synchrotron microbeam radiation therapy," J Instrum **6** (2011).

9. D. Maki, T. Ishii, F. Sato, Y. Kato, T. Yamamoto, and T. Iida, "Development of Confocal Laser Microscope System for Examination of Microscopic Characteristics of Radiophotoluminescence Glass Dosemeters," Radiat Prot Dosim **144**, 222-225 (2011).

10. A. T. A. Rahman, D. A. Bradley, S. J. Doran, B. Thierry, E. Brauer-Krisch, and A. Bravin, "The thermoluminescence response of Ge-doped silica fibres for synchrotron microbeam radiation therapy dosimetry," Nucl Instrum Meth A **619**, 167-170 (2010).

11. N. Nariyama, T. Ohigashi, K. Umetani, K. Shinohara, H. Tanaka, A. Maruhashi, G. Kashino, A. Kurihara, T. Kondob, M. Fukumoto, and K. Ono, "Spectromicroscopic film dosimetry for high-energy microbeam from synchrotron radiation," Appl Radiat Isotopes **67**, 155-159 (2009).

12. e. a. G. Belev, "Valency conversion of samarium ions under high dose synchrotron generated X-ray radiation," physica status solidi (c) **8**, 2822–2825 (2011).

13. D. L. Griscom, E. J. Friebele, K. J. Long, and J. W. Fleming, "Fundamental Defect Centers in Glass - Electron-Spin Resonance and Optical-Absorption Studies of Irradiated Phosphorus-Doped Silica Glass and Optical Fibers," J Appl Phys **54**, 3743-3762 (1983).

14. K. Miura, J. R. Qiu, S. Fujiwara, S. Sakaguchi, and K. Hirao, "Three-dimensional optical memory with rewriteable and ultrahigh density using the valence-state change of samarium ions," Appl Phys Lett **80**, 2263-2265 (2002).

15. J. Lim, M. Lee, and E. Kim, "Three-dimensional optical memory using photoluminescence change in Sm-doped sodium borate glass," Appl Phys Lett **86**, - (2005).

16. E. Malchukova, B. Boizot, G. Petite, and D. Ghaleb, "Optical properties and valence state of Sm ions in aluminoborosilicate glass under beta-irradiation," J Non-Cryst Solids **353**, 2397-2402 (2007).

17. Y. Huang, C. Jiang, K. Jang, H. S. Lee, E. Cho, M. Jayasimhadri, and S.-S. Yi, "Luminescence and microstructure of Sm2+ ions reduced by x-ray irradiation in Li2O–SrO–B2O3 glass," J Appl Phys **103**, - (2008).

18. C. A. G. Kalnins, H. Ebendorff-Heidepriem, N. A. Spooner, and T. M. Monro, "Optically Stimulated Luminescence in Fluoride–Phosphate Glass for Radiation Dosimetry," J Am Ceram Soc **94**, 474-477 (2011).

19. G. Okada, B. Morrell, C. Koughia, A. Edgar, C. Varoy, G. Belev, T. Wysokinski, D. Chapman, and S. Kasap, "Spatially resolved measurement of high doses in microbeam radiation therapy using samarium doped fluorophosphate glasses," Appl Phys Lett **99** (2011).

20. H. Ebendorff-Heidepriem, and D. Ehrt, "Effect of Tb3+ ions on X-ray-induced defect formation in phosphate containing glasses," Opt Mater **18**, 419-430 (2002).

21. D. Tonchev, and S. O. Kasap, "Effect of aging on glass transformation measurements by temperature modulated DSC," Materials Science and Engineering: A **328**, 62-66 (2002).

22. M. Nogami, Y. Abe, K. Hirao, and D. H. Cho, "Room temperature persistent spectra hole burning in Sm2+-doped silicate glasses prepared by the sol-gel process," Appl Phys Lett **66**, 2952-2954 (1995).

23. M. Nogami, and Y. Abe, "Fluorescence spectroscopy of silicate glasses codoped with Sm2+ and Al3+ ions," J Appl Phys **81**, 6351-6356 (1997).

24. J. R. Qiu, K. Miura, T. Suzuki, T. Mitsuyu, and K. Hirao, "Permanent photoreduction of Sm3+ to Sm2+ inside a sodium aluminoborate glass by an infrared femtosecond pulsed laser," Appl Phys Lett **74**, 10-12 (1999).

25. L. D. Bogomolova, Y. G. Teplyakov, V. A. Jachkin, V. L. Bogdanov, V. D. Khalilev, F. Caccavale, and S. Lo Russo, "On the formation of paramagnetic defects in ion-implanted fluoroaluminate glasses," J Non-Cryst Solids **202**, 178-184 (1996).

26. T. V. Bocharova, G. O. Karapetyan, A. M. Mironov, N. M. Mishchenkov, and N. O. Tagil'tseva, "Irradiation-induced and postirradiation processes in fluoroaluminate glasses," Inorg Mater+ **42**, 671-680 (2006).

27. D. Ehrt, P. Ebeling, and U. Natura, "UV Transmission and radiation-induced defects in phosphate and fluoride-phosphate glasses," J Non-Cryst Solids **263**, 240-250 (2000).

28. K. Tanimura, W. A. Sibley, M. Suscavage, and M. Drexhage, "Radiation effects in fluoride glasses," J Appl Phys **58**, 4544-4552 (1985).

29. P. Ebeling, D. Ehrt, and M. Friedrich, "X-ray induced effects in phosphate glasses," Opt Mater **20**, 101-111 (2002).

30. J. R. Qiu, Y. Shimizugawa, Y. Iwabuchi, and K. Hirao, "Photostimulated luminescence in Eu2+-doped fluoroaluminate glasses," Appl Phys Lett **71**, 759-761 (1997).

31. N. Ollier, B. Boizot, P. L'henoret, S. Guillous, and G. Petite, "Evidence of transient species occurring in the reduction process of trivalent lanthanides under 2.5 MeV electron irradiation by in situ cathodoluminescence and time-resolved photoluminescence," J Appl Phys **105** (2009).

32. T. V. Bocharova, G. O. Karapetyan, A. M. Mironov, N. O. Tagil'tseva, and V. D. Khalilev, "Specific features of the induced absorption spectra of fluoroaluminate glasses doped with samarium ions," Glass Phys Chem+ **29**, 7-10 (2003).

33. L. Y. Yang, N. Da, D. P. Chen, Q. Z. Zhao, X. W. Jiang, C. S. Zhu, and J. R. Qiu, "Valence state change and refractive index change induced by femtosecond laser irradiation in Sm3+ doped fluoroaluminate glass," J Non-Cryst Solids **354**, 1353-1356 (2008).

34. J. R. Qiu, K. Nouchi, K. Miura, T. Mitsuyu, and K. Hirao, "Room-temperature persistent spectral hole burning of x-ray-irradiated Sm3+-doped glass," J Phys-Condens Mat **12**, 5061-5067 (2000).

35. P. W. Levy, "The Kinetics of Gamma-Ray Induced Coloring of Glass," J Am Ceram Soc **43**, 389-395 (1960).

36. D. L. Griscom, "Defect Centers in Heavy-Metal Fluoride Glasses - a Review," J Non-Cryst Solids **161**, 45-51 (1993).

37. R. Li, H. Wang, and F. Gan, "ESR study of temperature dependence of colour centers in γ-ray irradiated fluoride glasses," J Non-Cryst Solids **140**, 194-198 (1992).

38. C. Koughia, A. Edgar, C. R. Varoy, G. Okada, H. von Seggern, G. Belev, C.-Y. Kim, R. Sammynaiken, and S. Kasap, "Samarium-Doped Fluorochlorozirconate Glass–Ceramics as Red-Emitting X-Ray Phosphors," J Am Ceram Soc **94**, 543-550 (2011).

4 Optically Erasable Samarium-Doped Fluorophosphate Glasses for High-Dose Measurements in Microbeam Radiation Therapy

Published as:

Brian Morrell, Go Okada, Shahrzad Vahedi, Cyril Koughia, Andy Edgar, Chris Varoy, George Belev, Tomasz Wysokinski, Dean Chapman, Ramaswami Sammynaiken and Safa Kasap, "Optically erasable samarium-doped fluorophosphate glasses for high-dose measurements in microbeam radiation therapy", *Journal of applied physics,* 115, 063107, February 2014.

Author contributions:

Shahrzad Vahedi contributed in thermal annealing experiments and data analysis including induced absorbance "band separation" shown in Figure 4.5 and Table 4.1 and ESR spectra approximation shown in Figure 4.6 and Table 4.2. These approximations are used in Figure 4.3. She also contributed in the dose measurements and preparing the manuscript.

4.1 Abstract

Previous work has demonstrated that fluorophosphate (FP) glasses doped with trivalent samarium (Sm^{3+}) can be used as a dosimetric detector in microbeam radiation therapy (MRT) to measure high radiation doses and large dose variations with a resolution in the micrometer range. The present work addresses the use of intense optical radiation at 405 nm to erase the recorded dose information in Sm^{3+}-doped FP glass plates and examines the underlying physics. We have evaluated both the conversion and optical erasure of Sm^{3+}-doped FP glasses using synchrotron-generated high-dose X-rays at the Canadian Light Source. The Sm-ion valency conversion is accompanied by the appearance of X-ray induced optical absorbance due to the trapping of holes and electrons into phosphorus-oxygen hole (POHC) and electron (POEC)

capture centers. Nearly complete Sm^{2+} to Sm^{3+} reconversion (erasure) may be achieved by intense optical illumination. Combined analysis of absorbance and electron spin resonance measurements indicates that the optical illumination causes partial disappearance of the POHC and the appearance of new POEC. The suggested model for the observed phenomena is based on the release of electrons during the Sm^{2+} to Sm^{3+} reconversion process, the capture of these electrons by POHC (and hence their disappearance), or by PO groups, with the appearance of new and/or additional POEC. Optical erasure may be used as a practical means to erase the recorded data and permits the reuse of these Sm-doped FP glasses in monitoring dose in MRT.

4.2 Introduction

Radiation induced valency conversion of rare earth ions in various solids is of great scientific and practical interest. Numerous researches have demonstrated the possibility of valence conversion of different ions in a variety of host materials under different forms of excitation, such as X-ray, γ- and β-irradiation as well as optical excitation [1-6]. Among the rare earth ions, Sm^{3+} to Sm^{2+}conversion is of particular interest because the dominant emission bands of Sm^{3+} and Sm^{2+} ions are readily distinguishable. In addition, all dominant bands are situated in the red region of the spectrum. There is therefore a good match to silicon-based detectors used in optical measurements. Recent work has also demonstrated that Sm^{3+} to Sm^{2+} conversion may provide submicron spatial resolution with respect to optical storage of information [1-2]. Samarium, of course, is not the only rare-earth element that can possess multivalency states, depending on the host medium. Europium is another good example of a multivalent ion whose valence changes can be optically detected [7-8].

Recently, we have investigated the Sm^{3+} to Sm^{2+} valency conversion in Sm-doped fluorophosphate (FP) and fluoroaluminate glasses for potential use as dosimetric plates with high

spatial resolution for Microbeam Radiation Therapy (MRT) [9-10]. This is an experimental form of radiation treatment that has the potential to improve the treatment of many types of cancer compared with customary broad-beam radiation treatment; the microbeam that is used in this form of therapy is normally generated at a synchrotron facility [11-15]. The MRT is based on the markedly different responses of tumor and normal cells to this form of treatment at the cell level as recently discussed in a paper by Crosbie *et al.* [16]. In practice, the radiation is applied in the form of a grid by passing the highly collimated X-ray beam from a synchrotron through a microplane collimator, which is a stack of parallel plates of two materials with dramatically different X-ray transparencies [17-18].

The accurate, simultaneous recording of peak and valley doses that differ by hundreds of grays, and the large dose gradients (hundreds of grays over several microns) in the whole X-ray energy range of interest for MRT (50–250 keV) are an extremely challenging task. No current detector can satisfactorily meet all these requirements. The research and development of detectors suitable for MRT has therefore become an important goal if MRT is to advance further. Detectors, such as ionization chambers, alanine dosimeters, MOSFET detectors, Gafchromic® films, radiochromic polymers, Thermoluminescence Detectors (TLDs), polymer gels, Fluorescent Nuclear Track Detectors (FNTDs, based on Al_2O_3:C, Mg single crystal detectors), optically stimulated luminescence detectors, and floating gate-based dosimeters have been reviewed with respect to their potential applications in MRT [19]. The latest attempts to solve the problem are based on using damage caused by X-ray irradiation to biological objects [20], aluminum oxide fluorescent detectors [21], high resolution optical Calorimetry [22], confocal laser microscopy of the radiophotoluminescence (PL) of silver activated phosphate glass [23], thermoluminescence of Ge-doped silica fibers [24], silicon strip detector

[25], and spectromicroscopic film dosimetry [26]. Another novel approach is the valence conversion of rare earth ions embedded in a suitable host material upon irradiation as discussed by the present group [27].

In an earlier work, we showed the applicability of Sm-doped FP glasses as a potential dosimetric material to measure both the dose and the peak-to-valley dose ratio (PVDR), a critical parameter for successful MRT. We demonstrated the efficiency of $Sm^{3+} \rightarrow Sm^{2+}$ conversion in these glasses and illustrated the feasibility of a spatially resolving dosimetric sensor based on the confocal detection of photoluminescence [9]. We also demonstrated that the effects of irradiation may be erased by annealing at temperatures exceeding the glass transition temperature T_g (= 450–470 °C for these glasses) [10]. Meanwhile, annealing at lower temperatures leads to a "thermal enhancement" effect, which was also discussed in detail in Ref. [10]. It seems obvious that the use of thermal annealing at temperatures exceeding T_g for the erasure of previously collected information is not a particularly convenient procedure that can be quickly implemented in field, and allow the reuse of the detector soon after it had been irradiated. Therefore, in the present paper, we discuss the possibility of erasure by using intense UV light and discuss the related problems associated with this type of erasure.

Our choice of a fluorophosphate glass as a host for Sm^{3+} is based on three important factors. First, fluorophosphate glasses are known to be good hosts for rare-earth ions and have been of recent scientific interest [28-29]. Secondly, there is considerable published work on Sm^{3+}-doped fluorophosphate glasses, in particular, on their optical properties [30–32]. Thirdly, and most importantly, comparatively few glasses show X-ray induced conversion of Sm^{3+} to Sm^{2+}, as we have reported in previous papers [10,27], but Sm-doped fluorophosphate glasses show good conversion, even under low dose exposure that can be easily detected by photoluminescence

experiments. The latter interesting observation is connected with the formation of hole and electron centers as discussed below. Another relevant observation is the fact that Sm^{3+} ions embedded in various types of polycrystalline samples do seem to convert relative easily to Sm^{2+} when exposed to X-rays [27]. However, polycrystalline samples are not suitable for MRT dosimetry as they do not allow high resolution confocal fluorescence readout from converted Sm^{2+} ions inasmuch as light scattering broadens the detected signal, reducing the effective spatial resolution.

4.3 Experimental

FP glasses can be thought as a combination of fluoride and phosphate glasses with a variety of possible cationic species. The composition and preparation are based on the FP10 composition published by Ebendorff-Heidepriem [30]. The FP10 batch composition, given in mol. %, is $10.0Sr(PO_3)_2$-$34.4AlF_3$-$10MgF_2$-$30.4CaF_2$-$15.2SrF_2$. The FP10 glasses were doped with Sm^{3+} by adding the SmF_3 in amounts from 0.001 to 0.5 mol. %. The quenched glass samples were cut and polished flat for X-ray and optical measurements.

The X-ray irradiation was performed by two different methods. The first method used a synchrotron radiation at the Biomedical Imaging and Therapy 05B1-1 bend magnet beamline at the Canadian Light Source (CLS), Saskatoon, Canada. The spectrum of filtered X-ray radiation had a maximum around 50 keV [9]. The intensity of synchrotron X-ray irradiation corresponded to an approximate dose rate of 2 Gy/s (±20%). The second irradiation method, which was more convenient, simply used the emission produced by a commercial FAXITRON X-ray tube with a tungsten anode operating at 110 kVp (3 mA filament current) with an approximate dose rate of 0.8 Gy/s. The X-ray tube has a 0.76 mm Be window through which the radiation passed onto the sample, approximately 5 cm from the anode. The mean photon energy was 45.2 keV. The quoted

dose rates represent dose in air at the surface of the sample, which is the usual manner in which dose is reported for MRT.

We have also exposed the samples to an X-ray microbeam at the CLS of the type that would be used in MRT. The microbeam was produced by passing a highly collimated X-ray beam through an 8 mm thick Tungsten/Air multislit collimator (MSC) manufactured by Usinage et Nouvelles Technologies, Morbier, France. The microbeams are 50 μm wide and have centre-to-centre distance of 400 μm (which is the spatial periodicity). Further details may be found elsewhere [9].

The steady-state PL spectra were measured from 200 nm to either 1100 or 1200 nm. For 200–1100 nm measurements, we used a Stellar Net EPP2000 fiber input mini-spectrometer, with a spectral resolution around 4 nm. For 200–1200 nm measurements, we used an ASEQ fiber input mini-spectrometer with spectral resolution better than 1 nm. The excitation source for the photoluminescence spectra was typically a laser diode with an emission wavelength at 405 nm and power 15 mW, which can be used to excite both the Sm^{3+} and Sm^{2+} ions [33]. The intensity of excitation was kept as low as possible to minimize the effect of $Sm^{2+} \rightarrow Sm^{3+}$ reconversion during the measurements. The transmittance spectra were measured using a Perkin-Elmer Lambda 900 spectrophotometer. Electron Spin Resonance (ESR) spectroscopy experiments were conducted on a standard Bruker EMX 10/2.7 instrument.

The erasure illumination was typically carried out by using a violet LED operating at 405 nm with power density of ~100 mW/cm^2 on the sample. In one set of experiments (Figure 4.1) a laser diode emitting at 405 nm was used, which gave a power density ~30 mW/cm^2 on the sample.

4.4 Results and Discussion

Figure 4.1 summarizes the essence of the problem that is being addressed. The X-ray microbeam exiting a multislit collimator is made incident on a Sm-doped FP glass plate, and

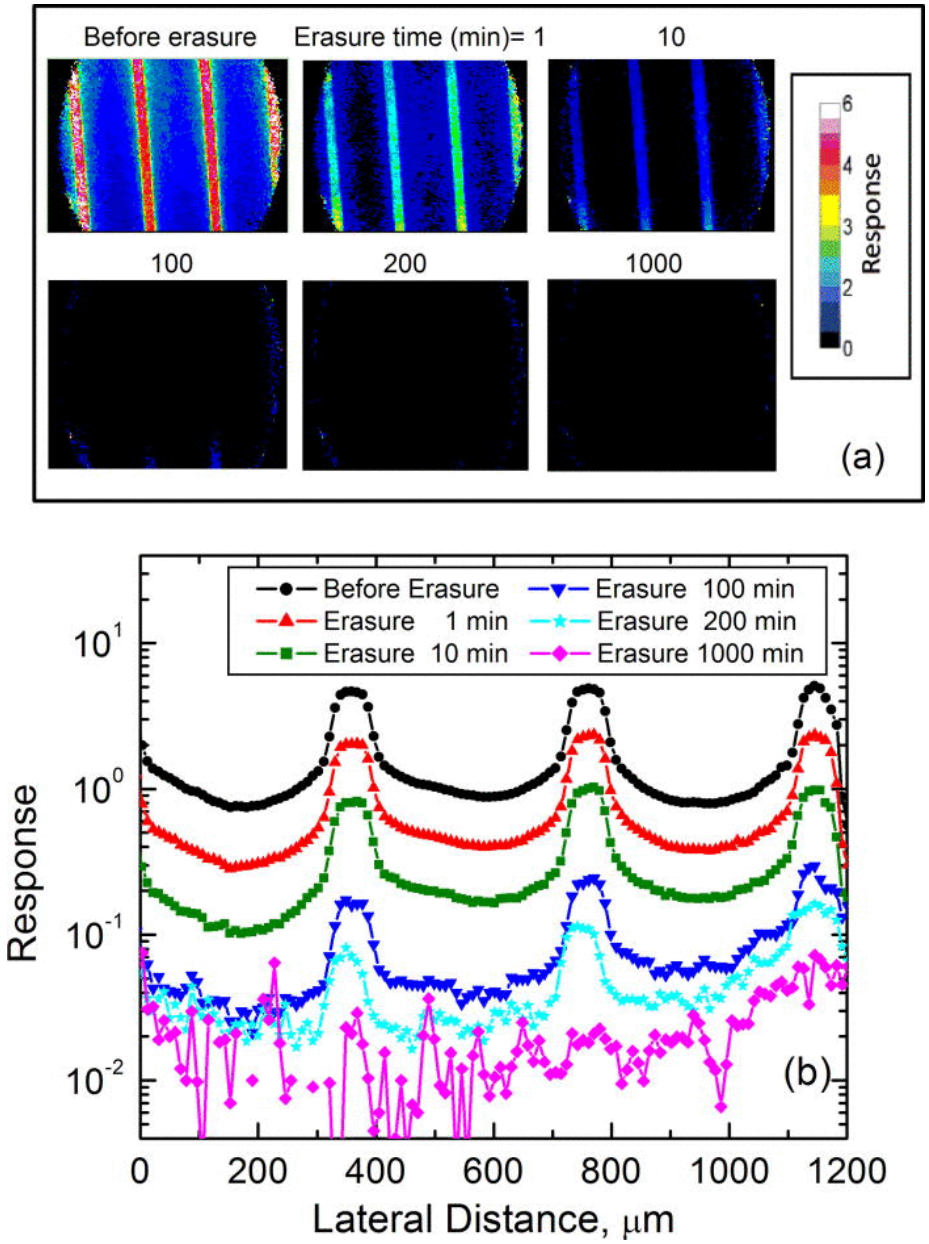

Figure 4.1 X-ray irradiation dose profile images (a) two dimensional and (b) one dimensional before and after optical erasure for different durations of erasure illumination. The peak dose was ~5 kGy. PL excitation wavelength was 470 nm. The optical erasure source was a laser diode emitting at a wavelength of 405 nm. The average erasure illumination power density was ~30 mW/cm ^{2} on the sample.

induces Sm^{3+} to Sm^{2+} conversion. The spatial variation of this conversion on the Sm-doped FP glass is recorded and digitized by examining the PL of Sm^{2+} and Sm^{3+} ions, excited by a low power laser diode operating at 470 nm through a confocal scanning fluoroscopic microscope. Numerically, the degree of Sm^{3+} to Sm^{2+}conversion may be characterized by a response ratio function $R(t)$, or simply called "response," defined by

$$R(t) = \mathrm{PL}_{\mathrm{Sm}^{2+}}(t) / \mathrm{PL}_{\mathrm{Sm}^{3+}}(t),$$

where $PL_{Sm}{}^{2+}(t)$ and $PL_{Sm}{}^{3+}(t)$ are the integrated photoluminescence of Sm^{2+} and Sm^{3+} bands, respectively, which depend on the time (duration) of irradiation t; note that the total dose is proportional to this time t, given that the dose rate is constant. The exact method of calculating the response $R(t)$ is discussed in detail in our previous work [10,34]. Figure 4.1 shows the spatial distribution of response R after ~5 kGy dose delivered through the multislit collimator as measured by a confocal fluoroscopic microscope. After the dose distribution has been measured, the specimen must be re-initialized for a second measurement. In other words, the results of previous irradiation should be erased so that the glass plate can be reused. We have already shown that the full erasure may be achieved by annealing at temperatures above the glass transition, which is typically around 450–470 °C for FP glasses [10]. An alternative to erasure by annealing is an erasure by an intense optical illumination. Figure 4.1 shows the general effect of optical erasure by intense illumination at 405 nm for different durations of illumination. Figure 4.2(a) highlights the effect of erasure by showing the evolution of the PL spectra from an FP10 glass doped with Sm^{3+}. The initial spectrum of "as-prepared" non-irradiated glass contains only emission bands associated with Sm^{3+} ions. X-ray irradiation induces additional bands, typical for Sm^{2+} ions, which are an indication of the partial conversion of Sm^{3+} into Sm^{2+}. The subsequent erasure reduces and, within 20 min, nearly erases all Sm^{2+} emission bands, which

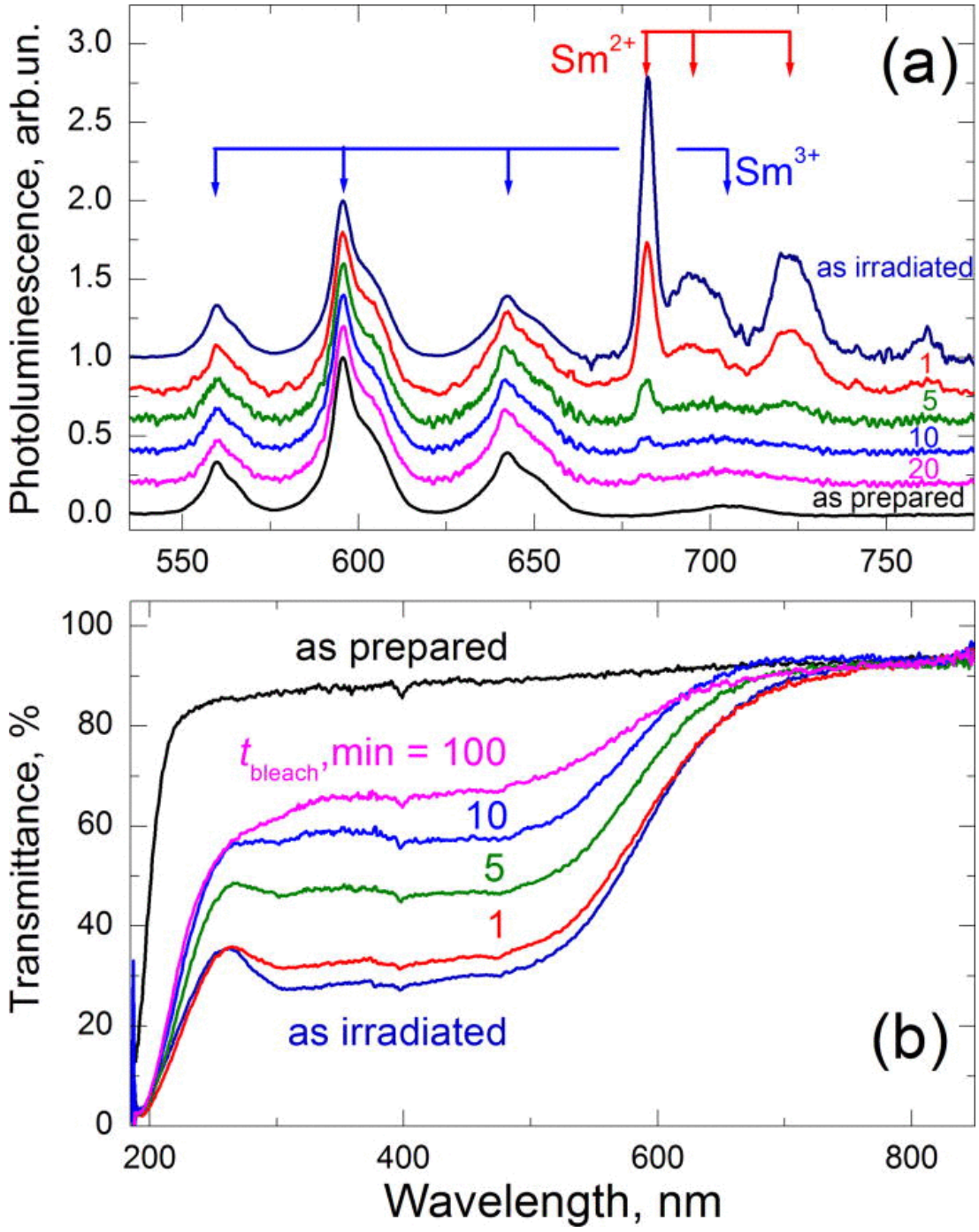

Figure 4.2 The effect of intense 405 nm illumination (erasure) on (a) the photoluminescence and (b) optical transmittance of FP10 glass doped with Sm^{3+}, and previously X-ray irradiated for 2 h (total dose delivered was ~14 kGy). The "as-prepared" trace was measured on the same glass prior to X-ray irradiation. "As irradiated" traces refer to the glass prior to any erasure. The times (durations) of erasure are values in minutes indicated above the corresponding curves. The spectra in (a) are shifted vertically to facilitate the comparison. The erasure illumination was at 405 nm (from an LED) with a power density of ~100 mW/cm ^{2}on the sample.

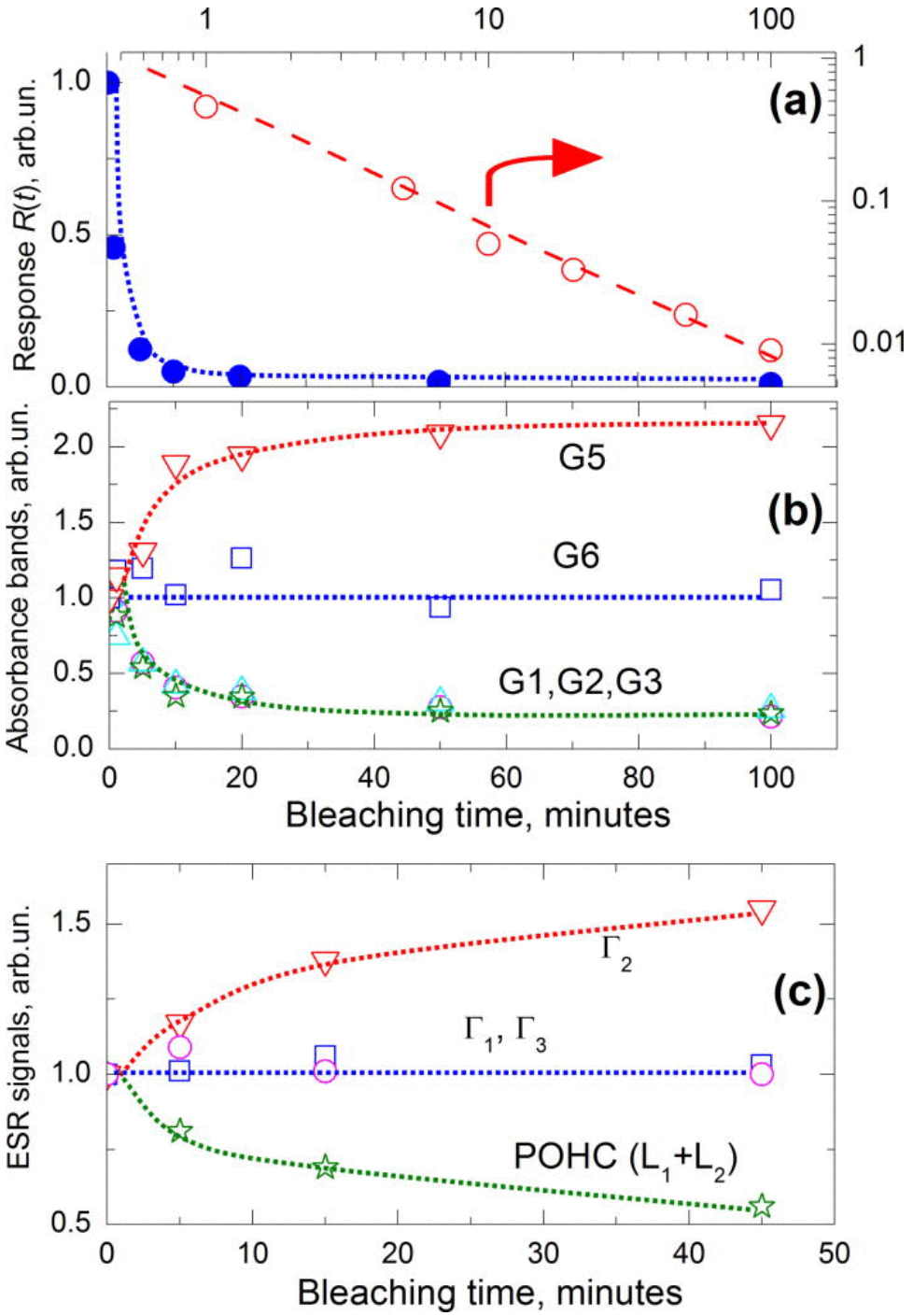

Figure 4.3 The effects of intense (~100 mW/cm^2 on the sample) 405 nm illumination (erasure) from an LED (a) on the response $R(t) = PL(Sm^{2+})/PL(Sm^{3+})$; (b)X-ray induced transmittance; (c) ESR signals in FP10 glasses doped with 0.5% of Sm^{3+} and previously X-ray irradiated for 2 h. All values are shown with respect to their initial values measured in "as irradiated" samples prior to any erasure. (a) Displays the PL twice: in linear and log-log scales. The labeling of Gaussians in (b) is done in accordance with Figure 4.5 and Table 4.1 . The labeling of ESR lines in (c) is done in accordance with Figure 4.6 and Table 4.2 . All lines are guides to the eye.

suggests the successful reconversion of Sm^{2+} back into Sm^{3+}. Figure 4.3(a) shows that the process of Sm^{2+} to Sm^{3+} reconversion is relatively fast and, at the given intensity within 50 min, optical illumination reduces the response by a factor of 100, which corresponds to a nearly full erasure.

Figure 4.4 addresses the issue of reproducibility of response $R(t)$ after erasure. Figure 4.4 compares the responses $R(t)$ before and after two consecutive cycles of optical erasure. The time of erasure was chosen intentionally short to avoid a complete recovery. It is worth noting that within a given dose range, $R(t)$ vs. dose behavior seems to be a linear function with a unique slope which is unaffected by erasure. This is a very promising result in that it appears as though optical erasure may be a convenient method of reconversion of Sm^{2+} to Sm^{3+}. However, further experiments, and deeper insight reveal some hidden potential obstacles connected with the creation and transformation of so-called "color centers."

It is widely known that changes of ion valency due to irradiation are usually accompanied by the formation of ESR and/or optically active defect centers [35-45]. The nature of these centers strongly depends on the nature of the glass itself. As an example, in germanium doped silica, they are usually associated with electrons trapped on germanium or/and silicon at the site of an oxygen vacancy [46-47]. Meanwhile, in heavy metal fluoride glasses, they are usually connected with the presence of neutral fluorine vacancies or interstitial atomic fluorine or impurities (e.g., oxygen) [48]. In fluorophosphate glasses of this work, these centers are commonly associated with holes and electrons captured by phosphorous-oxygen complexes [9-10,30,35,38].

Figure 4.2(b) shows the effect of X-ray irradiation and subsequent optical erasure on the optical transmittance. It can be clearly seen that the X-ray irradiation significantly reduces the transmittance, while the subsequent erasure partially restores the "status quo." However, even

after 100 min of erasure, one can still detect substantial induced absorption. Figure 4.5 reformulates this effect in terms of induced absorbance and presents a so-called *band separation analysis*, which allows us to quantify the processes of erasure. The technique of band separation presents the induced absorbance as a sum of Gaussians, which may be assigned to different electrons and hole centers [38,40,49].

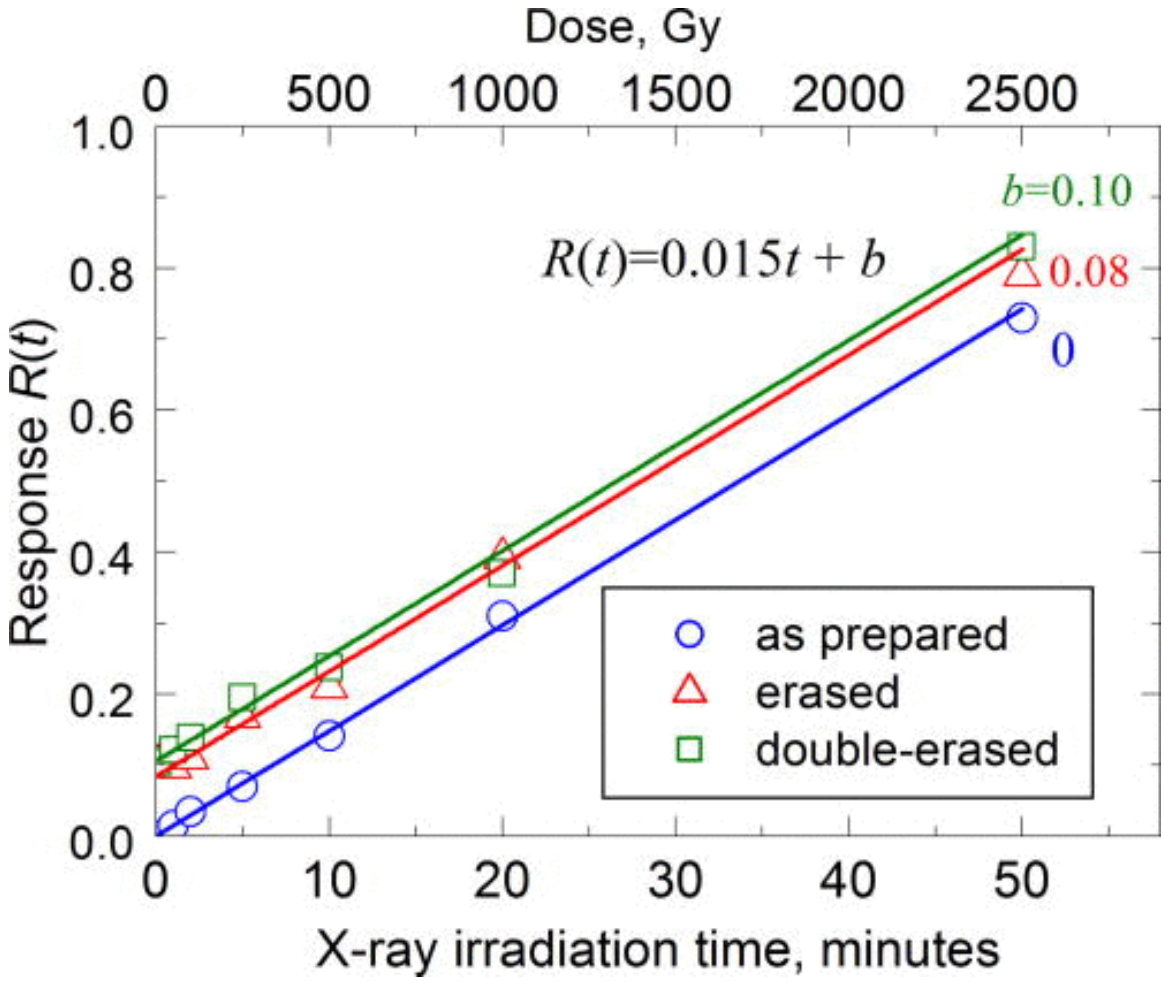

Figure 4.4 Response vs. dose behavior, and the influence of X-ray irradiation before and after two consecutive cycles of optical erasure. The values above the curves in the figure show adjustable parameters giving the best fit to experimental data. Notice that the slope of R (t) vs dose is the same in all three cases. (The erasure illumination was at 405 nm from an LED with a power density ~100 mW/cm^2 on the sample)

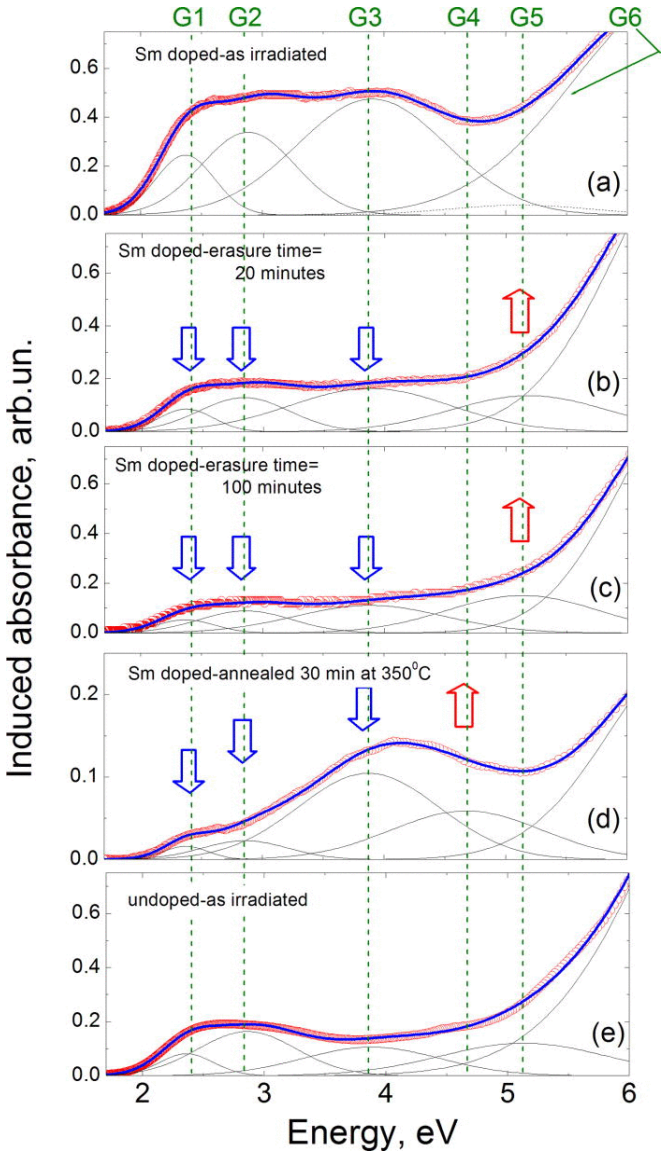

Figure 4.5 X-ray induced absorbance in FP10 glass doped with 0.5% of Sm^{3+} and initially X-ray irradiated for 2 h (total dose of ~14 kGy) (a)–(d) and nominally undoped FP10 glass irradiated for 30 min (e). Note that (a)–(c) show the evolution of X-ray induced absorbance under intense 405 nm illumination (erasure). (d) demonstrates the effect of annealing at 350 °C for 30 min. The experimental data (symbols) are approximated by a sum of Gaussians (thick solid lines). The individual Gaussians from G1 to G6 are shown by thin (solid and broken) lines. All Gaussians but G6 are marked at their centers. The center of G6 lies outside of the present figure. The broken line in (a) shows that the presence of the band G5 is not necessary prior to erasure in Sm-doped samples.

Figure 4.5 shows that in FP glasses, X-ray induced absorbance may be simulated using six overlapping Gaussians. The arrows in Figure 4.5(b)–(d) show the evolution of four of the

Gaussians under erasure, (b), (c); and annealing, (d). It should be noted that in our earlier work, we used only four Gaussians [9]. There is no contradiction here because the absorbance curve of "as-irradiated" sample alone may be fitted with the same level of accuracy using only four bands (this is shown by a dashed curve in Figure 4.5(a)). However, the absorbance curves collected during erasure require the additional band marked as G5. Furthermore, it should be emphasized that the band G5 appears also in a band separation analysis of absorbance in the undoped FP sample (with no Sm-doping) that had been just irradiated as shown in Figure 4.5(e). Meanwhile, the band G4 seems to appear only after thermal annealing as shown in Figure 4.5(d).

It seems appropriate to mention here that Sm-ions may also contribute to absorption within the 200–600 nm spectral range [50]. However, in our particular case, this contribution seems to be negligible. Indeed, Sm^{3+} is known to have a prominent absorption peak at 400 nm, which may be seen as a tiny feature (a very small dip at 400 nm) in the transmittance spectra in Figure 4.2(b). Similarly, Sm^{2+} has a peak absorption at around 360–380 nm [50], but this feature is again negligibly small. The contribution of absorbance from the excitation of Sm-ions has been therefore neglected in the analysis of the absorbance spectra and their evolution during irradiation and bleaching. The inclusion of absorption by Sm-ions does not change the analysis within the margins of error.

Table 4.1 compares our results of band separation with published data and shows a very reasonable agreement [38,40]. The only disagreement is the position of the band G6. The disagreement can be explained by the fact that the G6 band could only be captured partially in our experiments, being centered outside our spectroscopic range of measurement. In FP glasses, the absorption bands are usually associated with electron and hole capture within phosphorous-oxygen molecular ions or units [38,40]. Table 4.1 shows an example of such associations,

reproduced from papers published elsewhere [38,40]. Thus, the bands in the visible region (G1–G3) are associated with so-called POHC (phosphorous-oxygen hole centers), while the bands G4, G5, and G6 are supposedly related to PO_2, PO_4, and PO_3 electron centers (POEC), respectively [40]. Figure 4.3(b) shows the effect of optical illumination (erasure) on the intensities of the Gaussian G1–G6 bands. It shows that the erasure effectively reduces POHC related absorption bands G1–G3, while seemingly leaving the POEC related G6 band unchanged, and surprisingly increases the band G5, seemingly associated with POEC. This is a somewhat discouraging result, because it shows that although an intense optical illumination can successfully reconvert Sm^{2+} back to Sm^{3+}, it leads to the *appearance of new color centers* in the host glass. The new color centers, however, are in the UV range and thus do not prevent the recording of Sm^{3+} and Sm^{2+} PL signals.

Table 4.1 The comparison of central wavelengths (λ), central energies (*E*), and widths (*W*) of Gaussian absorption bands (G1–G6) observed in the present paper with earlier data by Ebeling *et al.* [40] The widths (*W*) of Gaussian bands refer to the full width at half maximum (FWHM).

Present paper				Ebeling *et al.*			
Bands	**λ, nm**	***E*, eV**	***W*, eV**	**λ, nm**	***E*, eV**	***W*, eV**	**Structural unit**
G1	525	2.36 ± 0.03	0.47	540	2.30 ± 0.02	0.50	POHC
G2	433	2.86 ± 0.02	0.74	430	2.89 ± 0.04	1.00	POHC
G3	320	3.88 ± 0.12	1.27	325	3.82 ± 0.04	1.12	POHC
G4	265	4.68 ± 0.09	1.10	265	4.68 ± 0.08	1.00	PO_2
G5	242	5.13 ± 0.02	1.22	240	5.12 ± 0.06	1.00	PO_4
G6	190	6.53 ± 0.08	1.47	210	5.90 ± 0.06	1.00	PO_3

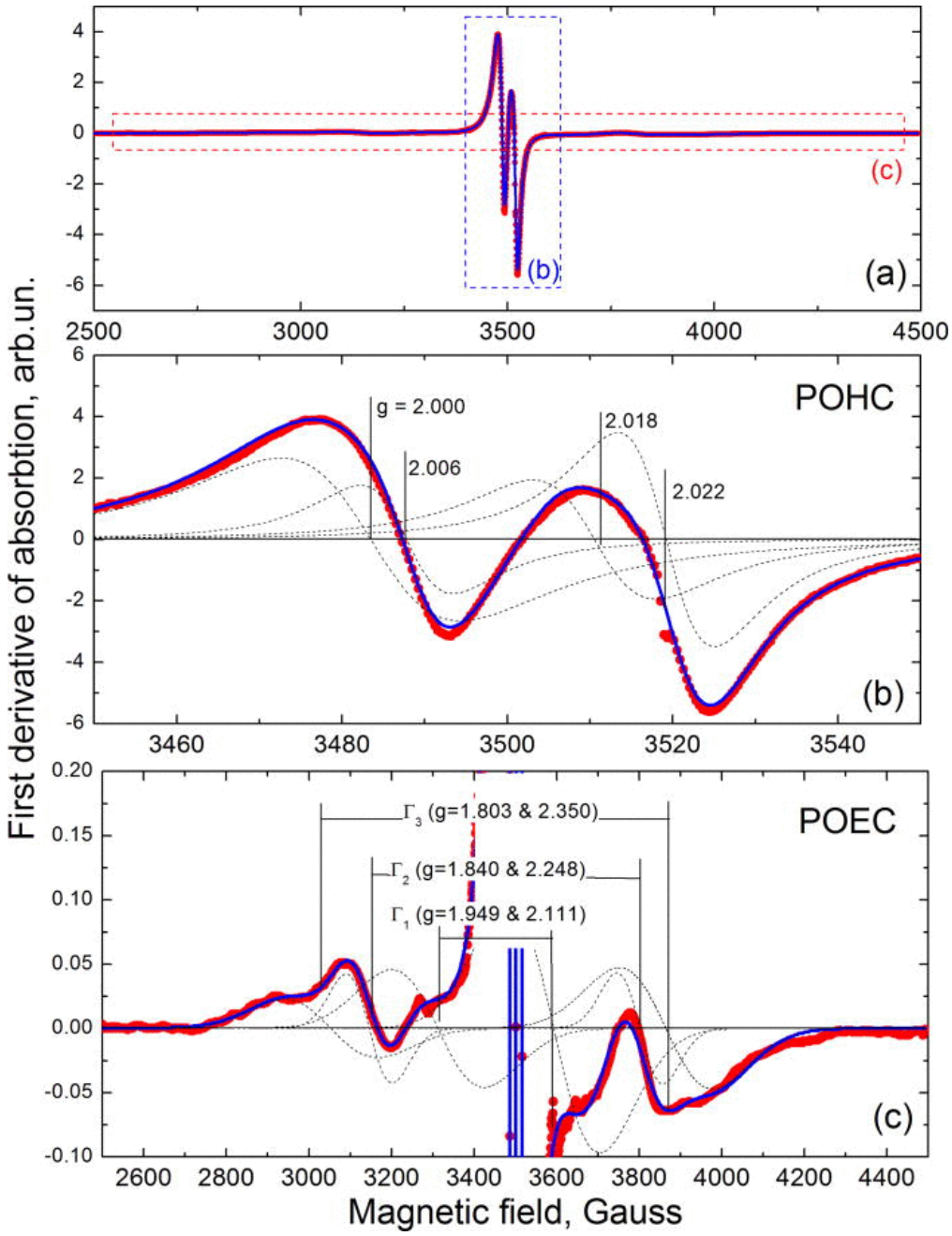

Figure 4.6 The ESR signal of FP10 glass doped with 0.5% of Sm^{3+} and X-ray irradiated for 2 h (total dose of ~6 kGy). (a) is an overview of a spectrum where the two rectangles (b) and (c) show the regions which are presented in (b) and (c), respectively. (b) shows strong and narrow lines in the central part of the spectrum, while (c) shows the weak wings of a spectrum. Experimental data (symbols) are approximated by a model (thick solid line) which is a sum of Lorentzians in (b) and Gaussians in (c), shown by thin broken lines. The Lorentzians in (b) are usually associated with phosphorous-oxygen hole centers (POHC), while the Gaussians in (c) represent three doublets (Γ_1-Γ_3) which are normally associated with POEC. The effective g-values shown in the figure correspond to the centers of corresponding Lorentzian and Gaussian components.

Figure 4.6(a)–(c) present the ESR signal from our FP10 glass doped with 0.5% of Sm^{3+} and X-ray irradiated for 2h. It is appropriate to emphasize here that there was no detectable ESR signal prior to irradiation, and the ESR signal appeared only after X-ray irradiation. For the following interpretation, the experimental data have been approximated by a sum of the first derivatives of four Lorentzians (shown in Figure 4.6(b)) and six Gaussians (shown in Figure 4.6 (a) and Figure 4.6 (c)). We assume that these ten individual lines belong to five doublets whose spin-Hamiltonian parameters are summarized in Table 4.2 . The identification or association of ESR lines was reported previously by Ebeling *et al.* [40] The comparison of present data with the results by Ebeling *et al.* [40] allows us to identify the doublets L_1 and L_2 as belonging to POHC, while the doublets Γ_1, Γ_2, and Γ_3 may be tentatively associated with PO_2, PO_3, and PO_4 complexes, respectively. Figure 4.3(c) summarizes the influence of optical erasure on the ESR components. It shows that POHC related Lorentzian doublets L_1 and L_2 decrease with erasure, while the POEC related Gaussian doublet Γ_2 increases and Gaussian doublets Γ_1 and Γ_3, also related to POEC, remain seemingly unaffected. Overall, based on the ESR data, the effects of erasure are the same as those based on the band separation analysis above; in other words, optical erasure seems to reduce the POHC while inducing some additional POEC. Note that the lines in Table 4.2 were used for all ESR spectra that were recorded after each step of bleaching, and only the intensities of the lines change with erasure time (see Figure 4.3 (c)).

From a chemical point of view, we can summarize the effect of optical erasure by a set of chemical reactions in which *hv* represents optical excitation

$$Sm^{2+} + h\nu \rightarrow Sm^{3+} + e^{-} \qquad (4.1)$$

$$POHC + e^{-} \rightarrow PO \qquad (4.2)$$

$$PO + e^{-} \rightarrow POEC \qquad (4.3)$$

where e^{-} stands for an electron released by Sm^{2+} under optical illumination, PO represents a phosphorus-oxygen based defect precursor, and POHC (POEC) stands for a phosphorus-oxygen center with a captured hole (captured electron for POEC). In other words, Sm^{2+} ions become optically excited and relax to Sm^{3+} with the emission of electrons which are captured by PO precursors, producing POEC with an outcome that depends on the nature of precursor and/or by POHC reconverting to PO groups. We should also emphasize that the above three sets of equations represent an oversimplification of the optical erasure process, because the optical illumination itself may erase and create several types of POHC and POEC.

Table 4.2 The lines used for approximating the ESR signals of FP10 glass doped with 0.5% of Sm^{3+} and X-ray irradiated for 2 h. The total dose delivered is ~6 kGy. Three doublets have Gaussian (Γ) and two have Lorentzian (L) lineshapes. $g^{(1)}$ and $g^{(2)}$ are the effective *g*-values for each line of a doublet. g_{average} is the average of $g^{(1)}$ and $g^{(2)}$. *A* is a splitting of two lines of a doublet. *W* is the full width of each line at half maximum. *W* and *A* are defined for a nominal frequency of 9.8 GHz. Possible interpretation of structures related to appropriate doublet is based on comparison with Ebeling *et al.* [40].

Doublets	**Γ_1**	**Γ_2**	**Γ_3**	**L_1**	**L_2**
g_{average}	2.030	2.044	2.076	2.014	2.009
A, Gauss	276	695	908	28	31
W, Gauss	251	123	173	28	21
$g^{(1)}$	2.111	2.248	2.350	2.022	2.018
$g^{(2)}$	1.949	1.840	1.803	2.006	2.000
Nature	POEC	POEC	POEC	POHC	POHC

Applying the same rationale to the effect of X-ray irradiation, we can write another set of chemical reactions of the form

$$\mathrm{PO} + h^{+} \rightarrow \mathrm{POHC} \qquad (4.4)$$

$$\mathrm{Sm}^{3+} + e^{-} \rightarrow \mathrm{Sm}^{2+} \qquad (4.5)$$

$$\mathrm{PO} + e^{-} \rightarrow \mathrm{POEC} \qquad (4.6)$$

where e^{-} and h^{+} stand for electrons and holes generated under X-ray irradiation. In the case of X-ray irradiation, the absorbed X-ray ejects a primary projectile electron, from an inner shell, that ionizes the medium and generates electrons and holes. Equation (4.6) is a new addition to our previous approach [9-10]. It is worth noting that Eqs. (4.3) and (4.6) are identical, which means that certain types of POEC may appear under different types of excitation, in particular, X-ray irradiation and/or optical erasure.

Naturally, Eqs. (4.1)–(4.3) and (4.4)–(4.6) should be supplemented by a charge conservation condition that can be written as

$$C_{\mathrm{POHC}}(t) = C_{\mathrm{Sm}^{2+}}(t) + C_{\mathrm{POEC}}(t) \qquad (4.7)$$

where $C_{\mathrm{POHC}}(t)$, $C_{\mathrm{Sm}^{2+}}(t)$, and $C_{\mathrm{POEC}}(t)$ are the concentrations of the species POHC, Sm^{2+}, and POEC, respectively, at any given instant of time t. The above equations clearly show that under X-ray irradiation, the electrons are shared between two competing processes: Sm^{3+} to Sm^{2+} conversion and POEC formation.

We still need to answer the question, "What is the maximum Sm^{3+} concentration for a good conversion efficiency?" Figure 4.7 tries to answer this question. It shows the response R as a function of concentration of trivalent samarium $C_{\mathrm{Sm}^{3+}}$ for several X-ray doses (D) corresponding to different irradiation times. The response is plotted as a function of D and $C_{\mathrm{Sm}^{3+}}$. Figure

4.7 shows that there are two distinctive regions in the R (D, C_{Sm}^{3+}) vs. C_{Sm}^{3+} dependence. At low concentrations, R (D, C_{Sm}^{3+}) ≈ const (D), which depends on the dose D. At higher concentrations, R (D, C_{Sm}^{3+}) seems to be inversely proportional to C_{Sm}^{3+}, i.e., R (D, C_{Sm}^{3+}) ∝ $(C_{Sm}^{3+})^{-1}$. For further interpretation, it seems reasonable to assume that the relative intensity of the PL is approximately proportional to the ratio of the ionic concentrations, i.e., R (D, C_{Sm}^{3+}) ∝ C_{Sm}^{2+} (D) / C_{Sm}^{3+}, where the constant of proportionality, among other factors, would include the optical oscillator strengths of the PL transitions in Sm^{3+} and Sm^{2+}. Therefore, R (D, C_{Sm}^{3+}) ≈ const (D) means simply that C_{Sm}^{2+} (D) ∝ C_{Sm}^{3+}. In other words, the more Sm^{3+} we add, the more Sm^{2+} conversion takes place within a given irradiation time, that is, at a given dose rate. Meanwhile, R (D, C_{Sm}^{3+}) ∝ $(C_{Sm}^{3+})^{-1}$ should be interpreted as C_{Sm}^{2+} (D) ≈ const (D). The latter constant depends only on the dose D and does not depend on C_{Sm}^{3+}. From a practical view, this result means that the addition of Sm^{3+} over a critical concentration, C_{crit} (Sm^{3+}), does not create additional converted Sm^{2+}, and further doping may be considered ineffectual.

The above observation may be explained by the concentration quenching effect, which typically starts to set in at around the concentration where the graph in Figure 4.7 has a "knee" (begins rolling off), i.e., 0.5–5%, where one rare earth ion has a good chance of being sufficiently close to another rare earth ion to be able to affect the radiative transition. This effect would be dose independent, as observed. We would expect that for "high" concentrations of Sm^{3+}, the Sm^{2+} could relax from its excited states through a Forster-Dexter type mechanism [51], giving its energy to a nearby Sm^{3+}, assisted by the overlap between a broad 5*d* band and the sharp 4*f* lines. This would certainly reduce the PL intensity ratio for Sm^{2+}/Sm^{3+} through both the numerator and denominator. Alternatively, the luminescence saturation effect may be connected with the host glass itself where the number of sites for Sm^{3+} to Sm^{2+} conversion may

be limited by the organization of the host glass ionic network. In any case, further experiments are needed to shed light on the possible origins of "the concentration quenching" effect.

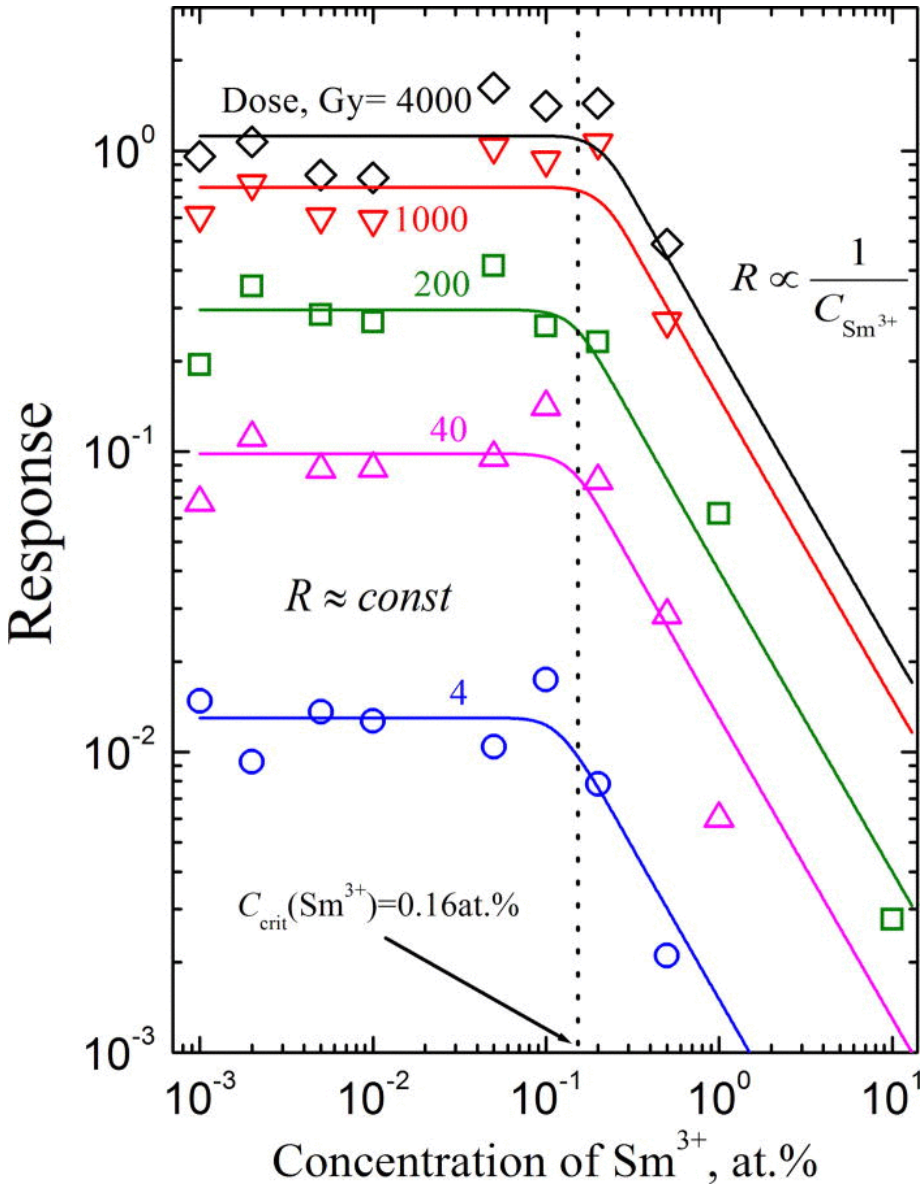

Figure 4.7 Response $R = PL(Sm^{2+})/PL(Sm^{3+})$ of FP 10 glass at different delivered doses versus doping (Sm^{3+}) concentration. The PL excitation wavelength was 470 nm.

4.5 Conclusion

X-ray induced Sm^{3+} to Sm^{2+} valence conversion in Sm^{3+}-doped FP glasses, and subsequent reconversion of Sm^{2+} to Sm^{3+}under intense optical illumination, has been investigated for

potential use in a re-useable dosimetric detector for MRT. It was shown that X-ray irradiated Sm-doped FP glasses can be optically erased by illumination under 405 nm light so that they can be reused in measuring the dose in microbeam radiation therapy. The Sm^{3+} to Sm^{2+} valence conversion is accompanied by the formation of POHC and POEC responsible for X-ray induced optical absorbance. The use of intense optical illumination seemingly achieves near-complete Sm^{2+} to Sm^{3+} reconversion. However, the examination of optical transmission spectra shows that optical illumination only partially erases existing X-ray induced bands, and, at the same time, induces new absorbance bands. We have used a band-separation analysis to interpret the induced absorbance, based on reported possible defect structures in the literature. Combined analysis of absorbance and ESR measurements indicates the optically stimulated erasure of POHC related defects and the development of new POEC related defects. The suggested model for the observed phenomena is based on the release of electrons during Sm^{2+} to Sm^{3+} reconversion, the capture of these electrons by POHC (and hence their disappearance) or by PO groups (with the appearance of additional EC defects). The latter conclusion shows that the direct X-ray induced Sm^{3+} to Sm^{2+} conversion seems to be directly competing with POEC formation. The conversion ratio (the response of the detector) does not depend on the initial concentration of Sm^{3+} in the glass up to a certain critical concentration $C_{crit}(Sm^{3+}) \approx 0.16$ at. %. Beyond this critical concentration, it monotonically decreases with the Sm^{3+} concentration. The latter observation may be connected with the concentration quenching effect, which usually occurs at similar concentrations or with the host glass itself where the number of possible sites for the Sm^{3+} to Sm^{2+} conversion may be limited by the organization of the host glass ionic network.

Acknowledgments

We thank NSERC and the New Zealand Ministry of Business, Innovation and Employment for financial support and Teledyne-DALSA for sponsoring the project through NSERC. (Irradiation experiments described in this paper were performed at the Canadian Light Source, which is supported by NSERC, NRC, the Canadian Institutes of Health Research, the Province of Saskatchewan, Western Economic Diversification, Canada, and the University of Saskatchewan.)

4.6 References

1. K. Miura, J. Qiu, S. Fujiwara, S. Sakaguchi, and K. Hirao, "Three-dimensional optical memory with rewriteable and ultrahigh density using the valence-state change of samarium ions," Appl. Phys. Lett. **80**, 2263 (2002).

2. J. Lim, M. Lee, and E. Kim, "Three-dimensional optical memory using photoluminescence change in Sm-doped sodium borate glass," Appl. Phys. Lett. **86**, 191105 (2005).

3. A. Z. M. S. Rahman, X. Cao, L. Wei, B. Wang, R. Yu, Z. Chen, G. An, and A. Sidike, "Irradiation-induced valence conversion of samarium ions in Na2SO4," Appl. Phys. A **111**, 587 (2013).

4. E. Malchukova, B. Boizot, G. Petite, and D. Ghaleb, "Optical properties and valence state of Sm ions in aluminoborosilicate glass under β-irradiation," J. Non-Cryst. Solids **353**, 2397 (2007).

5. Y. Huang, C. Jiang, K. Jang, H. Sueb, E. Cho, M. Jayasimhadri, and S.-S. Yi, "Luminescence and microstructure of Sm^{2+} ions reduced by X-ray irradiation in $Li_2O–SrO–B_2O_3$ glass," J. Appl. Phys. **103**, 113519 (2008).

6. C. A. G. Kalnins, H. Ebendorff-Heidepriem, N. A. Spooner, and T. M. Monro, "Optically stimulated luminescence in fluoride–phosphate glass for radiation dosimetry," J. Am. Ceram. Soc. **94**, 474–477 (2011).

7. C. Paβlick, O. Muller, D. Lutzenkirchen-Hecht, R. Frahm, J. A. Johnson, and S. Schweizer, "Optically Stimulated Luminescence in Fluoride–Phosphate Glass for Radiation Dosimetry," J. Appl. Phys. **110**, 113527 (2011) and references therein, as an example.

8. B. Henke, C. Paβlick, P. Keil, J. A. Johnson, and S. Schweizer, "Eu oxidation state in fluorozirconate-based glass ceramics," J. Appl. Phys. **106**, 113501 (2009).

9. G. Okada, B. Morrell, C. Koughia, A. Edgar, C. Varoy, G. Belev, T. Wysokinski, D. Chapman, and S. Kasap, "Spatially resolved measurement of high doses in microbeam radiation therapy using samarium doped fluorophosphate glasses," Appl. Phys. Lett. **99**, 121105 (2011).

10. S. Vahedi, G. Okada, B. Morrell, E. Muzar, C. Koughia, A. Edgar, C. Varoy, G. Belev, T. Wysokinski, D. Chapman, and S. Kasap, "X-ray induced Sm^{3+} to Sm^{2+} conversion in fluorophosphate and fluoroaluminate glasses for the monitoring of high-doses in microbeam radiation therapy," J. Appl. Phys. **112**, 073108 (2012).

11. D. N. Slatkin, F. A. Dilmanian, P. Spanne, and M. Sandborg, "Microbeam radiation therapy: Tissue dose penetration and BANG-gel dosimetry of thick-beams' array interlacing," Med. Phys. **19**, 1395 (1992).

12. F. A. Dilmanian, P. Romanelli, Z. Zhonge, R. Wang, M. E. Wagshul, J. Kalef-Ezra, M. J. Maryanski, E. M. Rosen, and D. J. Anschel, "Microbeam radiation therapy: Tissue dose penetration and BANG-gel dosimetry of thick-beams' array interlacing," Eur. J. Radiol. **68**, S129 (2008).

13. P. Deman, M. Vautrin, M. Edouard, V. Stupar, L. Bobyk, R. Farion, H. Elleaume, C. Remy, E. L. Barbier, F. Esteve, and J.-F. Adam, "Monochromatic minibeams radiotherapy: From healthy tissue-sparing effect studies toward first experimental glioma bearing rats therapy," Int. J. Radiat. Oncol., Biol., Phys. **82**, e693 (2012).

14. A. Bouchet, A. Boumendjel, E. Khalil, R. Serduc, E. Brauer, E. A. Siegbahn, J. A. Laissueg, and J. Boutonnath, "Chalcone JAI-51 improves efficacy of synchrotron microbeam radiation therapy of brain tumors," J. Synchrotron Radiat. **19**, 478 (2012).

15. E. Brauer-Krisch, R. Serduc, E. A. Siegbahn, G. Le Duc, Y. Prezado, A. Bravin, H. Blattmann, and J. A. Laissue, "Effects of pulsed, spatially fractionated, microscopic synchrotron X-ray beams on normal and tumoral brain tissue," Mutat. Res. **704**, 160 (2010).

16. J. C. Crosbie, R. L. Anderson, K. Rothkamm, C. M. Restall, L. Cann, S. Ruwanpura, S. Meachem, N. Yagi, I. Svalbe, R. A. Lewis, B. R. G. Williams, and P. A. W. Rogers, "Tumor cell response to synchrotron microbeam radiation therapy differs markedly from cells in normal tissues," Int. J. Radiat. Oncol., Biol., Phys. **77**, 886 (2010).

17. M. Torikoshi, Y. Ohno, N. Yagi, K. Umetani, and Y. Furusawa, "Dosimetry for a microbeam array generated by synchrotron radiation at SPring-8," Eur. J. Radiol. **68**, S114 (2008).

18. E. Bräuer-Krisch, H. Requardt, T. Brochard, G. Berruyer, M. Renier, J. A. Laissue, and A. Bravin, "New technology enables high precision multislit collimators for microbeam radiation therapy," Rev. Sci. Instrum. **80**, 074301 (2009).

19. E. Bräuer-Krisch, A. Rosenfeld, M. Lerch, M. Petasecca, M. Akselrod, J. Sykora, J. Bartz, M. Ptaszkiewicz, P. Olko, A. Berg, M. Wieland, S. Doran, T. Brochard, A. Kamlowski, G. Cellere, A. Paccagnella, E. A. Siegbahn, Y. Prezado, I. Martinez-Rovira, A. Bravin, L. Dusseau,

and P. Berkvens, “Potential High Resolution Dosimeters For MRT,” AIP Conf. Proc. **1266**, 89 (2010).

20. K. Rothkamm, J. C. Crosbie, F. Daley, S. Bourne, P. R. Barber, B. Vojnovic, L. Cann, and P. A. W. Rogers, “In situ biological dose mapping estimates the radiation burden delivered to ‘spared’ tissue between synchrotron X-ray microbeam radiotherapy tracks,” PLoS One **7**(1), e29853 (2012).

21. J. A. Bartz, G. J. Sykora, E. Bräuer-Krisch, and M. S. Akselrod, “Imaging and dosimetry of synchrotron microbeam with aluminum oxide fluorescent detectors,” Radiat. Meas. **46**, 1936 (2011).

22. T. Ackerly, J. C. Crosbie, A. Fouras, G. J. Sheard, S. Higgins, and R. A. Lewise, “High resolution optical calorimetry for synchrotron microbeam radiation therapy,” J. Instrum. **6**, P03003 (2011).

23. D. Maki, T. Ishii, F. Sato, Y. Kato, T. Yamamoto, and T. Iida, “Development of confocal laser microscope system for examination of microscopic characteristics of radiophotoluminescence glass dosemeters,” Radiat. Prot. Dosim. **144**, 222 (2011).

24. A. T. AbdulRahman, D. A. Bradley, S. J. Doran, B. Thierry, E. Bräuer-Krisch, and A. Bravin, “The thermoluminescence response of Ge-doped silica fibres for synchrotron microbeam radiation therapy dosimetry,” Nucl. Instrum. Methods Phys. Res., Sect. A **619**, 167 (2010).

25. M. Petasecca, A. Cullen, I. Fuduli, A. Espinoza, C. Porumb, C. Stanton, A. H. Aldosari, E. Bräuer-Krisch, H. Requardt, A. Bravin, V. Perevertaylo, A. B. Rosenfeld, and M. L. F. Lerch, “X-Tream: a novel dosimetry system for Synchrotron Microbeam Radiation Therapy,” J. Instrum. **7**, P07022 (2012).

26. N. Nariyama, T. Ohigashi, K. Umetani, K. Shinohara, H. Tanaka, A. Maruhashi, G. Kashino, A. Kurihara, T. Kondob, M. Fukumoto, and K. Ono, “Spectromicroscopic film dosimetry for high-energy microbeam from synchrotron radiation,” Appl. Radiat. Isot. **67**, 155 (2009).

27. G. Belev, G. Okada, D. Tonchev, C. Koughia, C. Varoy, A. Edgar, T. Wysokinski, D. Chapman, and S. Kasap, “Valency conversion of samarium ions under high dose synchrotron generated X-ray radiation,” Phys. Status Solidi C **8**, 2822 (2011).

28. Y. Tian, R. Xu, L. Hu, and J. Zhang, “Fluorescence properties and energy transfer study of Er^{3+}/Nd^{3+} doped fluorophosphate glass pumped at 800 and 980 nm for mid-infrared laser applications,” J. Appl. Phys. **111**, 073503 (2012).

29. L. Zhang, Z. Yang, Y. Tian, J. Zhang, and L. Hu, “Comparative investigation on the 2.7 μm emission in Er^{3+}/Ho^{3+} codoped fluorophosphate glass,” J. Appl. Phys. **110**, 093106 (2011).

30. H. Ebendorff-Heidepriem and D. Ehrt, “Effect of Tb^{3+} ions on X-ray-induced defect formation in phosphate containing glasses,” Opt. Mater. **18**, 419 (2002).

31. V. Venkatramu, P. Babu, C. K. Jayasankar, Th. Troster, W. Sievers, and G. Wortmann, "Optical spectroscopy of Sm^{3+} ions in phosphate and fluorophosphate glasses,"Opt. Mater. **29**, 1429 (2007).

32. C. R. Kesavulu and C. K. Jayasankar, "Spectroscopic properties of Sm^{3+} ions in lead fluorophosphate glasses," J. Lumin. **132**, 2802 (2012).

33. A. Edgar, C. R. Varoy, C. Koughia, G. Okada, G. Belev, and S. Kasap, "High-resolution X-ray imaging with samarium-doped fluoroaluminate and fluorophosphate glass," J. Non-Cryst. Solids **377**, 124 (2013).

34. G. Okada, S. Vahedi, B. Morrell, C. Koughia, G. Belev, T. Wysokinski, D. Chapman, C. Varoy, A. Edgar, and S. Kasap, "Examination of the dynamic range of Sm-doped glasses for high-dose and high-resolution dosimetric applications in microbeam radiation therapy at the Canadian synchrotron," Opt. Mater. **35**, 1976 (2013).

35. D. L. Griscom, E. J. Friebele, K. J. Long, and J. W. Fleming, "Fundamental defect centers in glass: Electron spin resonance and optical absorption studies of irradiated phosphorus-doped silica glass and optical fibers," J. Appl. Phys. **54**, 3743 (1983).

36. L. D. Bogomolova, Yu. G. Teplyakov, V. A. Jachkin, V. L. Bogdanov, V. D. Khalilev, F. Caccavale, and S. Lo Russo, "On the formation of paramagnetic defects in ion-implanted fluoroaluminate glasses," J. Non-Cryst. Solids **202**, 178 (1996).

37. T. V. Bocharova, G. O. Karapetyan, A. M. Mironov, N. M. Mishchenkov, and N. O. Tagil'tseva, "Irradiation-induced and postirradiation processes in fluoroaluminate glasses," Inorg. Mater. **42**(6), 671–680 (2006).

38. D. Ehrt, P. Ebeling, and U. Natura, "UV Transmission and radiation-induced defects in phosphate and fluoride–phosphate glasses," J. Non-Cryst. Solids **263–264**, 240–250 (2000).

39. K. Tanimura, W. A. Sibley, M. Suscavage, and M. Drexhage, "Radiation effects in fluoride glasses," J. Appl. Phys. **58**, 4544 (1985).

40. P. Ebeling, D. Ehrt, and M. Friedrich, "X-ray induced effects in phosphate glasses," Opt. Mater. **20**, 101 (2002).

41. J. Qiu, Y. Shimizugawa, Y. Iwabuchi, and K. Hirao, "Photostimulated luminescence in Eu^{2+}-doped fluoroaluminate glasses," Appl. Phys. Lett. **71**, 759 (1997).

42. N. Ollier, B. Boizot, P. L'henoret, S. Guillous, and G. Petite, "Evidence of transient species occurring in the reduction process of trivalent lanthanides under 2.5 MeV electron irradiation by in situ cathodoluminescence and time-resolved photoluminescence," J. Appl. Phys. **105**, 113515 (2009).

43. T. V. Bocharova, G. O. Karapetyan, A. M. Mironov, N. O. Tagil'tseva, and V. D. Khalilev, "Specific Features of the Induced Absorption Spectra of Fluoroaluminate Glasses Doped with Samarium Ions," Glass Phys. Chem. **29**, 7 (2003).

44. L. Yang, N. Da, D. Chen, Q. Zhao, X. Jiang, C. Zhu, and J. Qiu, "Valence state change and refractive index change induced by femtosecond laser irradiation in Sm^{3+} doped fluoroaluminate glass," J. Non-Cryst. Solids **354**, 1353 (2008).

45. J. Qiu, K. Nouchi, K. Miura, T. Mitsuyu, and K. Hirao, "Room-temperature persistent spectral hole burning of X-ray-irradiated Sm^{3+}-doped glass," J. Phys.: Condens. Matter **12**, 5061 (2000).

46. E. J. Friebele, D. L. Griscom, and G. H. Sigel, Jr., "Defect centers in a germanium-doped silica-core optical fiber," J. Appl. Phys. **45**, 3424 (1974).

47. J. X. Wen, W. Y. Luo, Z. Y. Xiao, T. Y. Wang, Z. Y. Chen, and X. L. Zeng, "Formation and conversion of defect centers in low water peak single mode optical fiber induced by gamma rays irradiation," *J. Appl. Phys.* **107**, 044904 (2010).

48. D. L. Griscom, "Defect centers in heavy-metal fluoride glasses: a review," J. Non-Cryst. Solids **161**, 45 (1993).

49. P. W. Levy, "The Kinetics of Gamma-Ray Induced Coloring of Glass," J. Am. Ceram. Soc. **43**, 389 (1960).

50. A. Edgar, C. R. Varoy, C. Koughia, D. Tonchev, G. Belev, G. Okada, S. O. Kasap, H. von Seggern, and M. Ryan, "Erratum to "Optical properties of divalent samarium-doped fluorochlorozirconate glasses and glass ceramics" [Opt. Mater. 31 (2009) 1459–1466]," Opt. Mater. **32**, 266 (2009).

51. G. Blasse and B. C. Grabmaier, ed. *Luminescent Materials,* (Springer-Verlag, Berlin, New York, 1994), Chap. 5, pp. 90–107.

5 ESR Study of Samarium Doped Fluorophosphate Glasses for High-Dose, High-Resolution Dosimetry

Published as:

Shahrzad Vahedi, Go Okada, Cyril Koughia, Ramaswami Sammynaiken, Andy Edgar, and Safa Kasap, "ESR study of samarium doped fluorophosphate glasses for high-dose, high-resolution dosimetry", *Optical Materials Express,* Vol. 4, Issue 6, pp. 1244-1256, May 2014.

Author contributions:

The main experimental work and data analysis of this manuscript was performed by Shahrzad Vahedi. Go Okada helped in preparing the glass samples. Shahrzad Vahedi prepared the manuscript. Cyril Koughia and Safa Kasap contributed to editing the manuscript. Ramaswami Sammynaiken provided the technical support for using the ESR instrument. Andy Edgar synthesized the glasses and offered comments and suggestions for improving the manuscript.

5.1 Abstract

We have studied the effect of samarium doping concentration and thermal annealing on X-ray induced defect centers, including phosphorus-oxygen hole and electron centers (POHC and POEC), in Sm^{3+}-doped fluorophosphate glasses towards developing a potential high-dose, high-resolution detector for microbeam radiation therapy. ESR measurements show that defect center formation is suppressed by increasing the Sm-dopant concentration with POECs more strongly influenced than POHCs. This can be explained by a model based on the competition between defect center formations and $Sm^{3+} \leftrightarrows Sm^{2+}$ interconversion. Thermal annealing at increasing moderate temperatures (T_A = 100−300 °C) reduces the POHC related ESR and induced absorbance bands while those of POEC continue to survive. ESR measurements over a wider range show the trace of a very broad ESR signal in samples containing Sm^{2+} ions including those

annealed at temperatures between 350°C and glass transition temperature ($T_g \approx 460$ °C). Finally, thermal annealing at 550°C ($> T_g$) totally erases all the ESR signals and restores the sample to its original unirradiated state.

5.2 Introduction

There has been much interest in samarium (Sm) and europium (Eu) doped glasses due to their efficient luminescence and their persistent spectral hole burning characteristics [1–6]. These ions are most stable in their trivalent state in glasses that have been prepared by conventional glass melting techniques. However, it is well known that, in many host glasses, the trivalent Sm^{3+} and Eu^{3+} ions can be converted to their divalent form (Sm^{2+} and Eu^{2+}) upon exposure to high energy radiation. This valence change can be optically detected because the dominant emission bands of trivalent and divalent forms of Sm and Eu can be readily distinguished [7,8]. In the case of Sm, all dominant bands of Sm^{3+} and Sm^{2+} ions are situated in the red region of the spectrum, which means that there is a good match to silicon based detectors used in optical measurements. The valency conversion of these ions has been reported in phosphate, borate and aluminate containing glasses under X-ray, fs-laser, γ and β-irradiation [5,6,8–20]. This conversion is usually accompanied by the formation of defects in the glass which include electron centers and hole centers. Electronic transitions of these defects cause high absorbances in the UV and the visible regions, which results in photodarkening of the glass. As defect centers are paramagnetic, electron spin resonance (ESR) can be used to investigate the nature of these defects. It should be stressed here that the valency conversion has been usually observed in glasses which are host to "oxygen-associated trapped hole centers [21]" such as POHC [22–25], BOHC [8,17,26] or (Al-OHC) [6,20,27,28]. Valency conversion is usually reversible. It has been reported that optical-illumination [26,29,30] as well as annealing the glass at high temperatures [6,29,31] may result

in the reverse conversion of divalent to trivalent ions. The photodarkening is usually reversible as well. Annealing or illuminating the sample may reduce the X-ray induced absorption, probably by removing color centres [10,11,28,31–34].

Recently, we demonstrated that the X-ray irradiation induced valency conversion of Sm^{3+}-ions in glasses can be a promising dosimetric technique for the measurement of spatially resolved high doses in Microbeam Radiation Therapy (MRT) [30,31,35]. MRT is an experimental form of radiation treatment which guarantees less damage to normal tissue in comparison with other kinds of radiotherapy. This is based on the markedly different responses of tumor and normal cells to this form of treatment. The synchrotron generated X-ray beam is collimated and applied in the form of an array of planar microbeams (typically~20–50 μm width) usually spaced 100–400 μm apart. As a result, the spatial dose distribution has high dose and low dose areas that alternate. While the 'peak dose' (~150–600 Gy) provides lethal radiation for damaging tumors, the 'valley dose' (~3–30 Gy) spares sufficient minimally irradiated normal tissue, including the central nervous system which has extraordinary resistance to damage. This tissue is capable of repairing the irradiation damaged zones. The exact mechanisms underlying this effect are not well understood. It is suggested that the surviving blood vessels in the valley zones repair the tissue microvasculature through an angiogenesis process; spared tumor tissue on the other hand would be ablated (as suggested) by the migration of lethally irradiated tumor cells to 'valley zones'. Accordingly, the accurate measurement of peak-to-valley dose ratio (PVDR) is of crucial importance to assure that inadequate normal tissue is maintained [36–41]. However, the accurate, simultaneous recording of peak and valley doses that differ by hundreds of Grays, and the large dose gradients (hundreds of Grays over several microns) in the whole X-ray energy range of interest for MRT (50-250 keV) is an extremely challenging task. No current detector

can satisfactorily meet all these requirements [42], and intensive research towards the development of detectors suitable for MRT is currently underway [43–49].

In our earlier work, we examined various Sm^{3+} doped glasses for the presence of $Sm^{3+} \rightarrow Sm^{2+}$ conversion under the influence of X-ray irradiation for the purposes of developing high-dose high-resolution detector plates suitable for MRT. Among a large variety of glasses we had examined, we found useful Sm^{3+} to Sm^{2+} conversion only in fluoroaluminate (FA) and fluorophosphate (FP) glasses [30,31,35,50]. We showed that both types may be used in the measurement of high-dose to several thousand Grays and provide high spatial resolution required for MRT. The detection is based on the X-ray induced conversion of trivalent Sm^{3+} to the divalent form Sm^{2+}. Photoluminescence (PL) spectra of Sm^{2+} ions can be easily distinguished from those of Sm^{3+} ions and hence we can measure the dose which is proportional to response ratio $R(t) = PL(Sm^{2+})/PL(Sm^{3+})$. A side effect of X-ray irradiation is the formation of defect centers and photodarkening of these glasses. In our case, photodarkening is an undesirable effect and makes the calculation of the response ratio complicated as discussed in our previous work [31]. We also showed that the effects of previous X-ray exposure, including the valency conversion of Sm ions, along with photodarkening may be erased by intense optical illumination [30] or annealing at temperatures sufficiently exceeding the glass transition temperature T_g. Annealing at temperatures around or just below T_g results in the stabilization of the Sm^{2+} ionic environment and therefore is not effective for erasure [31].

The defect centers in FP glasses include phosphorus-oxygen hole centers (POHCs) and defects such as PO_2, PO_3 and PO_4complexes which consist of electrons trapped on phosphate group precursors [22–25,51]. These defects are generally called phosphorus-oxygen electron

centers (POECs) [30]. On the other hand, the precise nature of the defects in FA glasses is uncertain as FA glasses are not as well studied in the literature.

In this paper, we investigate different processes occurring in a Sm-doped fluorophosphate glass under the influence of X-ray irradiation, including the formation of defect centers and their correlation with samarium valency conversion. The investigation is based on ESR and optical absorption spectroscopy. We examine the X-ray irradiated FP glasses doped with different Sm-ion concentrations and also study the effect of thermal annealing on defects. We have deliberately chosen to study FP rather than FA glasses inasmuch as FP glasses are among the more thoroughly investigated glasses, and their properties are much better understood. Indeed, FP glasses without RE doping have also been used in dosimetry [52]. FP glasses are therefore a better candidate for optical absorption and ESR studies than FA glasses. Prior knowledge on defects in FP glasses has allowed us to associate different features and bands of the spectra to well known POHC and POEC defects and hence provide a better understanding of the physical processes that take place in these glasses during the Sm^{3+} to Sm^{2+} ion conversion under X-ray irradiation.

5.3 Experimental

Fluorophosphate (FP) glasses can be thought of as a combination of fluoride and phosphate glasses with a variety of possible cationic species. Samples used in the present study were synthesized and prepared based on the FP10 composition published by Ebendorff-Heidepriem [25]. The FP10 batch composition is given in mol% as 10.0Sr $(PO_3)_2$-34.4AlF_3-10MgF_2-30.4CaF_2-15.2SrF_2. The FP10 glasses were doped with Sm^{3+} by adding SmF_3 with concentrations varying from 0.001 to 0.5 mol%. Assuming full Sm ionization, it gives us a variation of Sm^{3+} concentration from 0.001 to 0.5 at. %. The quenched glass samples were cut in

smaller pieces suitable for ESR and optical absorption spectroscopy experiments. The glass transition temperature T_g of the FP glasses used in this work was measured by using a temperature modulated differential scanning calorimeter (TMDSC), and was found to be approximately 460°C. Annealing experiments were carried out at temperatures 100°C to 550°C using a temperature controlled furnace.

The X-ray irradiation was performed using the emission produced by a commercial FAXITRON X-ray set with a tungsten anode and 0.76 mm Beryllium filtration placed approximately 5 cm from the anode. The X-ray tube operates at 110 kVp (mean energy ~45 keV, calculated using reference [53]) with an approximate dose rate of 50 Gy/min. The quoted dose rate represents dose in air at the surface of the sample, which is the usual manner in which dose is reported for MRT.

The steady-state photoluminescence (PL) spectra were measured from 200 nm to 1200 nm, using an ASEQ fiber input mini-spectrometer with spectral resolution better than 1 nm. The excitation source for all the photoluminescence spectra was a laser diode with an emission wavelength at 405 nm, which can be used to excite both the Sm^{3+} and Sm^{2+} ions [54]. The intensity of excitation was kept as low as possible to minimize the effect of $Sm^{2+} \rightarrow Sm^{3+}$ reconversion during the measurements. The transmittance spectra were recorded using a Perkin-Elmer Lambda 900 spectrophotometer. The samples were polished flat for these measurements. Electron Spin Resonance (ESR) spectroscopy measurements were carried out using a standard Bruker EMX 10/2.7 instrument working at X-band frequency (~9.8 GHz) so as to obtain the first derivative ESR. All samples were prepared to have the same geometry 1.5 mm × 1.5 mm × 6 mm (to avoid sample shape dependence in ESR measurements) and carefully placed in the same position inside the cavity for each measurement. Further, ESR measurements

were also checked for reproducibility. The background signal was recorded and subtracted after each single spectral recording. The ESR signal intensities were normalized to the mass of the samples. ESR measurements were conducted at room temperature, following X-ray irradiation and after each step of thermal annealing.

5.4 Results and Discussion

5.4.1 ESR Spectra

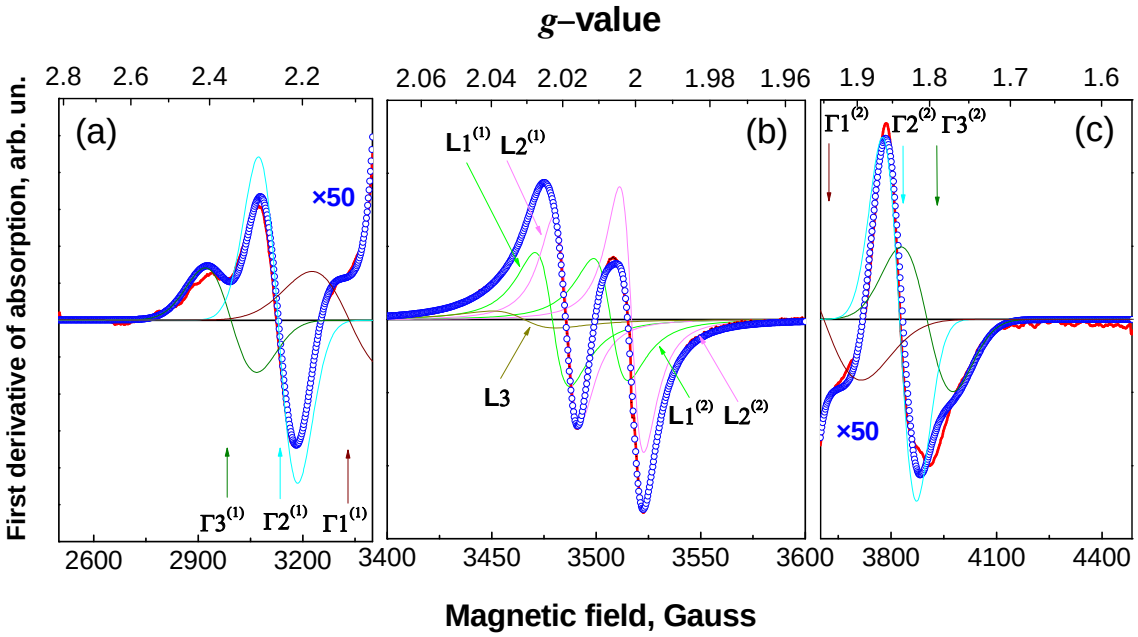

Figure 5.1 The electron spin resonance (ESR) signal of FP glass doped with 0.2% of Sm^{3+} and X-ray irradiated for 2 hours (total dose of ~6 kGy). The spectra were measured after annealing the irradiated sample at 100°C and cooling back to room temperature. The experimental data (thick solid lines) are approximated by a sum of five doublets and one singlet (symbols). Two doublets (L_1 and L_2) and the singlet L_3 have Lorentzian lineshapes while the other three doublets (Γ_1–Γ_3) are Gaussians. The singlet and the individual components of each doublet are shown by thin solid lines and are marked by superscript (1) or (2). Note the change of scale (compression over the x-axis and stretching over y-axis by a factor of 50) in the wings, (a) and (c), of the graph. The lower scale is shown for a nominal frequency of 9.85 GHz.

Figure 5.1 presents a typical ESR signal of an X-ray irradiated Sm-doped FP glass sample. Prior to irradiation, we could not detect any significant ESR signal. It is worth noting the change of scale in Figure 5.1(a) and Figure 5.1(c) (the "wings") in comparison with Figure 5.1(b). In

other words, the central part of the ESR signal consists of very strong and narrow lines which are usually associated with POHC. Meanwhile, the weaker wings are commonly related to PO_2, PO_3 and PO_4 complexes which readily capture electrons [22,24,25,51]; we refer to these defects as POEC [30].

For future interpretation and numerical comparisons, we have presented the ESR spectra as combinations of elementary lines such as Lorentzians and Gaussians. In order to have a self-consistent interpretation, we used a *unique set* of Lorentzians and Gaussians (characterized by positions and widths) for *the whole set of* ESR spectra obtained in all our experiments. Figure 5.1(a)-(c) illustrate typical examples of these efforts. The intense central part of the ESR spectrum is presented as a sum of the first derivatives of five Lorentzians while the weaker signals in the wings use the first derivatives of six Gaussians. The positions and width of these Lorentzian and Gaussian elementary lines are summarized in Table 5.1. The weighting factors for the latter lines are used as adjustable parameters and their values are discussed below. We wish to stress that we have used the minimum number of lines required to fit *all* our spectra, and the quality of fitting is illustrated by Figure 5.1(a)-(c).

We have already mentioned that the weaker signals in the wings of ESR spectra are usually associated with PO_2, PO_3 and PO_4complexes. In our particular case, this implies that the six Gaussians may be interpreted as belonging to three doublets (Γ_1, Γ_2 and Γ_3) related to these complexes. The spin-Hamiltonian parameters of Γ_1, Γ_2 and Γ_3 and their assignments to PO complexes are shown in Table 5.1.

There is also a good consensus that the strong and narrow central lines are associated with POHC [22,24,25,30,51]. Therefore, in the following we will analyze only the summed and

Table 5.1 The *unique set* of Lorentzians and Gaussians (characterized by positions and widths) used for approximating *the whole set of* ESR spectra obtained in our experiments. Doublets (L_1–L_2) and singlet L_3 have Lorentzian (L) and doublets (Γ_1–Γ_3) have Gaussian (Γ) lineshapes. *W* is a full width of each line at half maximum. $g^{(1)}$ and $g^{(2)}$ are the effective *g*-values for each line of a doublet. $g_{average}$ is the average of $g^{(1)}$ and $g^{(2)}$. *A* is splitting of two lines of a doublet. *W* and *A* are defined for a nominal frequency of 9.8 GHz.

Doublets	$g_{average}$	***A*, Gauss**	***W*, Gauss**	$g^{(1)}$	$g^{(2)}$	**Nature**[b]
L_1	2.014	28	28	2.022	2.006	POHC
L_2	2.009	31	21	2.018	2.000	POHC
L_3[a]	2.030	No hyperfine splitting	52	-	-	OHC?
Γ_1	2.030	276	251	2.111	1.949	POEC (PO_2)
Γ_2	2.044	695	123	2.248	1.840	POEC (PO_3)
Γ_3	2.076	908	173	2.350	1.803	POEC (PO_4)

[a]Singlet, [b]Based on comparison with [22] and [25].

integrated strength of the POHC related ESR signals, which is simply proportional to the total concentration of POHC. However, we made an attempt to deconvolute the ESR signal and obtained five Lorentzians, tentatively belonging to two doublets (L_1 and L_2) and one singlet (L_3) whose spin-Hamiltonian parameters are summarized in Table 5.1. Tentatively, we assume that the doublets L_1 and L_2 may be attributed to two different types of POHC, *i.e.* r-POHC and l-POHC [24,51]. In the r-POHC (which was labeled as the stable form of POHC by Griscom [51]), the unpaired spin is shared between the two non-bridging oxygens [23] in the structure. On the other hand, l-POHC was initially reported to be stable only at low temperatures. However, Origlio *et al.* showed that this structure can be observed at room temperature as well. The weaker singlet with $g = 2.030$ cannot be found in non-annealed samples, and appears only after thermal treatment. Unfortunately, there is no reported reliable assignment to any particular structural unit. However, it might be tentatively ascribed to so-called OHC (oxygen related centers of

unknown structure) [25]. As a conclusion of this discussion, it is worth noting that all Lorentzians strongly overlap. Consequently, despite the above description being the most probable, it may not be unique and needs to be studied further.

5.4.2 Effect of Sm Doping Concentration on Defects

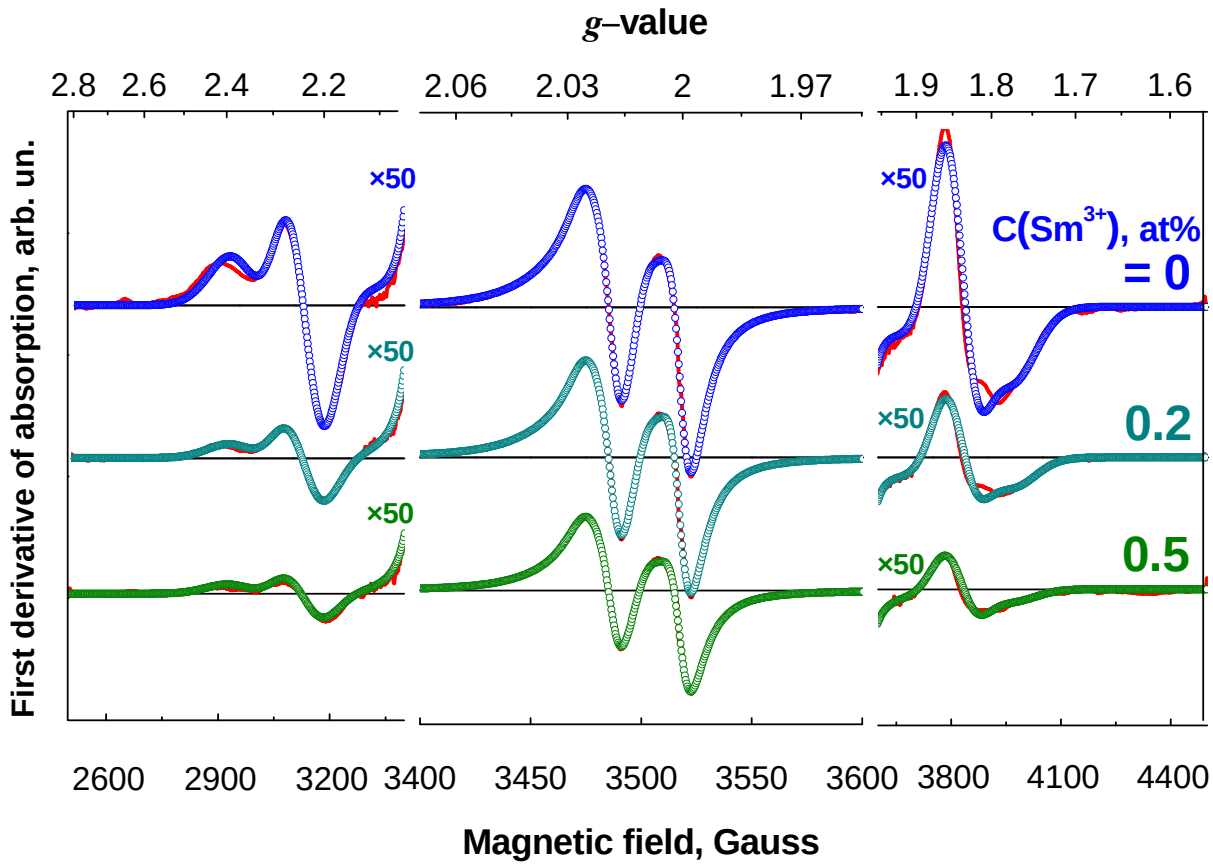

Figure 5.2 Variation of ESR spectra of FP glass samples as a result of changing the concentration of Sm^{3+} (C_0) in the range of 0–0.5 at.%. All the samples were X-ray irradiated for 2 hours prior to the ESR measurement. Symbols are approximation of experimental data based on the approach presented in Figure 5.1 and Table 5.1. All the signal intensities are normalized to the mass of the samples.

Figure 5.2 presents a series of ESR spectra of FP glasses that had been X-ray irradiated for 2 hours. The samples have different concentrations of Sm^{3+}. It is clearly seen that the increase in the Sm^{3+} doping concentration (C_0) reduces the ESR signal intensity.

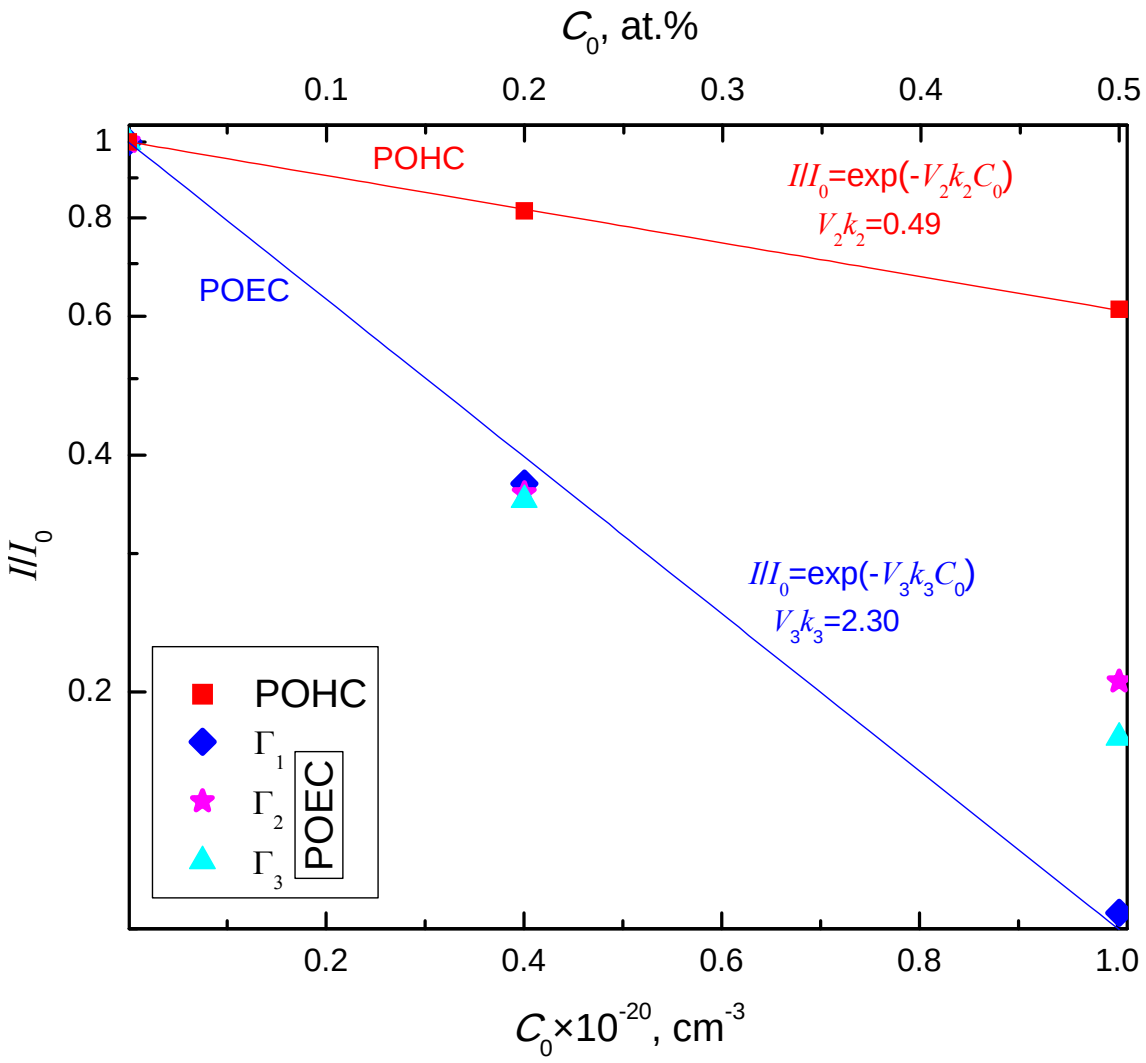

Figure 5.3 Variation of ESR signal components ascribed to POHC and POEC according to Table 5.1 versus Sm doping concentration (C_0). All the samples were X-ray irradiated for 2 hours prior to the ESR measurement. ESR signal intensities were normalized to the mass of the samples. I is the intensity of POHC related Lorentzian and POEC related Gaussian lines presented in Table 5.1. In case of Lorentzians, I is the summed intensity of L_1–L_3. Note that the first derivative of these lines sum up to simulate the ESR signal (symbols in Figure 5.2). I_0 is the corresponding intensity in the undoped glass irradiated for the same time (same dose). Lines are the fits using the formulas and the fitting parameters as shown in the figure. (The maximum C_0 value along the x-axis is 1×10^{20} cm^{-3}.)

Figure 5.3 shows that the POHC related ESR signal, as well as POEC related Gaussian doublets Γ_1, Γ_2 and Γ_3 decrease exponentially with increasing C_0. However, POEC related components decrease at a faster rate with C_0 in comparison with those of POHC.

The above data may be explained by using a model that accounts for the chemical reactions occurring in the glass under X-ray irradiation. High energy X-rays create a large number of electron-hole pairs, which can be captured at pre-existing traps (precursors). Due to the photogeneration process (a primary projectile photoelectron ionizing the glass medium) a hole capturing reaction typically takes place in the vicinity of an electron capturing reaction. The reduction of RE ions usually takes place together with the formation of "oxygen-associated trapped hole centers [21]" nearby [6,20,26]. There are at least three "primary" reactions which consume X-ray generated electrons and holes

$$Sm^{3+} + e^{-} \rightarrow Sm^{2+} \qquad (5.1)$$

$$PO + e^{-} \rightarrow POEC \qquad (5.2)$$

$$PO + h^{+} \rightarrow POHC \qquad (5.3)$$

It should be emphasized that Sm^{2+} ions created as a result of X-ray irradiation have a metastable ionic environment since the relaxation of glass structure surrounding the Sm^{2+}-ions cannot take place at room temperature (far below the glass transition temperature) as we discussed in our previous work [31]. These ions are usually referred to as $(Sm^{3+})^{-}$ or (Sm^{2+})* to distinguish them from Sm^{2+} in thermally reduced (or structurally relaxed) glass [13,19]. Consequently, we should also include the inverse "secondary" reaction of Sm^{2+} to Sm^{3+} reconversion due to the capture of holes.

$$Sm^{2+} + h^{+} \rightarrow Sm^{3+} \qquad (5.4)$$

In all these reactions, the term PO has the general meaning of being a precursor for POHC or POEC creation by capturing the appropriate charge carrier on the PO bond. Equations (5.1) and (5.2) clearly show that Sm^{3+} ions and some of PO precursors compete for electrons in the vicinity of reaction defined by Eq. (5.3), which captures holes. Therefore, it is reasonable to

assume that POEC formation in the glass would be suppressed by increasing the Sm^{3+} doping concentration (C_0). Mathematically, this dependence may be expressed as

$$n_{\mathrm{POEC}} = n_0 e^{-V_3 C_3} \qquad (5.5)$$

where C_3 stands for the unconverted Sm^{3+} concentration and V_3 is the so-called "capture volume" of an Sm^{3+}-ion for an electron. This mathematical approach was initially put forward by Stroud [55], and later further developed by Bocharova [56]. According to the "capture volume" model, the competition between activator ions and defect precursors in doped glasses leads to an $n = n_0\exp(-VC)$ dependence where, n and n_0 are the concentration of trapping centers formed in doped and undoped glasses, respectively, C is the concentration of activator ions and V is the effective "capture volume". (Note that doped and undoped glasses receive equal radiation dose. Also note that the concentration of POHC is equal to the concentration of POEC in the undoped glass, *i.e.* $(n_{\mathrm{POHC}})_{\mathrm{undoped}} = (n_{\mathrm{POEC}})_{\mathrm{undoped}} = n_0$ due to the charge neutrality condition). In other words, increasing the concentration of activator ions would exponentially suppress the formation of defect centers. The physics of the process is actually straightforward. If a precursor lies within the "capture volume" of the activator ion, the electron (or hole) would be preferably captured by the activator ion and would be obviously "lost" or not available for defect precursors.

Similarly, another pair of reactions defined by Eqs. (5.3) and (5.4) obviously compete for holes while, the electrons would be captured by the nearest neighbouring POEC precursors according to Eq. (5.2). The competition for holes between Eqs. (5.3) and (5.4) can be expressed as

$$n_{\mathrm{POHC}} = n_0 e^{-V_2 C_2} \qquad (5.6)$$

where V_2 stands for the capture volume of the Sm^{2+} ion for a hole and C_2 stands for Sm^{2+} concentration. However, Eq. (5.4) cannot effectively suppress the POHC creation because

the "secondary" Eq. (5.4) relies on the re-conversion of Sm^{2+}, which appears only as the result of the "primary" Eq. (5.1) and is absent prior to X-ray irradiation.

Assuming that time dependent Sm^{2+} and Sm^{3+} concentrations $C_2(t)$ and $C_3(t)$ should be proportional to initial concentration of Sm^{3+}, C_0, one can present

$$C_2(t) = k_2(t)C_0 \text{ and } C_3(t) = k_3(t)C_0 \qquad (5.7)$$

where $k_2(t)$ and $k_3(t)$ are time dependent coefficients with t standing for the irradiation time and obviously, $k_2(t) + k_3(t) = 1$. By using Eq. (5.7) we can rewrite Eqs. (5.5) and (5.6) in terms of C_0:

$$\frac{n_{\mathrm{POEC}}}{n_0} = e^{-V_3 k_3 C_0} \qquad (5.8)$$

$$\frac{n_{\mathrm{POHC}}}{n_0} = e^{-V_2 k_2 C_0} \qquad (5.9)$$

Figure 5.3 shows good agreement of Eqs. (5.8) and (5.9) with experimental data assuming that the intensity (I) of the ESR signal components related to POHC and POEC are proportional to n_{POHC} and n_{POEC}, respectively. Figure 5.3 also clearly shows that the decay constant of Eq. (5.9) is much less than that of Eq. (5.8). This agrees with the predictions of the model. In other words, the formation of POHC is suppressed weakly as it was not directly influenced by increasing Sm doping concentration, C_0, but by a "secondary" consequence of it.

5.4.3 Effect of Thermal Annealing on Defects

Annealing is known to be an effective method of re-converting Sm^{2+} to Sm^{3+} and for the elimination of X-ray induced defect centers [31]. Figure 5.4 represents the evolution of ESR spectra of the same sample (FP doped with 0.2% of Sm^{3+}) that has been subject to a step-by-step annealing. This treatment involves a series of 30 minute sequential annealing processes at increasing temperatures (100 °C − 300 °C) interrupted by cooling down to room temperature

after each step to perform the necessary measurements. It is apparent from this figure that the central "POHC related" part of the ESR spectra decreases rapidly while the "POEC related" wings remain almost constant as a result of thermal annealing.

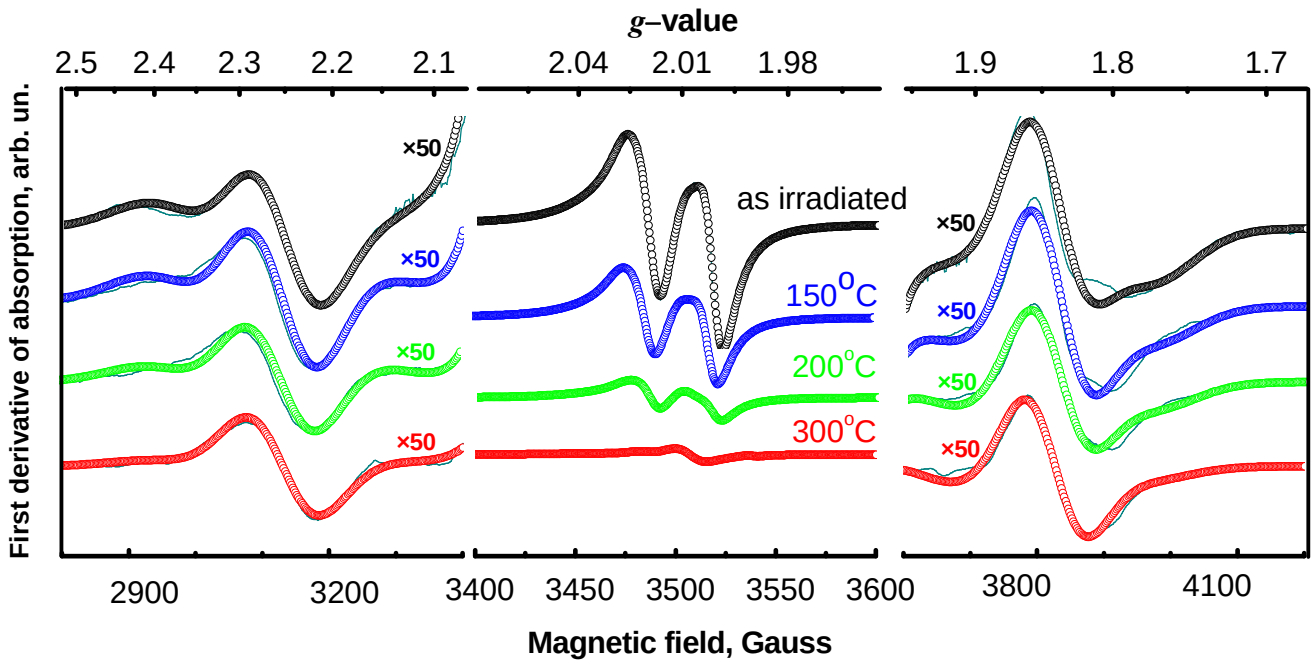

Figure 5.4 The evolution of EPR spectra of the same sample (FP doped with 0.2% of Sm^{3+}) experiencing a step-by-step annealing treatment carried out at increasing temperatures (100°C−300°C) and cooled back to room temperature after each step. The time duration for every annealing step is 30 min. The sample was X-ray irradiated for 2 hours prior to annealing. The experimental ESR data (thick solid lines) are approximated by a sum (symbols) of functions presented in Table 5.1 and Figure 5.1.

Optical transmittance spectra were also recorded after each step of annealing and induced absorbance calculated (typical induced absorbance spectrum is not shown but can be found in [30]). To interpret the data, we performed a so-called "band separation" analysis [57] on induced absorbance spectra and approximated it as a sum of six Gaussians (G1−G6) based on the approach described in our previous work [30] where we associated these bands with POHC and POEC defects according to comparison with the results reported in reference [22].

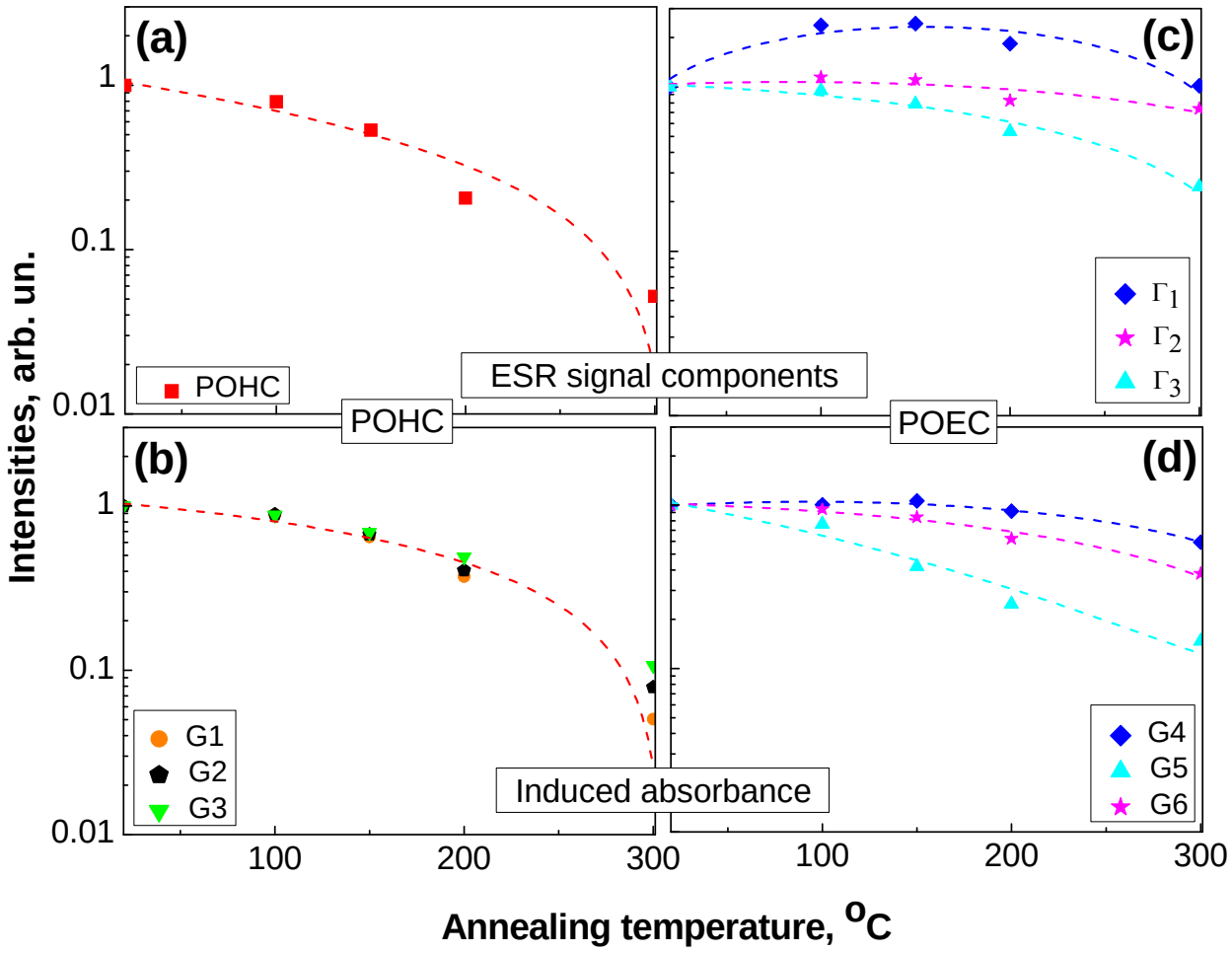

Figure 5.5 The variation of ESR signal components (a) and (c) and induced absorbance bands (b) and (d) (symbols) versus annealing temperatures (100°C−300°C) related to the same sample of Figure 5.4 (doped with 0.2% of Sm^{3+} and X-ray irradiated for 2 hours prior to annealing). Symbols in (a) and (c) correspond to the intensity of lines presented in Table 5.1 used for approximation of experimental data of Figure 5.4. Symbols in (b) and (d) correspond to the intensity of bands G1−G6 introduced in [30]. (a) and (b) correspond to POHC related bands while (c) and (d) to POEC related bands. All the intensities are normalized to their value at room temperature (20°C) just after irradiation for 2 hours. Lines are guides to eye.

More detailed analysis maybe done by studying the behavior of Gaussian and Lorentzian components of the ESR signal which is presented in Figure 5.5(a) and Figure 5.5(c) in comparison with induced absorbance bands shown in Figure 5.5(b) and Figure 5.5(d). The parameters of the ESR components used here are the same as before and are listed in Table 5.1. The parameters of induced absorbance bands can be found in [30] Table 5.1. Notice that there is

a good correlation of ESR data in Figure 5.5(a) and Figure 5.5(c) with the corresponding data on induced absorbance in Figure 5.5(b) and Figure 5.5(d).

Surprisingly, some of the POEC related signals seem to increase with the annealing temperature T_A while others remain almost constant or decrease. This may be interpreted as an indicator that some electrons released from one POEC band may be recaptured by another POEC band, inasmuch as there is no other process in the glass that would sink electrons. Meanwhile, Figure 5.5(a) and Figure 5.5(b) clearly show that the concentration of POHC monotonically decreases with increasing T_A, which is reflected in the decrease of corresponding signals. It seems that the thermal annealing at moderate temperatures (T_A ~350 °C) is sufficiently efficient for destroying POHCs. TL glow curve previously obtained in FP glass shows a peak related to phosphorus-oxygen based defects in the same temperature range [35]. Similar results have been observed for another kind of oxygen-associated trapped hole center (NBOHC) in silica glass [33]. One possible mechanism for the destruction of POHCs could be through the following chemical reactions (however, further investigations may be required):

$$Sm^{2+} \rightarrow Sm^{3+} + e^{-} \qquad (5.10)$$

$$POHC + e^{-} \rightarrow PO \qquad (5.11)$$

Furthermore, the ESR spectra recorded in a wider range (g = 1−3.5) illustrated in Figure 5.6 reveal some useful and interesting information. The trace of an extremely broad ESR signal (wider than 5000 Gauss) is noticeable in Figure 5.6. This very broad signal shows a correlation with the presence of Sm^{2+} ions (inset of Figure 5.6) and disappears in undoped samples or samples annealed at very high temperatures (550 °C) where only Sm^{3+} ions are present as shown in Figure 5.6. The signal was reproducible. We suggest that the observed signal is probably

related to Sm^{2+} ions which are non-Kramer ions and expected to produce very broad ESR lines [58].

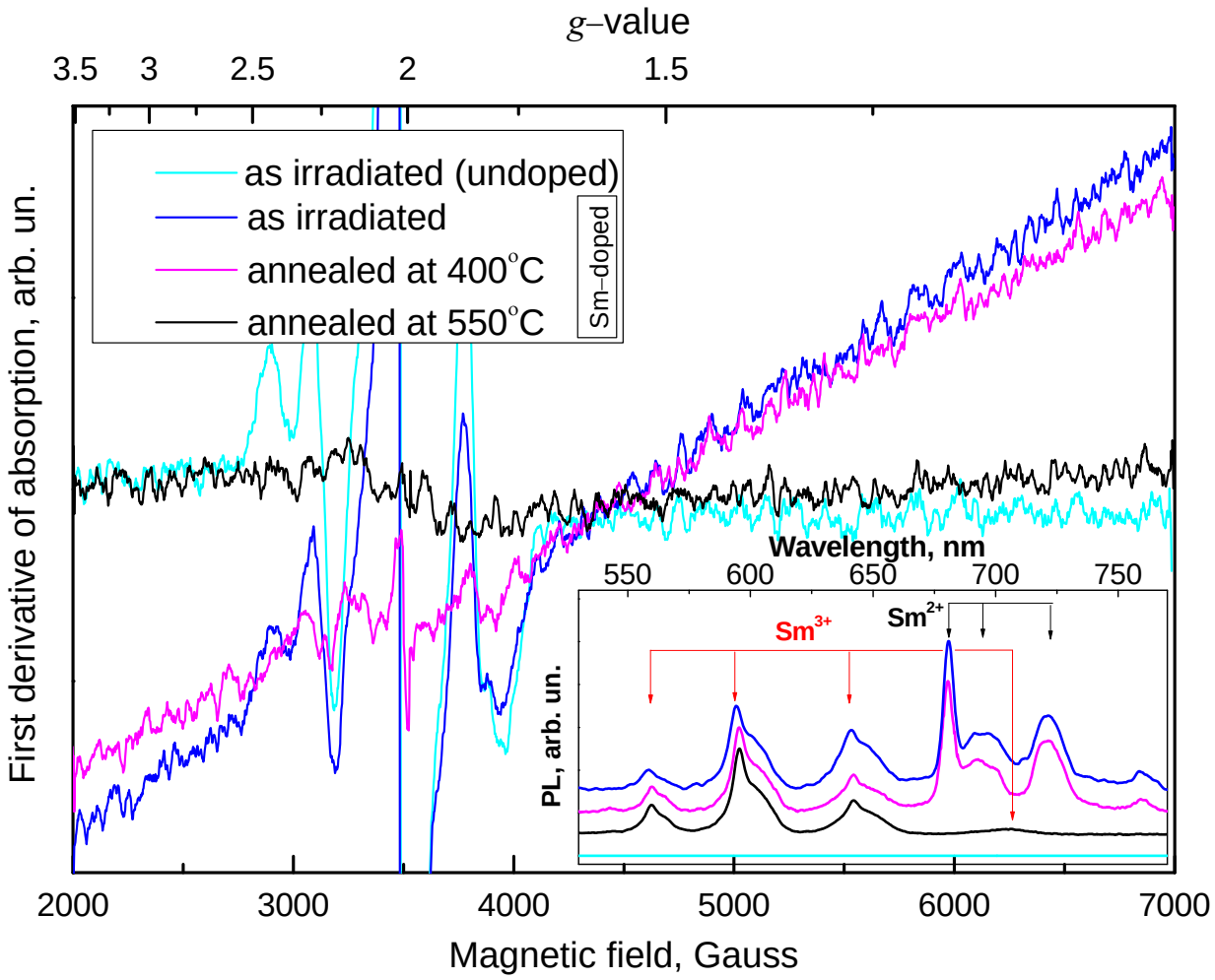

Figure 5.6 (a) ESR signal of undoped and doped (0.2% of Sm^{3+}) FP samples recorded in a very wide range. All the samples were X-ray irradiated for 2 h prior to annealing and ESR measurements. The annealing duration was 30 min. Inset shows the corresponding photoluminescence spectra (shifted vertically to facilitate the comparison). Narrow ESR lines observed in the range $g = 1.7-2.6$ are the same kind of lines shown in Figure 5.4 related to X-ray induced defects. Note the wide range deviation of the ESR signal in samples which show Sm^{2+} photoluminescence.

It must also be noted that at 550 °C, which is above the glass transition temperature, the ESR signals (related to defects or Sm^{2+}ions) almost totally disappear as shown in Figure 5.6. This implies the ionic reconstruction and erasure of almost all consequences of X-ray irradiation. On

the other hand, the annealing at temperatures less than T_g (and above 350 °C) is known to increase the brightness of Sm^{2+} PL (for example, the annealed sample at 400 °C shown in the inset in Figure 5.6). This phenomenon was discussed in our previous work [31] and was attributed to the formation of stable Sm^{2+} ions due to ionic structural rearrangement at elevated temperatures. It is interesting to note that we see the very broad ESR signal ascribed to Sm^{2+} ions in the samples annealed at 400 °C as well (Figure 5.6).

5.5 Conclusion

X-ray irradiation of Sm-doped fluorophosphate glasses results in Sm^{3+} to Sm^{2+} ion conversion along with the formation of a number of defects in the glass structure. The difference in the photoluminescence signatures of Sm^{3+} and Sm^{2+} ions can be used for high resolution dosimetry required for microbeam radiation therapy (MRT). Towards developing such a detector, we studied the nature of X-ray induced defects and their dependence on Sm doping concentration and thermal annealing by using ESR and optical absorbance spectroscopy. We showed that the intense central part of the ESR spectrum, usually associated with so-called POHC (phosphorus-oxygen hole center), may be presented as a sum of Lorentzians. Meanwhile, much weaker wings of the spectrum, usually associated with PO electron centers (which we refer to as POEC), may be approximated by a sum of Gaussians. We observed that both POHC and POEC related signals decrease exponentially with increasing Sm doping concentration, while the POEC related signals show a faster decay with the Sm-concentration. We were able to interpret these experimental results by a model that is based on competition between various defects and Sm-ions for the electrons and holes generated by the absorption of X-rays. The model suggests that the valency reduction of Sm^{3+} ions (electron centers) occurs together with the formation of POHCs (hole centers) within their vicinity. Sm^{3+} ions prevent the competing POEC precursors (POEC

precursors within the Sm^{3+} capture volume) from capturing electrons, which results in the reduction of these defect centers with increasing Sm doping concentration. POHC formation would also be somewhat suppressed, which is due to the less dominant reaction of Sm^{2+} to Sm^{3+} reconversion that prevents the nearby POHCs from capturing holes. Annealing the irradiated glass at increasing moderate temperatures (up to 300 °C) results in the reduction of the central "POHC related" part of the ESR spectra while, the "POEC related" wings almost survive. POHC and POEC related induced absorbance bands exhibit almost the same behavior. These results can be explained by considering that X-ray induced Sm^{2+} ions have a metastable structure which can be easily destroyed along with POHCs near them under moderate temperature annealing. On the other hand, since there is not such a reaction affecting POECs, the overall POEC concentration remains almost constant. Annealing at temperatures between 350 °C and the glass transition temperature (~460 °C) leads to the formation of stable Sm^{2+} ions (which produce a broad ESR signal) whereas above the glass transition temperature, almost all Sm^{2+} ions become reconverted back to Sm^{3+} and almost all defects become annealed out; there is no marked ESR signal. Our results suggest that the samarium valency conversion is correlated with the formation and destruction of defect centers which should be considered in designing Sm-doped FP glass plate detectors for MRT. It is also clear that annealing above the glass transition temperature can return the irradiated sample back to its original unirradiated state for reuse; a distinct advantage in MRT since once calibrated, the same Sm-doped FP glass can be reused many times.

Acknowledgments

We thank NSERC and the New Zealand Ministry for Business, Innovation and Employment for financial support and Teledyne-DALSA for sponsoring the project through an NSERC

Strategic Grant. Shahrzad Vahedi is a Fellow in the Canadian Institutes of Health Research Training program in Health Research Using Synchrotron Techniques (CIHR-THRUST).

5.6 References and Links

1. J. Yang, H. Guo, Y. Wei, H. M. Noh, and J. H. Jeong, "Luminescence and energy transfer process in Cu^{+},Sm^{3+} co-doped sodium silicate glasses," Opt. Mater. Express **4**, 315-320 (2014).

2. G. Gao, and L. Wondraczek, "Spectral asymmetry and deep red photoluminescence in Eu^{3+}-activated $Na_3YSi_3O_9$ glass ceramics," Opt. Mater. Express **4**, 476-485 (2014).

3. F. Wang, L. F. Shen, B. J. Chen, E. Y. B. Pun, and H. Lin, "Broadband fluorescence emission of Eu^{3+} doped germanotellurite glasses for fiber-based irradiation light sources," Opt. Mater. Express **3**, 1931-1943 (2013).

4. L. Li, Y. Yang, D. Zhou, Z. Yang, X. Xu, and J. Qiu, "Investigation of the interaction between different types of Ag species and europium ions in Ag^{+}-Na^{+} ion-exchange glass," Opt. Mater. Express **3**, 806-812 (2013).

5. S. Park, K. W. Jang, S. Kim, I. Kim, and H. Seo, "X-ray-induced reduction of Sm^{3+}-doped SrB_6O_{10} and its room temperature optical hole burning," J. Phys.-Condens. Mat. **18**, 1267-1274 (2006).

6. M. Nogami, and K. Suzuki, "Formation of Sm^{2+} ions and spectral hole burning in X-ray irradiated glasses," J. Phys. Chem. B **106**, 5395-5399 (2002).

7. S. Qi, Y. Huang, T. Tsuboi, W. Huang, and H. J. Seo, "Versatile luminescence of $Eu^{2+,3+}$-activated fluorosilicate apatites $M_2Y_3[SiO_4]_3F$ (M = Sr, Ba) suitable for white light emitting diodes," Opt. Mater. Express **4**, 396-402 (2014).

8. E. Malchukova, B. Boizot, G. Petite, and D. Ghaleb, "Optical properties and valence state of Sm ions in aluminoborosilicate glass under beta-irradiation," J. Non-Cryst. Solids **353**, 2397-2402 (2007).

9. G. Okada, B. Morrell, C. Koughia, A. Edgar, C. Varoy, G. Belev, T. Wysokinski, D. Chapman, and S. Kasap, "Spatially resolved measurement of high doses in microbeam radiation therapy using samarium doped fluorophosphate glasses," Appl. Phys. Lett. **99** (2011).

10. L. Y. Yang, N. Da, D. P. Chen, Q. Z. Zhao, X. W. Jiang, C. S. Zhu, and J. R. Qiu, "Valence state change and refractive index change induced by femtosecond laser irradiation in Sm^{3+} doped fluoroaluminate glass," J. Non-Cryst. Solids **354**, 1353-1356 (2008).

11. K. Miura, J. R. Qiu, S. Fujiwara, S. Sakaguchi, and K. Hirao, "Three-dimensional optical memory with rewriteable and ultrahigh density using the valence-state change of samarium ions," Appl. Phys. Lett. **80**, 2263-2265 (2002).

12. J. R. Qiu, Y. Shimizugawa, Y. Iwabuchi, and K. Hirao, "Photostimulated luminescence in Eu^{2+}-doped fluoroaluminate glasses," Appl. Phys. Lett. **71**, 759-761 (1997).

13. Y. D. Li, Y. L. Huang, C. F. Jiang, and K. Jang, "The dependence of luminescence on reduction of Sm^{2+} ions doped in lithium barium borate glasses," Appl. Phys. A 97, 663-669 (2009).

14. Y. D. Li, J. Y. Wang, Y. L. Huang, and H. J. Seo, "Temperature-dependent $^5D_0 \rightarrow {}^7F_0$ luminescence of Sm^{2+} ions doped in alkaline earth borophosphate glass," J. Am. Ceram. Soc. **93**, 722-726 (2010).

15. K. W. Jang, Y. F. Huang, W. X. Zha, E. J. Cho, H. S. Lee, X. G. Wang, D. Qin, Y. Zhang, C. F. Hang, and H. J. Seo, "Irradiation-induced reduction and luminescence properties of Sm^{2+} doped in $BaBPO_5$," J. Solid State Chem. **180**, 3325-3332 (2007).

16. J. R. Qiu, K. Miura, T. Suzuki, T. Mitsuyu, and K. Hirao, "Permanent photoreduction of Sm^{3+} to Sm^{2+} inside a sodium aluminoborate glass by an infrared femtosecond pulsed laser," Appl. Phys. Lett. **74**, 10-12 (1999).

17. B. H. Babu, and V. V. R. K. Kumar, "Fluorescence properties and electron paramagnetic resonance studies of gamma-irradiated Sm^{3+}-doped oxyfluoroborate glasses," J. Appl. Phys. **112**, 093516 (2012).

18. E. Malchukova, B. Boizot, D. Ghaleb, and G. Petite, "Optical properties of pristine and gamma-irradiated Sm doped borosilicate glasses," Nucl. Instrum. Meth. A **537**, 411-414 (2005).

19. K. Fujita, C. Yasumoto, and K. Hirao, "Photochemical reactions of samarium ions in sodium borate glasses irradiated with near-infrared femtosecond laser pulses," J. Lumin. **98**, 317-323 (2002).

20. M. Nogami, G. Kawamura, G. J. Park, H. P. You, and T. Hayakawa, "Effect of Al^{3+} and Ti^{4+} ions on the laser reduction of Sm^{3+} ion in glass," J. Lumin. **114**, 178-186 (2005).

21. D. L. Griscom, "Esr studies of radiation-damage and structure in oxide glasses not containing transition group ions - a contemporary overview with illustrations from alkali borate system," J. Non-Cryst. Solids **13**, 251-285 (1974).

22. P. Ebeling, D. Ehrt, and M. Friedrich, "X-ray induced effects in phosphate glasses," Opt. Mater. **20**, 101-111 (2002).

23. L. B. Fletcher, J. J. Witcher, N. Troy, S. T. Reis, R. K. Brow, R. M. Vazquez, R. Osellame, and D. M. Krol, "Femtosecond laser writing of waveguides in zinc phosphate glasses [Invited]," Opt. Mater. Express **1**, 845-855 (2011).

24. G. Origlio, F. Messina, S. Girard, M. Cannas, A. Boukenter, and Y. Ouerdane, "Spectroscopic studies of the origin of radiation-induced degradation in phosphorus-doped optical fibers and preforms," J. Appl. Phys. **108**, 123103 (2010).

25. H. Ebendorff-Heidepriem, and D. Ehrt, "Effect of Tb^{3+} ions on X-ray-induced defect formation in phosphate containing glasses," Opt. Mater. **18**, 419-430 (2002).

26. Y. Huang, C. Jiang, K. Jang, H. S. Lee, E. Cho, M. Jayasimhadri, and S.-S. Yi, "Luminescence and microstructure of Sm^{2+} ions reduced by X-ray irradiation in $Li_2O–SrO–B_2O_3$ glass," J. Appl. Phys. **103**,113519 (2008).

27. S. Rydberg, and M. Engholm, "Experimental evidence for the formation of divalent ytterbium in the photodarkening process of Yb-doped fiber lasers," Opt. Express **21**, 6681-6688 (2013).

28. H. Gebavi, S. Taccheo, D. Tregoat, A. Monteville, and T. Robin, "Photobleaching of photodarkening in ytterbium doped aluminosilicate fibers with 633 nm irradiation," Opt. Mater. Express **2**, 1286-1291 (2012).

29. G. Okada, J. Ueda, S. Tanabe, G. Belev, T. Wysokinski, D. Chapman, D. Tonchev and S. Kasap, "Samarium-doped oxyfluoride glass-ceramic as a new fast erasable dosimetric detector material for microbeam radiation cancer therapy applications at the Canadian synchrotron," J. Am. Ceram. Soc. doi: 10.1111/jace.12938 (2014).

30. B. Morrell, G. Okada, S. Vahedi, C. Koughia, A. Edgar, C. Varoy, G. Belev, T. Wysokinski, D. Chapman, R. Sammynaiken, and S. O. Kasap, "Optically erasable samarium-doped fluorophosphate glasses for high-dose measurements in microbeam radiation therapy," J. Appl. Phys. **115**, 063107 (2014).

31. S. Vahedi, G. Okada, B. Morrell, E. Muzar, C. Koughia, A. Edgar, C. Varoy, G. Belev, T. Wysokinski, D. Chapman, and S. Kasap, "X-ray induced Sm^{3+} to Sm^{2+} conversion in fluorophosphate and fluoroaluminate glasses for the monitoring of high-doses in microbeam radiation therapy," J. Appl. Phys. **112**, 073108 (2012).

32. A. Edgar, C. R. Varoy, C. Koughia, D. Tonchev, G. Belev, G. Okada, S. O. Kasap, H. von Seggern, and M. Ryan, "Optical properties of divalent samarium-doped fluorochlorozirconate glasses and glass ceramics," Opt. Mater. **32**, 266-266 (2009).

33. J. J. Witcher, W. J. Reichman, L. B. Fletcher, N. W. Troy, and D. M. Krol, "Thermal annealing of femtosecond laser written structures in silica glass," Opt. Mater. Express **3**, 502-510 (2013).

34. A. V. Kir'yanov, S. Ghosh, M.C. Paul, Y.O. Barmenkov, V. Aboites and N.S. Kozlova, " Ce-doped and Ce/Au-codoped alumino-phosphosilicate fibers: Spectral attenuation trends at high-energy electron irradiation and posterior low-power optical bleaching," Opt. Mater. Express **4**, 434-448 (2014).

35. G. Okada, S. Vahedi, B. Morrell, C. Koughia, G. Belev, T. Wysokinski, D. Chapman, C. Varoy, A. Edgar, and S. Kasap, "Examination of the dynamic range of Sm-doped glasses for high-dose and high-resolution dosimetric applications in microbeam radiation therapy at the Canadian synchrotron," Opt. Mater. **35**, 1976-1980 (2013).

36. D. N. Slatkin, P. Spanne, F. A. Dilmanian, and M. Sandborg, "Microbeam radiation therapy," Med. Phys. **19**, 1395-1400 (1992).

37. F. A. Dilmanian, Y. Qu, S. Liu, C. D. Cool, J. Gilbert, J. F. Hainfeld, C. A. Kruse, J. Laterra, D. Lenihan, M. M. Nawrocky, G. Pappas, C. I. Sze, T. Yuasa, N. Zhong, Z. Zhong, and J. W. McDonald, "X-ray microbeams: tumor therapy and central nervous system research," Nucl. Instrum. Meth. A **548**, 30-37 (2005).

38. J. A. Laissue, H. Blattmann, H. P. Wagner, M. A. Grotzer, and D. N. Slatkin, "Prospects for microbeam radiation therapy of brain tumours in children to reduce neurological sequelae," Dev. Med. Child Neurol. **49**, 577-581 (2007).

39. P. Regnard, G. Le Duc, E. Brauer-Krisch, I. Tropres, E. A. Siegbahn, A. Kusak, C. Clair, H. Bernard, D. Dallery, J. A. Laissue, and A. Bravin, "Irradiation of intracerebral 9L gliosarcoma by a single array of microplanar X-ray beams from a synchrotron: balance between curing and sparing," Phys. Med. Biol. **53**, 861-878 (2008).

40. J. C. Crosbie, R. L. Anderson, K. Rothkamm, C. M. Restall, L. Cann, S. Ruwanpura, S. Meachem, N. Yagi, I. Svalbe, R. A. Lewis, B. R. G. Williams, and P. A. W. Rogers, "Tumor cell response to synchrotron microbeam radiation therapy differs markedly from cells in normal tissues," Int. J. Radiat. Oncol. **77**, 886-894 (2010).

41. A. Bouchet, A. Boumendjel, E. Khalil, R. Serduc, E. Brauer, E. A. Siegbahn, J. A. Laissue, and J. Boutonnat, "Chalcone JAI-51 improves efficacy of synchrotron microbeam radiation therapy of brain tumors," J. Synchrotron Rad. **19**, 478-482 (2012).

42. E. Brauer-Krisch, A. Rosenfeld, M. Lerch, M. Petasecca, M. Akselrod, J. Sykora, J. Bartz, M. Ptaszkiewicz, P. Olko, A. Berg, M. Wieland, S. Doran, T. Brochard, A. Kamlowski, G. Cellere, A. Paccagnella, E. A. Siegbahn, Y. Prezado, I. Martinez-Rovira, A. Bravin, L. Dusseau, and P. Berkvens, "Potential high resolution dosimeters for MRT," 6th international conference on medical applications of synchrotron radiation **1266**, 89-97 (2010).

43. N. Nariyama, T. Ohigashi, K. Umetani, K. Shinohara, H. Tanaka, A. Maruhashi, G. Kashino, A. Kurihara, T. Kondob, M. Fukumoto, and K. Ono, "Spectromicroscopic film dosimetry for high-energy microbeam from synchrotron radiation," Appl. Radiat. Isotopes **67**, 155-159 (2009).

44. A. T. A. Rahman, D. A. Bradley, S. J. Doran, B. Thierry, E. Brauer-Krisch, and A. Bravin, "The thermoluminescence response of Ge-doped silica fibres for synchrotron microbeam radiation therapy dosimetry," Nucl. Instrum. Meth. A **619**, 167-170 (2010).

45. K. Rothkamm, J. C. Crosbie, F. Daley, S. Bourne, P. R. Barber, B. Vojnovic, L. Cann, and P. A. W. Rogers, "In situ biological dose mapping estimates the radiation burden delivered to 'spared' tissue between synchrotron X-Ray microbeam radiotherapy tracks," PLoS One **7**, e29853 (2012).

46. J. A. Bartz, G. J. Sykora, E. Brauer-Krisch, and M. S. Akselrod, "Imaging and dosimetry of synchrotron microbeam with aluminum oxide fluorescent detectors," Radiat. Meas. **46**, 1936-1939 (2011).

47. T. Ackerly, J. C. Crosbie, A. Fouras, G. J. Sheard, S. Higgins, and R. A. Lewis, "High resolution optical calorimetry for synchrotron microbeam radiation therapy," J. Instrum. **6**, P03003 (2011).

48. D. Maki, T. Ishii, F. Sato, Y. Kato, T. Yamamoto, and T. Iida, "Development of confocal laser microscope system for examination of microscopic characteristics of radiophotoluminescence glass dosemeters," Radiat. Prot. Dosim. **144**, 222-225 (2011).

49. M. Petasecca, A. Cullen, I. Fuduli, A. Espinoza, C. Porumb, C. Stanton, A. H. Aldosari, E. Brauer-Krisch, H. Requardt, A. Bravin, V. Perevertaylo, A. B. Rosenfeld, and M. L. F. Lerch, "X-Tream: a novel dosimetry system for synchrotron microbeam radiation therapy," J. Instrum. **7**, P07022 (2012).

50. G. Belev, G. Okada, D. Tonchev, C. Koughia, C. Varoy, A. Edgar, T. Wysokinski, D. Chapman, and S. Kasap "Valency conversion of samarium ions under high dose synchrotron generated X-ray radiation," phys. status solidi C **8**, 2822–2825 (2011).

51. D. L. Griscom, E. J. Friebele, K. J. Long, and J. W. Fleming, "Fundamental defect centers in glass - electron-spin resonance and optical-absorption studies of irradiated phosphorus-doped silica glass and optical fibers," J. Appl. Phys. **54**, 3743-3762 (1983).

52. C. A. G. Kalnins, N. A. Spooner, H. Ebendorff-Heidepriem, and T. M. Monro, " Luminescent properties of fluoride phosphate glass for radiation dosimetry," Opt. Mater. Express **3** (7), 960-967 (2013).

53. Siemens "Simulation of X-ray Spectra," (Siemens AG, 2014). https://w9.siemens.com/cms/oemproducts/home/x-raytoolbox/spektrum/pages/default.aspx.

54. A. Edgar, C. R. Varoy, C. Koughia, G. Okada, G. Belev, and S. Kasap, "High-resolution X-ray imaging with samarium-doped fluoroaluminate and fluorophosphate glass," J. Non-Cryst. Solids **377**, 124-128 (2013).

55. J. S. Stroud, "Color centers in a cerium-containing silicate glass," J. Chem. Phys. **37**, 836 (1962).

56. T. V. Bocharova, "A model of the capture volume of free carriers in fluorophosphate glasses doped with terbium," Glass Phys. Chem. **31**, 119-127 (2005).

57. P. W. Levy, "The Kinetics of Gamma-Ray Induced Coloring of Glass," J. Am. Ceram. Soc. **43**, 389-395 (1960).

58. A. Abragam , and B. Bleaney, *Electron paramagnetic resonance of transition ions* (Oxford University, 1970), Chap. 5.

6 Conclusion and Suggestions for Future Work

6.1 Summary and Conclusions

Fluorophosphate (FP) and fluoroaluminate (FA) glasses doped with trivalent samarium were evaluated as sensors of X-ray radiation with respect to their potential application in MRT. The detection is based on the X-ray induced conversion of trivalent Sm^{3+} to the divalent form Sm^{2+}. The photoluminescence signatures of Sm^{3+} and Sm^{2+} ions are distinctly different and both situated in the red region of the spectrum. Thus, the response, R, of the sensor to the dose delivered can be calculated as the ratio of PL line intensity of these two ions:

$R(t) = \mathrm{PL}(Sm^{2+})/\mathrm{PL}(Sm^{3+})$.

X-ray irradiation of Sm-doped glasses also results in the formation of light absorbing defects in the glass structure which cause the photodarkening of the glass. Photodarkening is an undesirable effect and makes the calculation of the response complicated specially in the case of FP glasses, where induced absorbance in the visible region partially blocks Sm^{3+} and Sm^{2+} emissions.

We studied the nature of X-ray induced defects by using optical absorbance spectroscopy and electron spin resonance (ESR) spectroscopy. To interpret the data, induced absorbance spectra were simulated as sum of Gaussians using a so-called “band separation” analysis. These bands were associated with different kinds of defects including electron centers (ECs) and hole centers (HCs) based on comparison with literature. ESR spectra were also approximated as sum of Lorentzians and Gaussians which were ascribed to various electron and hole centers, as well. Defect centers revealed by ESR spectroscopy and induced absorbance spectroscopy are in a good agreement.

Dose-response curves obtained for FP and FA glasses show that both of these glass plates provide a wide dynamic range which can cover a broad range of doses applied in MRT. These glasses show a linear response from 1Gy to ~150 Gy and nonlinear response up to ~2400 Gy where saturation is reached. The efficiency of $Sm^{3+} \rightarrow Sm^{2+}$ conversion in FA glasses is almost similar to that in FP glasses. However, the induced absorbance being in the UV make fluoroaluminate glasses more appealing as the response can be calculated more accurately and straightforwardly. These glass plates also allow the recording of microbeams dose profile with a spatial resolution as high as a few microns in 2D, very promising for PVDR screening in MRT. These properties suggest that Sm-doped FP and FA glass sensors can be promising tools for quality assurance (QA) of MRT.

To find the optimum doping concentration for detector plates, FP and FA glass samples with different Sm doping concentration were investigated. (Some of the Sm-doped samples were codoped with Eu^{2+}). It is revealed that codoping with Eu^{2+} does not provide any additional benefits and even higher amounts of codoping leads to a reduction in the response. The results also indicate that the response is almost independent from Sm doping concentration in the range of 0.001 to 0.2 at.%. While, the response $R(t)$ correlates with the amplitudes of X-ray induced absorbance bands (which are proportional to the concentration of related defect centers) specifically, both of them saturate at the same dose. At concentrations higher than ~0.2 at.%, the response monotonically decreases with the Sm doping concentration. This may be connected with the concentration quenching effect. On the other hand, results from ESR spectroscopy show an exponential decrease in the concentration of defect centers with increasing the Sm doping concentration for a constant dose received. While, electron centers show a faster decay in comparison with hole centers.

We were able to interpret the above experimental results by a model that is based on competition between various defects and Sm-ions for the electrons and holes generated by the absorption of X-rays. The model suggests that the valency reduction of Sm^{3+} ions occurs together with the formation of hole centers within their vicinity. In other words, Sm^{3+} to Sm^{2+}conversion which is an electron capturing process, requires a hole capturing process nearby to "hold" the holes. This explains the correlation between the response curve and induced absorbance intensity curve. It is also assumed that inside a volume called "capture volume" of Sm^{3+}, these ions prevent electron centers from capturing electrons. All electrons within this volume would be preferably captured by Sm^{3+} ions reducing them to Sm^{2+} ions. At the same time, holes would be captured by nearby hole centers. The model also considers that some of Sm^{2+} ions may convert back to Sm^{3+} ions (this is a "secondary" and less dominant reaction) by "stealing" the holes from hole centers within capture volume of Sm^{2+}. This can explain the suppression of defect centers by increasing the Sm-dopant concentration and faster decay of electron centers.

Good reproducibility of the response; as well as erasability and reusability of the detector plates is also demonstrated. It is shown that the effects of previous X-ray exposure including Sm^{3+} to Sm^{2+} valence conversion and X-ray induced optical absorbance may be erased by intense optical illumination or by annealing at a suitable temperature. Sequential X-ray irradiations show good reproducibility of the results.

It is shown that X-ray irradiated Sm-doped FP glasses can be optically erased by illumination under 405 nm light so that they can be reused in measuring the dose in microbeam radiation therapy. The use of intense optical illumination seemingly achieves near-complete Sm^{2+} to Sm^{3+} reconversion. On the other hand, the examination of optical transmission spectra shows

that optical illumination only partially erases existing X-ray induced bands, and, at the same time, induces new absorbance bands. However, this partial erasure does not affect the reproducibility of the response and good reproducibility of response was shown after optical erasure.

Another method for erasure is annealing. By monitoring both response and induced absorbance at different temperatures it is concluded that at a temperature sufficiently above glass transition temperature (T_g) of the doped glass, almost all Sm^{2+} ions become reconverted back to Sm^{3+} and almost all defects become annealed out. There is also no marked ESR signal. This method can return the irradiated sample back to its original unirradiated state. It was shown that the erased sample can reproduce the same response as the original sample. This is a distinct advantage in MRT since once calibrated, the same Sm-doped FP glass can be reused many times.

On the other hand, the annealing at temperatures just below T_g (temperatures between 350 °C and T_g) causes the effect of "thermally stimulated enhancement" of the photoluminescence associated with divalent samarium. This occurs together with a spectral shift in $^5D_0 \rightarrow {}^7F_j$ (j = 0, 1, 2) emission bands of Sm^{2+}. The observed effects are explained assuming the existence of metastable Sm^{2+} in an unrelaxed ionic environment which is the direct result of X-ray irradiation. The subsequent annealing leads to the relaxation and the appearance of stable Sm^{2+}. It might be possible to take advantage of "thermally stimulated enhancement" effect in cases where the response is weak and the amplification of the response is required. A broad ESR signal ascribed to Sm^{2+} ions is observed in this range. While, the intensities of ESR signals related to defects and induced absorbance reduce monotonically at the same temperature range. Annealing the irradiated glass at lower temperatures (up to 300 °C) will result in the reduction of hole center

related ESR signals, while the signals related to electron centers almost survive. Induced absorbance bands related to electron and hole centers exhibit almost the same behavior.

6.2 Suggestions for Future Work

This thesis has provided a fundamental knowledge about fluorophosphate (FP) and fluoroaluminate (FA) glasses and their properties for possible application in MRT dosimetry. However, for the detector to be practically used, further investigations are required including the following:

- The dose rate dependence has to be examined more thoroughly.
- Energy dependence should be investigated in a wider energy range (50-250 keV).
- Uncertainty in measuring the dose should be determined more accurately.
- The stability of the response should also be studied more exclusively.

Appendix: X-Ray Irradiation and Dose Calculation

A.1 Faxitron X-Ray Cabinet

For most experiments of this thesis, X-ray irradiation was performed using a Faxitron cabinet X-ray system, model 43855D with tungsten anode operating at (10-110 kVp) with maximum 3 mA tube current. The system has a manual timer with crystal controlled clock that can be set for exposures up to 60 minutes (1 second increments). The system has a Beryllium window (0.76 mm) and no additional filters were used for any exposures. To maximize the exposure, the samples were positioned as close as possible to the window (5cm from the anode) using an aluminum rod and maximum tube voltage (110 kVp) was used.

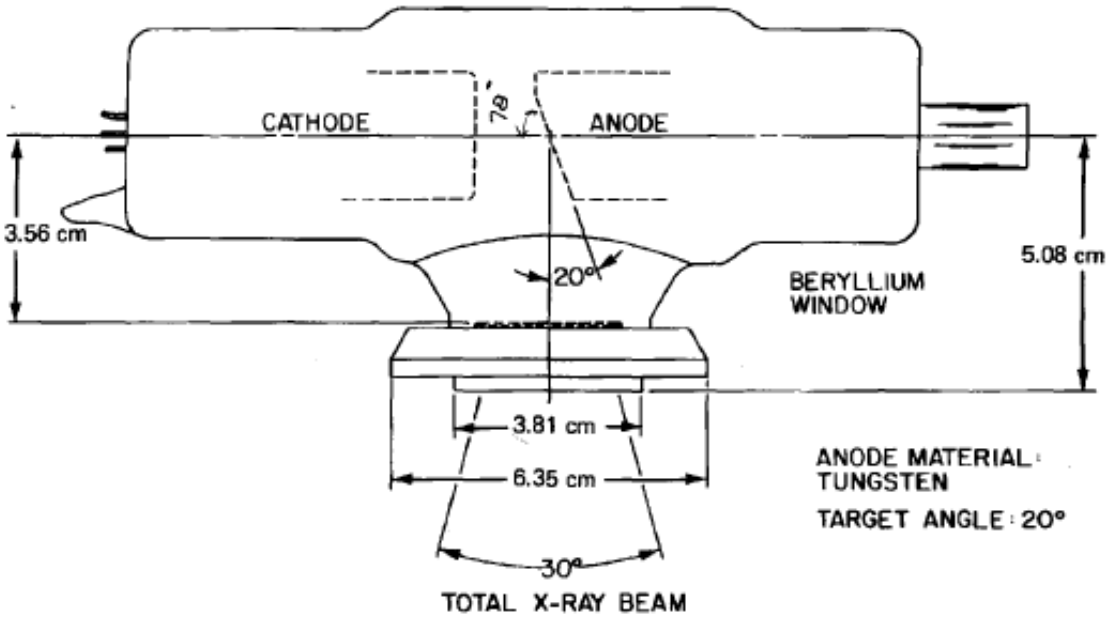

Figure A.1 Outline drawing of Faxitron standard X-ray tube.

Air kerma was calculated as 50 Gy / min at 5cm from the anode using an ion chamber. This value represents dose in air on the surface of the sample, and not inside the sample. The spectra from tube (shown in Figure A.1) were calculated using [1] which gives the mean energy of 45.18 keV.

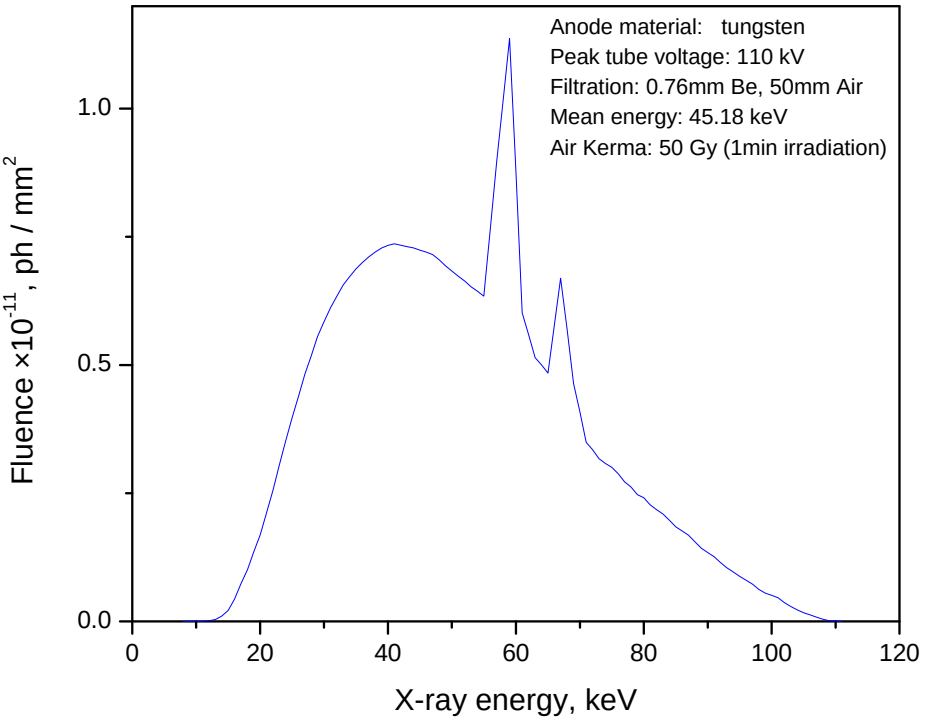

Figure A.2 X-ray spectra from Faxitron cabinet X-ray system operating at 110 kVp calculated for 1 min irradiation at 5cm from the anode (Air kerma = 50 Gy).

The total energy absorbed ($E_{absorved}$) by the samples can be calculated based on the method described in Ref. [2] using the following equation:

$$E_{absorved} = \int_0^{E_{max}} \Phi(E) E \frac{\mu_{en}}{\mu} \left[1 - \exp(-\mu(E)L)\right] dE \qquad (A.1)$$

where $\Phi(E)$ is the photon fluence shown in Figure A.2. We assume that $\left[1 - \exp(-\mu(E)L)\right] \approx 1$ as the samples have a thickness L greater than the attenuation depth. μ_{en}/μ is the ratio of mass energy absorption coefficient (μ_{en}/ρ) and mass attenuation coefficient (μ/ρ) of the compound. These coefficients can be obtained from NIST website (http://physics.nist.gov) for each element and their value for the compound can be calculated using:

$$\frac{\mu}{\rho}_{Composite} = \sum_{i=1}^{n} \frac{\mu}{\rho}_i w_i \qquad \text{(A.2)}$$

where w_i is the weight fraction ($w_i = \frac{M_i}{M_{total}}$). Figure A.3 shows the calculated μ/ρ and μ_{en}/ρ and their ratio μ_{en}/μ for FP glass samples.

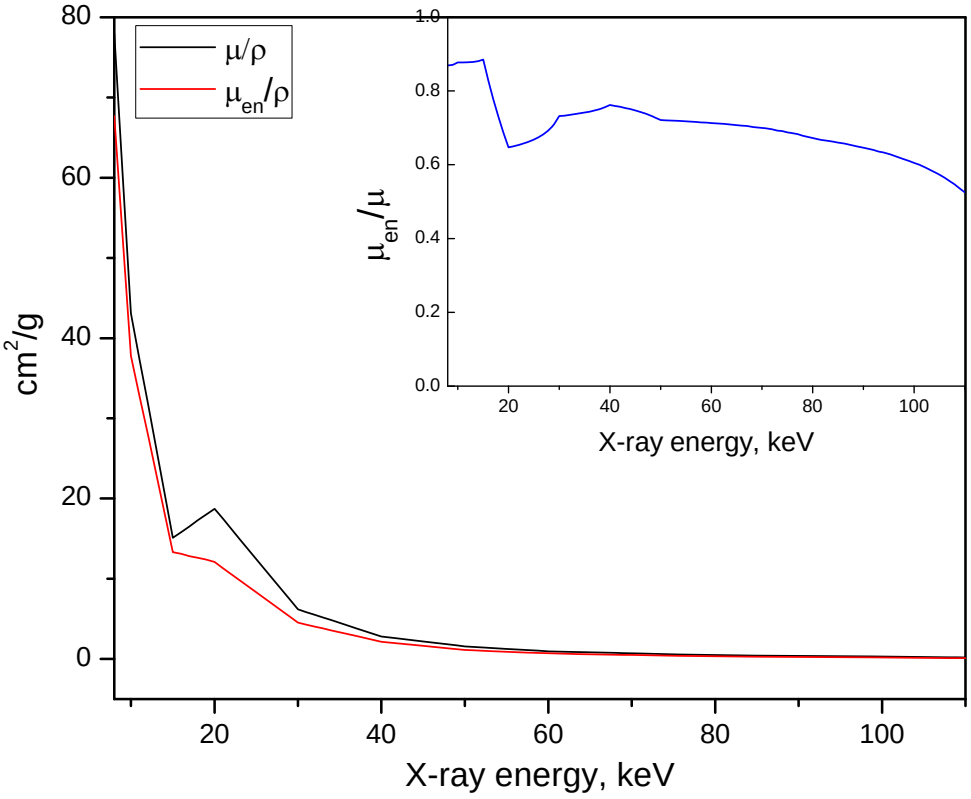

Figure A.3 calculated μ/ρ and μ_{en}/ρ and their ratio μ_{en}/μ for FP glass samples.

We can calculate the total dose absorbed by the glass samples (D) using:

$$D = E_{absorved}/M \qquad \text{(A.3)}$$

where M is the total mass of the glass samples. Knowing the glass density (3.42 g/cm^3), D is estimated from (A.1) and (A.3) equal to 6500Gy per cm^3 per minute.

A.2 Canadian Light Source

Biomedical Imaging and Therapy Bend Magnet (BMIT-BM) beamline 05B1-1 [3] at Canadian Light Source (CLS) was used for generating microbeams to test the spatial resolution of glass plates and also for irradiating some of the samples. The Canadian Light Source is a synchrotron facility with a third-generation 2.9 GeV storage ring located in Saskatoon, Saskatchewan, Canada. The irradiation was done 25.5 m away from the source. The maximum ring current was 250 mA for our experiments. The X-ray beam was filtered with three Cu filters of thickness 0.110, 0.276, and 0.552 mm providing an effective thickness of 0.938 mm. As a result, the spectrum (shown in Figure A.4) which has a peak X-ray energy of 50 keV would be in the similar range as X-rays used for MRT.

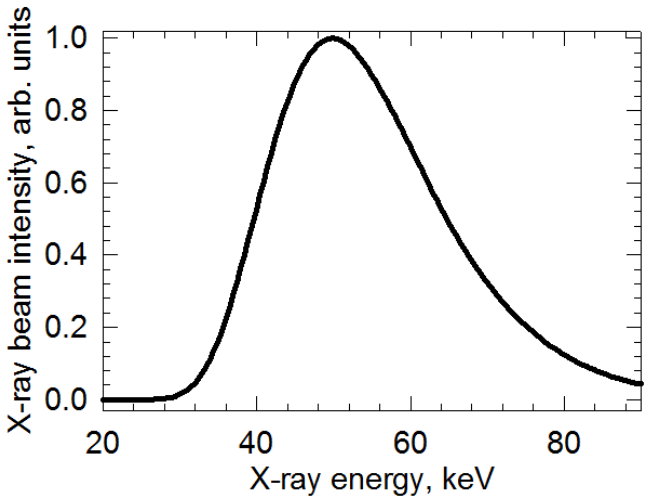

Figure A.4 The normalized spectrum of the X-rays from the BMIT-BM beamline.

At the point of irradiation the dose rate was estimated to be around 2 Gy/s (±20%) for an air absorber. Dose measurement was conducted by the beamline scientists using a Keithley 96030 ionization chamber connected to a Keithley 35050 dosimeter through a 100 μm slit.

A.3 References

1. Siemens, "Simulation of X-ray Spectra," (2014), https://w9.siemens.com/cms/oemproducts/home/x-raytoolbox/spektrum/pages/default.aspx.

2. J. M. Boone, ed. *Handbook of Medical Imaging Vol I* (SPIE, Belingha, WA, 2000).

3. T. W. Wysokinski, D. Chapman, G. Adams, M. Renier, P. Suortti, and W. Thomlinson, "Beamlines of the biomedical imaging and therapy facility at the Canadian light source—Part 1," Nuclear Instruments and Methods in Physics Research Section A: Accelerators, Spectrometers, Detectors and Associated Equipment **582**, 73-76 (2007).